

DOCUMENT CONTROL SHEET

	ORIGINATOR'S REF. NLR-TP-2003-342	SECURITY CLASS. Unclassified						
ORIGINATOR National Aerospace Laboratory NLR, Amsterdam, The Netherlands								
TITLE Space-time discontinuous Galerkin finite element method with dynamic grid motion for inviscid compressible flow - A VKI course								
PRESENTED AT The 33rd Computational Fluid Dynamics Course "Novel methods for solving convection dominated systems", as lecture notes of an invited lecture series, Von Karman Institute, Brussels, 24-28 March, 2003.								
AUTHORS J.J.W. van der Vegt and H. van der Ven	DATE July 2003	<table style="width: 100%; border-collapse: collapse;"> <tr> <td style="width: 50%; text-align: center;">PP</td> <td style="width: 50%; text-align: center;">REF</td> </tr> <tr> <td style="text-align: center;">108</td> <td style="text-align: center;">50</td> </tr> </table>	PP	REF	108	50		
PP	REF							
108	50							
DESCRIPTORS <table style="width: 100%; border-collapse: collapse;"> <tr> <td style="width: 50%;">Aerospace applications</td> <td style="width: 50%;">Grid motion</td> </tr> <tr> <td>Discontinuous Galerkin</td> <td>Hyperbolic equations</td> </tr> <tr> <td>Finite elements</td> <td>Space-time</td> </tr> </table>			Aerospace applications	Grid motion	Discontinuous Galerkin	Hyperbolic equations	Finite elements	Space-time
Aerospace applications	Grid motion							
Discontinuous Galerkin	Hyperbolic equations							
Finite elements	Space-time							
ABSTRACT <p>In these notes a new space-time discontinuous Galerkin finite element method for the solution of the Euler equations of gas dynamics in time-dependent flow domains is discussed. The discontinuous Galerkin discretization results in an efficient element-wise conservative upwind finite element method, which is particularly well suited for local mesh refinement. The upwind scheme uses a formulation of the HLLC flux applicable to moving meshes and several formulations for the stabilization operator to ensure monotone solutions around discontinuities are investigated. The non-linear equations of the space-time discretization are solved using a multigrid accelerated pseudo-time integration technique with an optimized Runge-Kutta method. In order to improve the computational efficiency a new and efficient quadrature rule for the flux integrals arising in the space-time discontinuous Galerkin discretization is presented and analyzed. The quadrature rule is a factor three more efficient than the commonly applied Gauss quadrature rule and does not affect the local truncation error and stability of the numerical scheme. The local truncation error of the resulting numerical discretization is determined and is shown to be the same as when product Gauss quadrature rules are used. Details of the approximation of the dissipation in the numerical flux are presented, which render the scheme consistent and stable. The numerical scheme is demonstrated with calculations of several model problems, an oscillating NACA 0012 airfoil and the three-dimensional, transonic flow over a deforming wing.</p>								



NLR-TP-2003-342

Space-time discontinuous Galerkin finite element method with dynamic grid motion for inviscid compressible flow

A VKI course

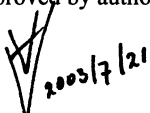
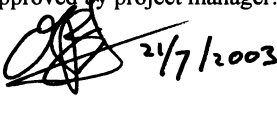
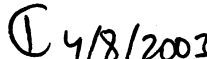
J.J.W. van der Vegt* and H. van der Ven

* *University of Twente*

Lecture notes of an invited lecture series held on the 33rd Computational Fluid Dynamics Course “Novel methods for solving convection dominated systems”, at the Von Karman Institute, Brussels, 24-28 March, 2003.

The contents of this report may be cited on condition that full credit is given to NLR and the authors.

Customer: National Aerospace Laboratory NLR
Working Plan number: A.1.B.7
Owner: National Aerospace Laboratory NLR
Division: Fluid Dynamics
Distribution: Unlimited
Classification title: Unclassified
July 2003

Approved by author: 	Approved by project manager: 	Approved by project managing department: 
--	--	---

Summary

In these notes a new space-time discontinuous Galerkin finite element method for the solution of the Euler equations of gas dynamics in time-dependent flow domains is discussed. The discontinuous Galerkin discretization results in an efficient element-wise conservative upwind finite element method, which is particularly well suited for local mesh refinement. The upwind scheme uses a formulation of the HLLC flux applicable to moving meshes and several formulations for the stabilization operator to ensure monotone solutions around discontinuities are investigated. The non-linear equations of the space-time discretization are solved using a multigrid accelerated pseudo-time integration technique with an optimized Runge-Kutta method. In order to improve the computational efficiency a new and efficient quadrature rule for the flux integrals arising in the space-time discontinuous Galerkin discretization is presented and analyzed. The quadrature rule is a factor three more efficient than the commonly applied Gauss quadrature rule and does not affect the local truncation error and stability of the numerical scheme. The local truncation error of the resulting numerical discretization is determined and is shown to be the same as when product Gauss quadrature rules are used. Details of the approximation of the dissipation in the numerical flux are presented, which render the scheme consistent and stable. The numerical scheme is demonstrated with calculations of several model problems, an oscillating NACA 0012 airfoil and the three-dimensional, transonic flow over a deforming wing.

Contents

List of figures	6
1 Introduction	9
2 Space-Time DGFEM	14
2.1 Space-time formulation of the Euler Equations of gas dynamics	14
2.2 Space-Time Discontinuous Galerkin Discretization of the Euler Equations	15
2.2.1 Geometry definition of space-time elements	15
2.2.2 Space-time discontinuous Galerkin finite element approximation	17
2.2.2.1 Weak formulation of the Euler equations	17
2.2.2.2 Transformation of the space-time weak formulation into ALE form	18
2.2.2.3 Introduction of numerical flux	20
2.2.3 Equations for the flow field expansion coefficients	22
2.2.4 Flux Calculation	25
2.2.4.1 Extension of the HLLC scheme to moving meshes	25
2.2.4.2 Evaluation of flux integrals	28
2.2.5 Stabilization operator	29
2.3 Solution of the non-linear DG coefficient equations	32
2.3.1 Multigrid algorithm for pseudo-time integration	32
2.3.2 Stability analysis of pseudo-time integration	39
2.4 Mesh adaptation	42
2.4.1 Space-time slab coupling for element refinement	44
2.4.2 Space-time slab coupling for element coarsening	45
2.5 Grid deformation	45
3 Efficient Flux Quadrature	47
3.1 Preliminaries	47
3.2 Taylor quadrature rule	48
3.3 Taylor approximation	50
3.3.1 Contact wave analogy	53
3.3.2 Consistency of the approximation	54
3.3.3 Boundary conditions	55
3.3.4 Local truncation error	56
3.3.5 Validity of the approximation	56
3.3.6 Analysis of element face quadrature errors	57

3.3.7	Analysis of element volume quadrature error	60
3.3.8	Truncation error of space-time discontinuous Galerkin discretization	62
4	Applications	67
4.1	Sod's shock tube problem	67
4.2	Accuracy study of the discontinuous Galerkin discretization	67
4.3	Comparison of Taylor and Gauss quadrature	69
4.3.1	Aerodynamic forces	69
4.3.2	Slip flow boundary	71
4.3.3	Computational efficiency	77
4.3.4	Computational complexity of DG methods	77
4.4	Steady transonic flow	83
4.5	Oscillating NACA 0012 airfoil in transonic flow	83
4.6	First torsion mode of the AGARD 445.6 wing	85
5	Concluding Remarks	94
6	Acknowledgments	95
7	References	96
	3 Tables	
	26 Figures	
	Appendices	101
A	Sobolev spaces	101
B	Some facts from differential geometry	103
C	Geometric integrals	105
	(2 Tables)	
D	Discrete conservation	107

(108 pages in total)

List of figures

Figure 1	Illustration of the geometry of two-dimensional space-time elements in both computational and physical space. Notations in the text.	19
Figure 2	Wave pattern used in the definition of the HLLC flux function for an element face moving with velocity v . Here S_L and S_R are the fastest left and right moving signal velocities. The solution in the star region U^* is divided by a wave with velocity S_M .	26
Figure 3	Coarsening based on refinement tree. The numbers at the nodes of the tree refer to the number of leaves in the subtree. The dashed lines show where the tree is pruned. The fine grid cells and the resulting coarse grid cells are shown to the right.	35
Figure 4	Multigrid levels in an adapted mesh about the NACA 0012 airfoil.	36
Figure 5	Convergence rate comparison of the residual for the element mean and fluctuating DG coefficient equations using single and multigrid computations (dark lines) on a twice adapted mesh of a NACA 0012 airfoil.	38
Figure 6	Locus of the eigenvalues $z_m(\theta)$, $\theta \in [0, 2\pi)$, (dots) of the DG discretization of $u_t + au_x = 0$ and the stability domain of the 5-stage semi-implicit Runge-Kutta method with optimized coefficients. $CFL_{\Delta t} = 1.0$, $CFL_{\Delta \tau} = 1.8$ (top), $CFL_{\Delta t} = 100.0$, $CFL_{\Delta \tau} = 1.8$ (bottom), no grid velocity.	41
Figure 7	Locus of the eigenvalues $z_m(\theta)$, $\theta \in [0, 2\pi)$, (dots) of the DG discretization of $u_t + au_x = 0$ and the stability domain of the explicit 5-stage Runge-Kutta method (42) with optimized coefficients (top) and the five stage semi-implicit Jameson Runge-Kutta scheme (bottom). $CFL_{\Delta t} = 1.0$. $CFL_{\Delta \tau} = 1.8$, no grid velocity.	43
Figure 8	Space-time mesh for the adaptive solution of Sod's shock tube problem.	68
Figure 9	Results of Sod's shock tube problem at $t = 0.2531$ on a uniform (top) and adapted mesh (bottom). Computed results plotted as circles, exact solution plotted as lines.	70
Figure 10	Original and one time adapted mesh for converging-diverging channel.	71
Figure 11	L^2 -Error in flow calculations for converging-diverging channel on uniform and adapted meshes.	72
Figure 12	Comparison of pressure distribution for the transonic over a NACA0012 foil.	73

Figure 13	Comparison of the total pressure loss at the wall for the flow around a circular cylinder ($M_\infty = 0.38$) using Gauss and Taylor flux quadrature rules for isoparametric elements on a coarse (32×48 elements) and fine mesh (64×96 elements) and superparametric elements on a coarse mesh (32×48 elements).	75
Figure 14	Comparison of the Mach number field of a circular cylinder at $M_\infty = 0.38$ using Gauss (upper left) and Taylor quadrature with (locally refined) linear isoparametric elements (coarse mesh with 1536 cells (upper right), fine mesh with 6144 cells (lower left), and three times adapted coarse mesh with 8358 elements (lower right)).	76
Figure 15	Pressure coefficient C_p at 65% and 90% span for the ONERA M6 wing. Experimental results are shown with dots.	79
Figure 16	Pressure distribution on wing and symmetry plane for the ONERA M6 wing.	80
Figure 17	Pressure coefficient C_p at 65% (top) and 90% span (bottom) for the ONERA M6 wing. (\cdots original grid, $- - -$ one adaptation, $- - -$ two adaptations, $- - -$ three adaptations, $\diamond \diamond \diamond$ experiment).	81
Figure 18	Adapted mesh on ONERA M6 wing.	82
Figure 19	Lift and drag coefficient on oscillating NACA 0012 airfoil ($M_\infty = 0.8$, $\omega = \pi/10$).	84
Figure 20	Adapted mesh around oscillating NACA 0012 airfoil, contours of density, and pressure coefficient C_p on the airfoil surface for $\alpha = 0.5^\circ$ (pitching downward) and $\alpha = -0.5^\circ$ ($M_\infty = 0.8$, $\omega = \pi/10$).	87
Figure 21	Adapted mesh around oscillating NACA 0012 airfoil, contours of density, and pressure coefficient C_p on the airfoil surface for $\alpha = 0.23^\circ$ (pitching upward) and $\alpha = 2.0^\circ$ (pitching upward) ($M_\infty = 0.8$, $\omega = \pi/10$).	88
Figure 22	Adapted mesh around oscillating NACA0012 airfoil, contours of density, and pressure coefficient C_p on the airfoil surface for $\alpha = 3.77^\circ$ (pitching upward) and $\alpha = 4.0^\circ$ (pitching downward) ($M_\infty = 0.8$, $\omega = \pi/10$).	89
Figure 23	Wing deformation at the two extreme positions. The vertical coordinate is multiplied with a factor 5, to make the deformation visible. The flow comes from the right.	90
Figure 24	Convergence history for five time steps of the simulation of the first torsion mode of the AGARD 445.6 wing	91
Figure 25	Mach number contours on wing and symmetry plane at time $t = \frac{7}{20}T$, where T is the period of the torsion mode.	92
Figure 26	C_p -distributions at a cross section at 88% span	93



This page is intentionally left blank.

1 Introduction

These notes discuss a new discontinuous Galerkin (DG) finite element method for the adaptive solution of the unsteady Euler equations of gas dynamics in three-dimensional time-dependent flow domains. The algorithm results in a second order accurate finite element discretization on deforming meshes and accuracy can be improved using local mesh refinement or h -type mesh adaptation. In the development of the numerical scheme the main objectives to be satisfied are obtaining a conservative discretization on deforming meshes, the accurate capturing of flow discontinuities using h -adaptation, while maintaining accuracy on locally refined meshes, and achieving good computational efficiency on parallel computers. These requirements have been the main motivation to develop a discontinuous Galerkin finite element method. The main feature of discontinuous Galerkin methods is the use of basis functions which are discontinuous across element faces. This results in a finite element discretization with a very compact stencil, which can be combined well with h -adaptation. These properties are important for many problems and the main reason why discontinuous Galerkin methods presently are receiving significant attention.

Discontinuous Galerkin methods can be subdivided into two main classes, namely discretizations with basis functions which are discontinuous either in space or in time. The first class of DG methods, in combination with a TVD Runge-Kutta time integration method, has been thoroughly investigated by Cockburn and Shu. Detailed surveys can be found in (Ref. 18, 19). The second class of DG methods uses discontinuous basis functions in time and a streamline upwind Galerkin or Galerkin least squares discretization in space. Both classes of discontinuous Galerkin methods are also extensively discussed in Barth (Ref. 3) and Schwab (Ref. 36).

The separation between space and time becomes cumbersome for time-dependent domain boundaries, which require the mesh to follow the boundary movement. We will therefore not separate space and time, but consider the Euler equations directly in four dimensional space, and use basis functions in the finite element discretization which are discontinuous across element faces, both in space and time. We refer to this technique as the space-time discontinuous Galerkin finite element method. The space-time DG method provides optimal efficiency to adapt and deform the mesh, while maintaining a conservative scheme which does not require interpolation of data after mesh refinement or deformation. The space-time DG method presented in this notes is an extension of our research on a solution adaptive discontinuous Galerkin finite element method for steady three-dimensional inviscid and compressible flows, Van der Vegt and Van der Ven (Ref. 43). In the first part of these notes we discuss the general formulation of the space-time DG method for the adaptive solution of the Euler equations in time-dependent flow domains. In the second part we discuss and analyze a new integration technique for the element face and volume integrals for



discontinuous Galerkin discretizations, which results in a significant improvement in computational efficiency. We will also demonstrate the maturity of the space-time DG discretization with three-dimensional aerodynamic applications, such as a deforming wing in transonic flow.

The combined use of space and time discontinuous basis functions in a discontinuous Galerkin method has been proposed by Jaffre, Johnson and Szepessy (Ref. 26), which theoretically analyzed this technique for multi-dimensional scalar conservation laws on non-deforming meshes. See also Cockburn and Gremaud (Ref. 14). Until now, however, the use of space-time discontinuous basis functions in DG methods has not been fully explored for non-linear hyperbolic systems of partial differential equations, such as the Euler equations of gas dynamics. An initial study was conducted by Lowrie, Roe and van Leer (Ref. 32). Their formulation results in a staggered space-time mesh, which is quite different from the DG discretization presented in these notes, and does not easily extend to local mesh refinement which is important for many applications.

In order to make the space-time DG method an accurate and efficient technique for the solution of the Euler equations of gas dynamics we had to deal with a number of issues. First, we will extensively discuss the weak formulation of the space-time discontinuous Galerkin finite element method using the Arbitrary Lagrangian Eulerian (ALE) approach. This technique decouples the grid motion from the motion of the fluid particles and is widely used in fluid-structure interaction problems and ideally suited for deforming meshes. The discontinuous Galerkin discretization which we present automatically satisfies the geometric conservation law, which states that a uniform flow field should not be influenced by the grid motion, since the element face and volume integrals are calculated with sufficiently accurate quadrature rules. This problem was analyzed in detail by Lesoinne and Farhat (Ref. 29), and is an essential condition to obtain at least first order accuracy in time, as was proven by Guillard and Farhat (Ref. 24).

The space-time discontinuous Galerkin discretization results for each element in a coupled system of non-linear equations. We will present and analyze a pseudo-time integration method with multigrid acceleration which can efficiently solve these equations. In this technique the non-linear equations of the DG discretization are augmented with a pseudo-time and marched to steady state in pseudo-time. The pseudo-time integration is significantly improved by optimizing the Runge-Kutta time integration method. The use of a multigrid technique for a DG discretization of hyperbolic partial differential equations is new and required a significant development effort. The proposed algorithm works well on locally refined meshes and maintains the local structure of a DG discretization, which allows a straightforward parallelization of the method.

Since the Euler equations of gas dynamics are hyperbolic and develop discontinuities in finite

time it is important to ensure monotone solutions around discontinuities. In the TVD Runge-Kutta discontinuous Galerkin method this is accomplished by using a slope limiter, for a survey see Cockburn (Ref. 18). In our earlier work we also used this limiter (Ref. 43, 44), but the limiter in a DG method prevents convergence to steady state and also has a negative effect on the numerical accuracy. In these notes we will discuss the use of a stabilization operator instead of a slope limiter to maintain monotone solutions. This technique significantly improved the accuracy and convergence to steady state of the pseudo-time integration.

Applications of computational fluid dynamics techniques to real-life (time-dependent, three-dimensional) applications, such as occur for instance in aerodynamics, require significant computational resources. This certainly applies to the DG method, which is known to be computationally expensive. The computational complexity of the DG method has been investigated by various authors, e.g. Lockard and Atkins (Ref. 31) and Van der Ven and Van der Vegt (Ref. 48). The computationally most intensive part of the method is the evaluation of the flux integrals. The standard approach for the evaluation of these integrals is the application of Gauss quadrature rules. For second-order accurate space-time DG methods a mixture of two-point and three-point product rules is required, which implies twelve flux evaluations for the face fluxes and 27 flux evaluations for the volume fluxes. This number is prohibitively large and would render DG methods impractical for real-life applications.

Atkins and Shu (Ref. 2) presented a quadrature free implementation of the DG method, and in earlier work, Van der Vegt and Van der Ven (Ref. 43) presented a DG implementation which requires only one flux evaluation per face. In this latter work (Ref. 43) a slope limiter was applied for stability which is replaced in these notes with a stabilization operator. This improves both the convergence to steady state and the accuracy of the method. The quadrature rule presented in (Ref. 43), however, proved to be unstable in combination with the stabilization operator.

This prompted the development of the so-called Taylor quadrature rule, which is discussed in the second part of these notes. The Taylor quadrature rule is related to the quadrature-free approach of Atkins and Shu (Ref. 2). As in the quadrature-free approach the flux is expanded in the basis functions, but the coefficients are obtained from a direct Taylor expansion of the flux in the face center. Since the expansion coefficients of the solution vector related to the linear basis functions can be interpreted as first derivatives of the solution vector, these expansion coefficients occur directly in the Taylor expansion of the flux. This demonstrates that DG methods provide a natural setting for the Taylor quadrature rule.

For linear fluxes, this flux expansion is equal to the flux expansion in the quadrature-free approach,



but for the nonlinear Euler flux the expansion is different since we only use as many terms as the number of basis functions in the DG expansion, whereas in the quadrature-free approach the expansion would also include the second order terms in the Taylor expansion. The Taylor quadrature rule significantly reduces the number of flux evaluations, reducing the flop count with respect to the required product Gauss quadrature rule. Moreover, since only data in the face center is required, the data locality of the algorithm is improved, which enhances the computational speed on cache-based computers.

The quadrature rule in the DG method must be chosen carefully, since it can negatively affect the accuracy of the DG discretization. For the TVD Runge-Kutta space DG discretization of a multi-dimensional scalar conservation law this has been analyzed by Cockburn, Hou, and Shu (Ref. 16) when Gauss quadrature rules are used for the flux integrals. In these notes we analyze the accuracy of the space-time DG discretization both for the Taylor and Gauss quadrature rules. The analysis shows that the Taylor quadrature rule does not have an adverse effect on the accuracy of the DG method, which is also confirmed by the numerical experiments discussed in Chapter 4.

Having established the accuracy of the numerical method, the next issue is the stability of the discretization. Unlike the approach of Atkins and Shu (Ref. 2), the Taylor quadrature rule does not presuppose a relatively simple numerical flux, such as the Lax-Friedrichs flux, which for our applications is too dissipative. We use the HLLC flux (Toro (Ref. 41)) which has an accuracy comparable to the Osher numerical flux, at considerably less computational cost. In our experience the proper integration of the upwind dissipation of the numerical flux is also essential for the stability of the gradient equations. This implies that the dissipative part of the numerical flux must be linearized as well. The linearization of the HLLC flux in the Taylor quadrature rule is discussed in detail, and is constructed such that it results in a stable scheme, with correct treatment of the pressure term at contact discontinuities, and satisfies the Geometric Conservation Law for moving meshes.

The outline of these notes is as follows. In Chapter 2 we discuss the main aspects of the space-time discontinuous Galerkin finite element method (STDGFEM). After some preliminaries we discuss in Section 2.2 the weak formulation of the space-time discontinuous Galerkin discretization and show its relation with the ALE weak formulation. Next, we give a derivation of the non-linear equations for the DG expansion coefficients and define the HLLC flux suitable for moving boundaries and the stabilization operator necessary to ensure monotone solutions around discontinuities. In Section 2.3 the multigrid accelerated pseudo-time integration method for the solution of the non-linear DG equations is presented and its stability is analyzed. The mesh adaptation is dis-



cussed in Section 2.4 and we give a brief summary of the mesh deformation algorithm in Section 2.5.

In Chapter 3 we present the Taylor quadrature rule for the face and volume flux integrals. First, we transform in Section 3.1 the flux integrals into a form suitable for the Taylor approximation. The Taylor quadrature rule is discussed in Section 3.2 and the application to the HLLC scheme in Section 3.3. In Section 3.3.4 the local truncation error of the DG scheme using the Taylor and Gauss quadrature rules is analyzed. Numerical experiments are presented in Chapter 4, including the simulation of the flow past an oscillating NACA 0012 airfoil using locally refined meshes and a deforming AGARD 445.6 wing. Conclusions are drawn in Chapter 5. The Appendices give background information for the error analysis and detailed expressions for the element face and volume integration.

2 Space-time discontinuous Galerkin formulation for the Euler equations of gas dynamics in time-dependent flow domains

2.1 Space-time formulation of the Euler Equations of gas dynamics

We consider the Euler equations of gas dynamics in a time-dependent flow domain. Since the flow domain boundary is moving and deforming in time we do not make an explicit separation between the space and time variables and consider the Euler equations directly in \mathbb{R}^4 . Let $\mathcal{E} \subset \mathbb{R}^4$ be an open domain. A point $x \in \mathbb{R}^4$ has coordinates (x_1, \dots, x_4) , but we will also frequently use the notation $(\bar{x}, t) \in \mathbb{R}^4$, with $\bar{x} = (x_1, x_2, x_3) \in \mathbb{R}^3$ the position vector at time t and $t = x_4$ representing time. The flow domain $\Omega(t)$ at time t is defined as: $\Omega(t) := \{\bar{x} \in \mathbb{R}^3 \mid (\bar{x}, t) \in \mathcal{E}\}$, with t_0 and T the initial and final time of the evolution of the flow domain. The space-time domain boundary $\partial\mathcal{E}$ consists of the hypersurfaces $\Omega(t_0) := \{x \in \partial\mathcal{E} \mid x_4 = t_0\}$, $\Omega(T) := \{x \in \partial\mathcal{E} \mid x_4 = T\}$ and $\mathcal{Q} := \{x \in \partial\mathcal{E} \mid t_0 < x_4 < T\}$.

Let $\mathcal{F} : \mathbb{R}^5 \rightarrow \mathbb{R}^{5 \times 4}$ denote the flux tensor, which is defined as:

$$\mathcal{F} = \begin{pmatrix} \rho u_1 & \rho u_2 & \rho u_3 & \rho \\ \rho u_1^2 + p & \rho u_1 u_2 & \rho u_1 u_3 & \rho u_1 \\ \rho u_1 u_2 & \rho u_2^2 + p & \rho u_2 u_3 & \rho u_2 \\ \rho u_1 u_3 & \rho u_2 u_3 & \rho u_3^2 + p & \rho u_3 \\ (\rho E + p)u_1 & (\rho E + p)u_2 & (\rho E + p)u_3 & \rho E \end{pmatrix},$$

with ρ , p , and E the density, pressure, and specific total energy, respectively, and u_i the velocity components in the Cartesian coordinate directions x_i , $i \in \{1, 2, 3\}$ of the velocity vector $u : \mathcal{E} \rightarrow \mathbb{R}^3$. Let the vector $U : \mathcal{E} \rightarrow \mathbb{R}^5$ denote the conservative flow variables with components:

$$U_i = \mathcal{F}_{i4},$$

then the Euler equations of gas dynamics are defined as:

$$\operatorname{div} \mathcal{F}(U(x)) = 0, \quad x \in \mathcal{E}, \quad (1)$$

together with the initial and boundary conditions:

$$\begin{aligned} U(x) &= U_0(x), & x &\in \Omega(t_0), \\ U(x) &= \mathcal{B}(U, U_w), & x &\in \mathcal{Q}. \end{aligned}$$

Here $U_0 : \Omega(t_0) \rightarrow \mathbb{R}^5$ denotes the initial flow field, $\mathcal{B} : \mathbb{R}^5 \times \mathbb{R}^5 \rightarrow \mathbb{R}^5$ the boundary operator and $U_w : \mathcal{Q} \rightarrow \mathbb{R}^5$ the prescribed boundary flow field data. The divergence of a second order tensor is defined as: $\operatorname{div} \mathcal{F} = \frac{\partial \mathcal{F}_{ij}}{\partial x_j}$, and the summation index is used on repeated indices in these notes. The Euler equations are completed with the equation of state for a calorically perfect gas: $p = (\gamma - 1)\rho(E - \frac{1}{2}u_i u_i)$, with γ the ratio of specific heats.

2.2 Space-Time Discontinuous Galerkin Discretization of the Euler Equations

2.2.1 Geometry definition of space-time elements

Consider a partitioning $t_0 < t_1 < \dots < T$ of the time interval (t_0, T) and define the time interval I_n as: $I_n = (t_n, t_{n+1})$. The space-time domain $\mathcal{E} \subset \mathbb{R}^4$ is split into a finite number of space-time slabs: $\{x \in \mathcal{E} \mid x_4 \in I_n\}$. The evolution of the flow domain during the time interval I_n is represented by the mapping Φ_t^n , which is defined as:

$$\Phi_t^n : \Omega(t_n) \rightarrow \Omega(t) : \bar{x} \mapsto \Phi_t^n(\bar{x}), \quad t \in I_n. \quad (2)$$

The mapping Φ_t^n is assumed to be sufficiently smooth, orientation preserving and invertible in each time interval I_n , but can be different in different time intervals. This makes it possible to generate a new grid when elements become too severely distorted during the dynamic mesh movement. At the time level t_n we use hexahedral elements K to define the tessellation \bar{T}_h^n :

$$\bar{T}_h^n := \{K_j^n \mid \bigcup_{j=1}^{N_n} \bar{K}_j^n = \bar{\Omega}_h(t_n) \text{ and } K_j^n \cap K_{j'}^n = \emptyset \text{ if } j \neq j', 1 \leq j, j' \leq N_n\},$$

such that $\Omega_h(t_n) \rightarrow \Omega(t_n)$ as $h \rightarrow 0$, with h the radius of the smallest sphere completely containing each element $K \in \bar{T}_h^n$, and N_n the total number of hexahedra in $\Omega_h(t_n)$. Each element $K^n \in \bar{T}_h^n$ is related to the master element $\hat{K} = (-1, 1)^3$ through the mapping F_K^n :

$$F_K^n : \hat{K} \rightarrow K^n : \bar{\xi} \mapsto \bar{x} = \sum_{i=1}^8 x_i(K^n) \chi_i(\bar{\xi}),$$

with $x_i(K^n) \in \mathbb{R}^3$, $1 \leq i \leq 8$, the spatial coordinates of the vertices of the hexahedron K^n at time t_n and $\chi_i(\bar{\xi})$ the standard tri-linear finite element shape functions for hexahedra, with $\bar{\xi} = (\xi_1, \xi_2, \xi_3) \in \hat{K}$. The elements K^{n+1} are now obtained by moving the vertices of each hexahedron $K^n \in \bar{T}_h^n$ with the mapping Φ_t^n to their new position at time $t = t_{n+1}$, and we can define the mapping:

$$F_K^{n+1} : \hat{K} \rightarrow K^{n+1} : \bar{\xi} \mapsto \bar{x} = \sum_{i=1}^8 \Phi_{t_{n+1}}^n(x_i(K^n)) \chi_i(\bar{\xi}).$$

The space-time elements are obtained by connecting the elements in $\Omega(t_n)$ and $\Omega(t_{n+1})$ by linear interpolation in time. This results in the following parameterization of the space-time elements \mathcal{K}^n :

$$G_K^n : \hat{\mathcal{K}} \rightarrow \mathcal{K}^n : \xi \mapsto (\bar{x}, t) = \left(\frac{1}{2}(1 - \xi_4) F_K^n(\bar{\xi}) + \frac{1}{2}(1 + \xi_4) F_K^{n+1}(\bar{\xi}), \right. \\ \left. \frac{1}{2}(t_n + t_{n+1}) + \frac{1}{2}(t_{n+1} - t_n) \xi_4 \right), \quad (3)$$

with $\xi \in \hat{\mathcal{K}}$ the computational coordinates in the master element $\hat{\mathcal{K}}$, which is defined as: $\hat{\mathcal{K}} = (-1, 1)^4$. The space-time tessellation is now defined as:

$$\mathcal{T}_h^n := \{\mathcal{K} = G_K^n(\hat{\mathcal{K}}) \mid K \in \bar{\mathcal{T}}_h^n\}.$$

We will also frequently use the notation $K(t)$ for the element K at time t , which is defined as: $K(t) = \{\bar{x} \in \mathbb{R}^3 \mid (\bar{x}, t) \in \mathcal{K}\}$. The space-time element \mathcal{K}^n is bounded by the hypersurfaces $K(t_n^+) = \lim_{\epsilon \downarrow 0} K(t_n + \epsilon)$, $K(t_{n+1}^-) = \lim_{\epsilon \downarrow 0} K(t_{n+1} - \epsilon)$, and $\mathcal{Q}^n = \partial\mathcal{K}^n \setminus (K(t_n^+) \cup K(t_{n+1}^-))$. This notation is used to indicate that the mesh can change discontinuously at the time levels t_n and t_{n+1} .

The boundary faces of \mathcal{K}^n can also be represented using the mapping (3). For $1 \leq m \leq 8$ define the eight faces \mathcal{S}_m of the space-time element \mathcal{K} , with $\partial\mathcal{K} = \cup_{m=1}^8 \mathcal{S}_m$, by:

$$\begin{aligned} \mathcal{S}_{2m-1} &= \{G_K(\xi) \mid \xi \in \hat{\mathcal{K}}, \xi_m = -1\}, \\ \mathcal{S}_{2m} &= \{G_K(\xi) \mid \xi \in \hat{\mathcal{K}}, \xi_m = 1\}, \quad 1 \leq m \leq 4. \end{aligned} \quad (4)$$

Note that $\mathcal{Q}^n = \cup_{m=1}^6 \mathcal{S}_m$, $K(t_n^+) = \mathcal{S}_7$, and $K(t_{n+1}^-) = \mathcal{S}_8$.

The reader is referred to Figure 1 for a two-dimensional illustration of the elements and mappings.

Remark 2.2.1 *The tessellation \mathcal{T}_h^n does not impose a limitation on the number of elements which can connect to a face of an element. This is important because during the simulations the computational mesh will be adapted by subdividing elements in space and/or time in regions where more mesh resolution is required.*

Remark 2.2.2 *Since we use a tri-linear representation of the elements in space, this implies that we use a bi-linear representation of the geometry at slip flow boundaries. Recently, Bassi and Rebay (Ref. 4), concluded that a higher order representation of a slip flow boundary is mandatory in order to avoid strong numerical boundary layers and to obtain convergence. In Section 4.3.2 we show that under grid refinement the numerical boundary layer diminishes for hexahedral type elements. Since local mesh refinement already is an integral part of our algorithm, we use this technique to remove the numerical boundary layer at slip flow boundaries and it is not necessary to use a higher-order accurate boundary representation.*

2.2.2 Space-time discontinuous Galerkin finite element approximation

2.2.2.1 Weak formulation of the Euler equations

In order to ensure that the different forms of the weak formulation of the Euler equations of gas dynamics, which are discussed in this section, are well defined we introduce the broken space $V(\mathcal{T}_h^n)$:

$$\begin{aligned} V(\mathcal{T}_h^n) := \{ & U : \mathcal{T}_h^n \rightarrow \mathbb{R}^5 \mid (\text{grad } U^1)^T : \mathcal{F}(U^2)|_{\mathcal{K}_j^n} \in L^1(\mathcal{K}_j^n); \\ & ((\text{grad } U^2)^T \cdot \mathfrak{D}(U^1)) : \text{grad } U^1|_{\mathcal{K}_j^n} \in L^1(\mathcal{K}_j^n); \\ & \gamma^-(U^1) \cdot (n_{\mathcal{K}}^T \mathcal{F}(\gamma^-(U^2)) + n_{\mathcal{K}}^T \mathcal{F}(\gamma^+(U^3))) \in L^1(\partial\mathcal{K}_j^n); \\ & \forall (U^1, U^2, U^3) \in V(\mathcal{T}_h^n), \forall \mathcal{K}_j^n \in \mathcal{T}_h^n \}, \end{aligned}$$

with L^1 the space of Lebesgue integrable functions, $\gamma^\pm(U) = \lim_{\epsilon \downarrow 0} U(x \pm \epsilon n_{\mathcal{K}})$ the traces of U at $\partial\mathcal{K}$, $n_{\mathcal{K}} \in \mathbb{R}^4$ the unit outward normal vector at $\partial\mathcal{K}$, $\mathfrak{D} : \mathbb{R}^5 \rightarrow \mathbb{R}^{4 \times 4}$ the artificial viscosity matrix, and superscript T denotes the transposition of a vector. We will also frequently use the notation U^\pm to denote $\gamma^\pm(U)$. The gradient operator $\text{grad} : \mathbb{R}^5 \rightarrow \mathbb{R}^{4 \times 5}$ is defined as: $(\text{grad } U)_{ij} = \frac{\partial U_j}{\partial x_i}$ and the symbol $:$ represents the dyadic product of two second order tensors and is defined for $\mathcal{A}, \mathcal{B} \in \mathbb{R}^{n \times m}$ as $\mathcal{A} : \mathcal{B} = \mathcal{A}_{ij} \mathcal{B}_{ij}$.

The discontinuous Galerkin finite element discretization is obtained by approximating the test and trial functions in each element $\mathcal{K} \in \mathcal{T}_h^n$ with polynomial expansions which are discontinuous across element faces, both in space and time. First, in the master element $\hat{\mathcal{K}}$ the basis functions $\hat{\phi}_m : \hat{\mathcal{K}} \rightarrow \mathbb{R}$ are defined which are linear in computational space:

$$\begin{aligned} \hat{\phi}_m(\xi) &= 1, & m &= 0, \\ &= \xi_m, & m &= 1, \dots, 4. \end{aligned}$$

Next, the basis functions $\phi_m : \mathcal{K} \rightarrow \mathbb{R}$ are constructed through the parameterization G_K :

$$\phi_m = \hat{\phi}_m \circ G_K^{-1}, \quad m = 0, \dots, 4.$$

We also introduce the basis functions $\psi_m : \mathcal{K} \rightarrow \mathbb{R}$, which are defined as:

$$\begin{aligned} \psi_m(\bar{x}, t) &= 1, & m &= 0, \\ &= \phi_m(\bar{x}, t) - \frac{1}{|K_j(t_{n+1}^-)|} \int_{K_j(t_{n+1}^-)} \phi_m(\bar{x}, t_{n+1}^-) dK, & m &= 1, \dots, 4, \end{aligned} \quad (5)$$

since this will result in a splitting of the test and trial functions into an element mean at time t_{n+1} and a fluctuating part. This property will be beneficial in the definition of the stabilization operator and the multigrid convergence acceleration, discussed in Sections 2.2.5 and 2.3.

The finite element space $V_h^1(\mathcal{T}_h^n)$ is now defined as follows:

$$V_h^1(\mathcal{T}_h^n) := \{U_h \mid U_h|_{\mathcal{K}} \in (P^1(\mathcal{K}))^5\} \subset V(\mathcal{T}_h^n),$$

with the polynomial space $P^1(\mathcal{K}) = \text{span}\{\psi_m, m = 0, \dots, 4\}$. The trial functions $U_h : \mathcal{T}_h^n \rightarrow \mathbb{R}^5$ are defined in each element $\mathcal{K} \in \mathcal{T}_h^n$ as:

$$U_h(\bar{x}, t)|_{\mathcal{K}} \equiv \mathbb{P}(U(\bar{x}, t)|_{\mathcal{K}}) = \sum_{m=0}^4 \hat{U}_m(\mathcal{K}) \psi_m(\bar{x}, t), \quad (6)$$

with $\mathbb{P} : \mathbb{R}^5 \rightarrow V_h^1(\mathcal{T}_h^n)$ the projection operator onto the space V_h^1 and $\hat{U}_m \in \mathbb{R}^5$ the expansion coefficients. The test functions $W_h : \mathcal{T}_h^n \rightarrow \mathbb{R}^5$ are defined analogously, only with \hat{U}_m replaced by \hat{W}_m . The weak formulation for the Euler equations of an inviscid compressible gas can now be formulated as:

Find a $U_h \in V_h^1(\mathcal{T}_h^n)$, such that for all $W_h \in V_h^1(\mathcal{T}_h^n)$, the following variational equation is satisfied:

$$\sum_{n=0}^{N_T} \sum_{j=1}^{N_n} \left\{ \int_{\mathcal{K}_j^n} W_h \cdot \text{div } \mathcal{F}(U_h) d\mathcal{K} + \int_{\mathcal{K}_j^n} ((\text{grad } W_h)^T \cdot \mathfrak{D}(U_h)) : \text{grad } U_h d\mathcal{K} \right\} = 0, \quad (7)$$

with $N_T + 1$ the total number of space-time slabs and N_n the number of elements in the tessellation \mathcal{T}_h^n . The second contribution in (7) is the stabilization operator and added to the weak formulation to prevent numerical oscillations around discontinuities and in regions with sharp gradients, for more details see Section 2.2.5.

2.2.2.2 Transformation of the space-time weak formulation into ALE form

The weak formulation (7) can be transformed into an integrated by parts form using Gauss' theorem. This has as main benefit that it does not result in loss of conservation under inexact quadrature, see e.g. Hansbo (Ref. 25). This approach is for instance followed by Shakib et al. (Ref. 37). It is, however, possible to establish a relation between the Arbitrary Lagrangian Eulerian (ALE) formulation, commonly used on moving and deforming meshes, and the space-time approach. This can be done either directly for the partial differential equations, as presented by Masud and Hughes (Ref. 33), or for the weak formulation using Stokes' theorem, see Bottasso (Ref. 9). In this section we will establish the relation between the space-time and ALE formulation in a more simplified way, which does not require the use of differential forms, and gives more insight into the origin of the various contributions.

If we introduce

$$W_h \cdot \text{div } \mathcal{F}(U_h) = \text{div} (W_h^T \mathcal{F}(U_h)) - (\text{grad } W_h)^T : \mathcal{F}(U_h), \quad (8)$$

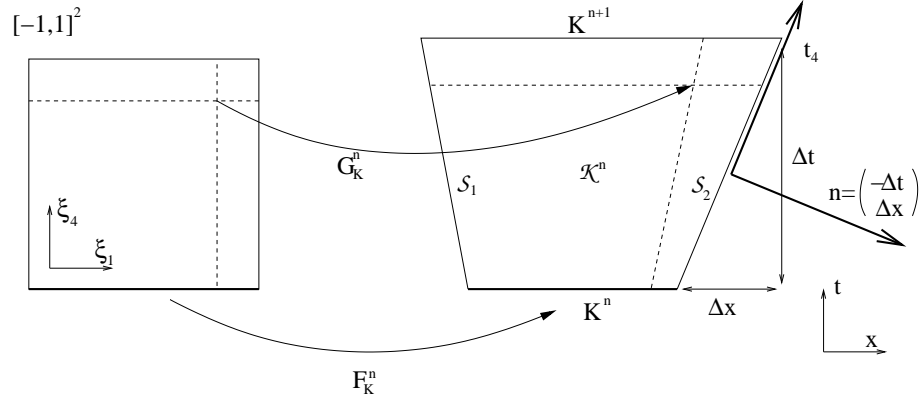


Fig. 1 Illustration of the geometry of two-dimensional space-time elements in both computational and physical space. Notations in the text.

into the weak formulation (7) and apply Gauss' theorem to the contribution resulting from the first term on the righthand side of (8) then we obtain:

$$\int_{\mathcal{K}_j^n} \operatorname{div} (W_h^T \mathcal{F}(U_h)) d\mathcal{K} = \int_{\partial \mathcal{K}_j^n} n_{\mathcal{K}} \cdot ((W_h^-)^T \mathcal{F}(U_h^-)) d(\partial \mathcal{K}), \quad (9)$$

where $n_{\mathcal{K}}$ is the unit outward normal vector at the boundary $\partial \mathcal{K}^n$. The ALE formulation can now be obtained by calculating the normal vector $n_{\mathcal{K}}$.

Given the parameterization $(\bar{x}, t) = G_K^n(\bar{\xi})$ for the space-time element, the normal vector $n_{\mathcal{K}}$ at the boundary surface components \mathcal{S}_{2i-1} and \mathcal{S}_{2i} , $1 \leq i \leq 4$, defined in (4), is orthogonal to the tangential vectors t_{i_1}, t_{i_2} , and t_{i_3} , with the indices $\{i_1, i_2, i_3\} \subset \{1, \dots, 4\}$ complementary to the index $\{i\}$. The tangential vectors are defined as: $t_j = \frac{\partial G_K^n}{\partial \xi_j}$, and are equal to (cf. (3)):

$$t_j = \begin{pmatrix} \frac{1}{2}(1 - \xi_4) \frac{\partial F_K^n(\bar{\xi})}{\partial \xi_j} + \frac{1}{2}(1 + \xi_4) \frac{\partial F_K^{n+1}(\bar{\xi})}{\partial \xi_j} \\ 0 \end{pmatrix}, \quad j = 1, 2, 3,$$

$$t_4 = \frac{1}{2} \begin{pmatrix} F_K^{n+1}(\bar{\xi}) - F_K^n(\bar{\xi}) \\ t_{n+1} - t_n \end{pmatrix} = \frac{1}{2} \begin{pmatrix} \Delta \bar{x} \\ \Delta t \end{pmatrix},$$

(also see Figure 1). The normal vectors at \mathcal{S}_7 and \mathcal{S}_8 are simply $(0, 0, 0, -1)$ and $(0, 0, 0, 1)$, respectively, hence the boundary integrals over the surfaces \mathcal{S}_7 and \mathcal{S}_8 are equal to:

$$\sum_{m=7}^8 \int_{\mathcal{S}_m} n_{\mathcal{K}} \cdot ((W_h^-)^T \mathcal{F}(U_h^-)) d\mathcal{S} = \int_{K_j(t_{n+1}^-)} W_h^- \cdot U_h^- d\mathcal{S} - \int_{K_j(t_n^+)} W_h^- \cdot U_h^- d\mathcal{S}, \quad (10)$$

where we used the relations: $U_h^- = \mathcal{F}_{i_4}(U_h^-)$, $\mathcal{S}_7 = K_j(t_n^+)$ and $\mathcal{S}_8 = K_j(t_{n+1}^-)$.

For the remaining boundary terms remember that for each $\xi_4 \in (-1, 1)$ the element $K(t)$, such that $(K(t), \xi_4) = G_K^n(\bar{\xi}, \xi_4)$, is the space-element defined by the interpolated vertices of the elements $K(t_n^+)$ and $K(t_{n+1}^-)$. Let $\bar{n}_{\mathcal{K}}^i(\bar{x}, t) \in \mathbb{R}^3$, ($1 \leq i \leq 6$), be the space part of the normal vector at the boundary parts $\mathcal{S}_i \subset \mathcal{Q}_j^n$. By definition, $\bar{n}_{\mathcal{K}}^{2m-1}$ and $\bar{n}_{\mathcal{K}}^{2m}$, ($1 \leq m \leq 3$), are perpendicular to the tangential vectors $t_{i_k} = \frac{1}{2}(1 - \xi_4) \frac{\partial F_K^n}{\partial \xi_{i_k}} + \frac{1}{2}(1 + \xi_4) \frac{\partial F_K^{n+1}}{\partial \xi_{i_k}}$, with $k = 1$ or 2 , such that $\{i_1, i_2, m\} = \{1, 2, 3\}$. Hence, the vectors $(\bar{n}_{\mathcal{K}}^i, \alpha) \in \mathbb{R}^4$ are orthogonal to the tangential vectors t_{i_k} , if and only if the conditions:

$$\frac{1}{2} \Delta \bar{x} \cdot \bar{n}_{\mathcal{K}}^i + \frac{1}{2} \alpha \Delta t = 0,$$

are satisfied. The space-time normal vector $n_{\mathcal{K}}^i$ at \mathcal{S}_i , ($1 \leq i \leq 6$), therefore is equal to:

$$n_{\mathcal{K}}^i = (\bar{n}_{\mathcal{K}}^i, -v \cdot \bar{n}_{\mathcal{K}}^i),$$

with the grid velocity $v \in \mathbb{R}^3$ given by the relation: $v = \Delta \bar{x} / \Delta t$. Since the space-time normal vector $n_{\mathcal{K}}$ has length one, the space normal vector $\bar{n}_{\mathcal{K}}$ has a length $|\bar{n}_{\mathcal{K}}| = 1 / \sqrt{1 + v \cdot v}$. The boundary flux integral over \mathcal{S}_i , ($1 \leq i \leq 6$) is now equal to:

$$\sum_{i=1}^6 \int_{\mathcal{S}_i} n_{\mathcal{K}} \cdot ((W_h^-)^T \mathcal{F}(U_h^-)) d\mathcal{S} = \int_{\mathcal{Q}_j^n} [\bar{n}_{\mathcal{K}} \cdot ((W_h^-)^T \bar{\mathcal{F}}(U_h^-)) - \bar{n}_{\mathcal{K}} \cdot v (W_h^- \cdot U_h^-)] d\mathcal{Q}, \quad (11)$$

where the flux tensor $\bar{\mathcal{F}} : \mathbb{R}^5 \rightarrow \mathbb{R}^{5 \times 3}$ has components $\bar{\mathcal{F}}_{ij} = \mathcal{F}_{ij}$ with $1 \leq j \leq 3$. If we replace the righthand side of (9) with the sum of (10) and (11) using the fact that $\partial \mathcal{K}^n = \cup_{i=1}^8 \mathcal{S}_i$, and introduce this relation into (7) we obtain the weak formulation for the Euler equations of gas dynamics in ALE form:

Find a $U_h \in V_h^1(\mathcal{T}_h^n)$, such that for all $W_h \in V_h^1(\mathcal{T}_h^n)$, the following variational equation is satisfied:

$$\begin{aligned} \sum_{n=0}^{N_T} \sum_{j=1}^{N_n} \left\{ - \int_{\mathcal{K}_j^n} (\text{grad } W_h)^T : \mathcal{F}(U_h) d\mathcal{K} + \int_{\mathcal{K}_j(t_{n+1}^-)} W_h^- \cdot U_h^- d\mathcal{K} - \right. \\ \left. \int_{\mathcal{K}_j(t_n^+)} W_h^- \cdot U_h^- d\mathcal{K} + \int_{\mathcal{Q}_j^n} W_h^- \cdot (\bar{\mathcal{F}}(U_h^-) \bar{n}_{\mathcal{K}} - \bar{n}_{\mathcal{K}} \cdot v U_h^-) d\mathcal{Q} + \right. \\ \left. \int_{\mathcal{K}_j^n} ((\text{grad } W_h)^T \cdot \mathfrak{D}(U_h)) : \text{grad } U_h d\mathcal{K} \right\} = 0. \end{aligned} \quad (12)$$

2.2.2.3 Introduction of numerical flux

In the summation over the space-time elements, the integrals over the internal faces of \mathcal{Q}^n , $K(t_n)$ and $K(t_{n+1})$ in the weak formulation (12) are counted twice, since two elements are connected

to each side of the faces. (In case of mesh refinement this applies to subsets of these faces.) This results in a multi-valued flux tensor at internal faces, since in general $U_h^- \neq U_h^+$ in the discontinuous Galerkin discretization, and this requires special care. If we use the fact that the normal flux through the boundary faces must be continuous, almost everywhere, to ensure conservation then we obtain the relations:

$$\begin{aligned} \int_{K_j(t_n^+) \cup K_j(t_{n+1}^-)} W_h^- \cdot U_h^- dK &= \int_{K_j(t_n^+) \cup K_j(t_{n+1}^-)} W_h^- \cdot U_h^+ dK, & \forall W_h \in V_h^1(\mathcal{T}_h^n), \\ \int_{\mathcal{Q}_j^n} W_h^- \cdot (\tilde{\mathcal{F}}(U_h^-) \bar{n}_{\mathcal{K}}) d\mathcal{Q} &= \int_{\mathcal{Q}_j^n} W_h^- \cdot (\tilde{\mathcal{F}}(U_h^+) \bar{n}_{\mathcal{K}}) d\mathcal{Q}, & \forall W_h \in V_h^1(\mathcal{T}_h^n), \end{aligned} \quad (13)$$

with U_h^+ the trace of U_h at $\partial\mathcal{K}_j^n$ of elements connected to \mathcal{K}_j^n . The generalized flux tensor $\tilde{\mathcal{F}} : \mathbb{R}^5 \rightarrow \mathbb{R}^{5 \times 3}$ is defined as:

$$\tilde{\mathcal{F}}(U) = \bar{\mathcal{F}}(U) - v \otimes U,$$

where $v \otimes U = v_i U_j$. The integrals over internal faces $K_j(t_n^+)$ then transform into:

$$\sum_{j=1}^{N_n} \int_{K_j(t_n^+)} W_h^- \cdot U_h^- dK = \sum_{j=1}^{N_n} \int_{K_j(t_n^+)} W_h^- \cdot \frac{1}{2}(U_h^- + U_h^+) dK,$$

with a similar relation for $K_j(t_{n+1}^-)$. The multivalued time flux is now replaced with a numerical flux H_T which, in order to ensure the causality of the time flux, is defined as:

$$\begin{aligned} H_T(U_h^-, U_h^+) &= U_h^+ & \text{at } K_j(t_n^+) \\ &= U_h^- & \text{at } K_j(t_{n+1}^-). \end{aligned}$$

The numerical flux H_T can also be used at the boundary faces $K_j(t_0^+)$, where the external trace is provided by the initial condition at $t = t_0$. The numerical flux H_T makes it possible to drop the summation over the space-time slabs in the weak formulation (12), since each space-time slab only depends on the previous space-time slab. The introduction of the time flux is an alternative to the weak coupling between space-time slabs generally used in time-discontinuous Galerkin methods and results in a uniform treatment of the space-time flux in the DG discretization. Using (13), the integrals over \mathcal{Q}_j^n in (12) can be transformed into:

$$\sum_{j=1}^{N_n} \int_{\mathcal{Q}_j^n} W_h^- \cdot (\tilde{\mathcal{F}}(U_h^-) \bar{n}_{\mathcal{K}}) d\mathcal{Q} = \sum_{j=1}^{N_n} \int_{\mathcal{Q}_j^n} W_h^- \cdot \frac{1}{2}(\tilde{\mathcal{F}}(U_h^-) \bar{n}_{\mathcal{K}} + \tilde{\mathcal{F}}(U_h^+) \bar{n}_{\mathcal{K}}) d\mathcal{Q}. \quad (14)$$

The representation of the flux in (14) as the average between the left and right states at the element face results in a central discretization which suffers from numerical oscillations around discontinuities. Monotone solutions are obtained by adding the stabilization operator and introducing a

Godunov type upwind flux. The use of an upwind flux fits very well into a discontinuous Galerkin discretization, since the states U_h^- and U_h^+ can be considered as the left and right states in a Riemann problem. We replace therefore the flux $\frac{1}{2}(\tilde{\mathcal{F}}(U_h^-(\bar{x}, t))\bar{n}_{\mathcal{K}} + \tilde{\mathcal{F}}(U_h^+(\bar{x}, t))\bar{n}_{\mathcal{K}})$ at the element faces \mathcal{Q}_j^n in the time interval $[t, t + \Delta t)$ with a monotone upwind flux $H(U_h^-, U_h^+)$, which is consistent: $H(U_h, U_h) = \tilde{\mathcal{F}}(U_h)\bar{n}_{\mathcal{K}}$, and conservative: $H(U_h^-, U_h^+) = -H(U_h^+, U_h^-)$. At external boundary faces we apply the same procedure, but at these faces the external state U_h^+ is controlled by the boundary operator: $U_h^+ = \mathcal{B}(U_h^-, U_w)$.

Any of the well-known (approximate) Riemann solvers, such as those from Godunov, Roe, Lax-Friedrichs, or Osher, for a survey see Toro (Ref. 41), can be used as upwind numerical flux. In earlier work, Van der Vegt and Van der Ven (Ref. 43), we used the Osher flux because of its good accuracy and nice mathematical foundation, but the Osher flux is computationally expensive and is replaced with the HLLC flux. The HLLC flux is introduced by Toro, Spruce and Speares (Ref. 40) and further analyzed by Batten et al. (Ref. 5, 6). The HLLC flux provides solutions of at least the same quality as the Osher flux, but at less than one quarter of the computational cost. The definition of the HLLC flux for moving interfaces is provided in Section 2.2.4. An important benefit of using an upwind numerical flux is that this already ensures nearly monotone solutions without a stabilization operator. A relatively simple stabilization operator in comparison with for instance the one used by Shakib, Hughes and Johan (Ref. 37) for the Galerkin least squares finite element method then is sufficient to obtain monotone solutions. The weak formulation for the space-time discontinuous Galerkin finite element discretization of the Euler equations of gas dynamics now is equal to:

Find a $U_h \in V_h^1(\mathcal{T}_h^n)$, such that for all $W_h \in V_h^1(\mathcal{T}_h^n)$, the following variational equation is satisfied:

$$\begin{aligned} \sum_{j=1}^{N_n} \left\{ - \int_{\mathcal{K}_j^n} (\text{grad } W_h)^T : \mathcal{F}(U_h) d\mathcal{K} + \int_{\mathcal{K}_j(t_{n+1}^-)} W_h^- \cdot U_h^- d\mathcal{K} - \right. \\ \left. \int_{\mathcal{K}_j(t_n^+)} W_h^- \cdot U_h^+ d\mathcal{K} + \int_{\mathcal{Q}_j^n} W_h^- \cdot H(U_h^-, U_h^+) d\mathcal{Q} + \right. \\ \left. \int_{\mathcal{K}_j^n} ((\text{grad } W_h)^T \cdot \mathfrak{D}(U_h)) : \text{grad } U_h d\mathcal{K} \right\} = 0. \end{aligned} \quad (15)$$

2.2.3 Equations for the flow field expansion coefficients

An important element in the numerical discretization is the splitting of the test and trial functions into an element mean $\bar{U}_h : \mathcal{T}_h^n \rightarrow \mathbb{R}^5$ at the time level t_{n+1} and a fluctuating part $\tilde{U}_h : \mathcal{T}_h^n \rightarrow \mathbb{R}^5$:

$$U_h(\bar{x}, t) = \bar{U}_h(\mathcal{K}_j(t_{n+1}^-)) + \tilde{U}_h(\bar{x}, t), \quad \forall(\bar{x}, t) \in \mathcal{K}_j^n, \quad (16)$$

with:

$$\bar{U}_h(K_j(t_{n+1}^-)) = \hat{U}_0, \quad (17)$$

$$\int_{K_j(t_{n+1}^-)} \tilde{U}_h(\bar{x}, t) dK = 0. \quad (18)$$

The flow field can now be represented as:

$$U_h(\bar{x}, t) = \bar{U}_h(K_j(t_{n+1}^-)) + \sum_{m=1}^4 \hat{U}_m(\mathcal{K}_j^n) \psi_m(\bar{x}, t), \quad \forall (\bar{x}, t) \in \mathcal{K}_j^n.$$

This splitting is a direct consequence of the fact that the basis functions $\psi_m(\bar{x}, t)$ are constructed such that:

$$\int_{K_j(t_{n+1}^-)} \psi_m(\bar{x}, t_{n+1}^-) dK = 0, \quad m \geq 1, \quad (19)$$

and has several advantages. In the first place, the structure of the space-time discontinuous Galerkin discretization becomes more clear, because the equations for the element mean are identical to a finite volume discretization. A second advantage of the splitting is that it makes it easier to define the stabilization operator and the multigrid convergence acceleration procedure. The stabilization operator does not act on the element mean, only on the fluctuating part. Any adjustment to the element fluctuations due to the stabilization operator will therefore not affect the element mean, and preserve a conservative scheme. The multigrid procedure also benefits from this splitting since it only uses the equations for the element mean at the coarse grid levels. This results in a significant simplification of the multigrid algorithm, while maintaining good multigrid performance.

If we introduce the polynomial expansions (6) for U_h and W_h into the weak formulation of the Euler equations (15), use (16)-(19) and the fact that the coefficients \hat{W} are arbitrary, then the following set of equations for the element mean $\bar{U}_i(K_j(t_{n+1}^-))$, $1 \leq i \leq 5$, is obtained:

$$|K_j(t_{n+1}^-)| \bar{U}_i(K_j(t_{n+1}^-)) - \int_{K_j(t_n^+)} U_{h,i}(\bar{x}, t_n^-) dK + \int_{\mathcal{Q}_j^n} H_i(U_h^-, U_h^+) d\mathcal{Q} = 0. \quad (20)$$

The coefficients for the fluctuating part of the flow field $\hat{U}_{mi}(\mathcal{K}_j^n)$ with $m = 1, \dots, 4$, are equal

to:

$$\begin{aligned}
& \sum_{m=1}^4 \hat{U}_{mi}(\mathcal{K}_j^n) \left(- \int_{\mathcal{K}_j^n} \frac{\partial \psi_l(\bar{x}, t)}{\partial t} \psi_m(\bar{x}, t) d\mathcal{K} + \int_{K_j(t_{n+1}^-)} \psi_l(\bar{x}, t_{n+1}^-) \psi_m(\bar{x}, t_{n+1}^-) dK \right) - \\
& \int_{K_j(t_n^+)} U_{h,i}(\bar{x}, t_n^-) \psi_l(\bar{x}, t_n^+) dK - \bar{U}_i(K_j(t_{n+1}^-)) \int_{\mathcal{K}_j^n} \frac{\partial \psi_l(\bar{x}, t)}{\partial t} d\mathcal{K} + \\
& \int_{\mathcal{Q}_j^n} \psi_l(\bar{x}, t) H_i(U_h^-, U_h^+) d\mathcal{Q} - \int_{\mathcal{K}_j^n} \frac{\partial \psi_l(\bar{x}, t)}{\partial x_k} \bar{\mathcal{F}}_{ik}(U_h) d\mathcal{K} + \\
& \sum_{m=1}^4 \hat{U}_{mi}(\mathcal{K}_j^n) \int_{\mathcal{K}_j^n} \frac{\partial \psi_l(\bar{x}, t)}{\partial x_k} \mathcal{D}_{kp}(U_h) \frac{\partial \psi_m(\bar{x}, t)}{\partial x_p} d\mathcal{K} = 0, \quad l = 1, \dots, 4; i = 1, \dots, 5.
\end{aligned} \tag{21}$$

The computational mesh can be discontinuous at the interface between two space-time slabs. This implies that more than one element in \mathcal{T}_h^{n-1} can connect to the element $\mathcal{K}_j^n \in \mathcal{T}_h^n$. In that case the polynomial representation of $U_h(\bar{x}, t_n^-)$ in the various elements in \mathcal{T}_h^{n-1} which connect to the element \mathcal{K}_j^n must be used in the evaluation of the integrals $\int_{K_j(t_n^+)} U_h(\bar{x}, t_n^-) \psi_l(\bar{x}, t_n^+) dK$. This is discussed in Sections 2.4.1 and 2.4.2. The different contributions in (21) are evaluated separately. Define the geometric coefficients $A^1, A^2, \mathcal{A} \in \mathbb{R}^{5 \times 5}$ as:

$$\begin{aligned}
A_{lm}^1 &= \int_{\mathcal{K}_j^n} \frac{\partial \psi_l(\bar{x}, t)}{\partial t} \psi_m(\bar{x}, t) d\mathcal{K}, \\
A_{lm}^2 &= \int_{K_j(t_{n+1}^-)} \psi_l(\bar{x}, t_{n+1}^-) \psi_m(\bar{x}, t_{n+1}^-) dK, \\
\mathcal{A}_{lm} &= -A_{lm}^1 + A_{lm}^2,
\end{aligned}$$

and the coefficients $B \in \mathbb{R}^{5 \times 5}$, which couple the space-time slabs, as:

$$B_{il}(U_h^+|_{K_j(t_n^+)}) = \int_{K_j(t_n^+)} U_{h,i}(\bar{x}, t_n^-) \psi_l(\bar{x}, t_n^+) dK. \tag{22}$$

The element face and volume flux contributions $\mathcal{R}^1 \in \mathbb{R}^{5 \times 5}$, $\mathcal{R}^2 \in \mathbb{R}^{5 \times 4}$ are defined as:

$$\mathcal{R}_{il}^1(U_h^-|_{\mathcal{Q}_j^n}, U_h^+|_{\mathcal{Q}_j^n}) = \int_{\mathcal{Q}_j^n} \psi_l(\bar{x}, t) H_i(U_h^-, U_h^+) d\mathcal{Q} \tag{23}$$

$$\mathcal{R}_{il}^2(U_h|_{\mathcal{K}_j^n}) = \int_{\mathcal{K}_j^n} \frac{\partial \psi_l(\bar{x}, t)}{\partial x_k} \bar{\mathcal{F}}_{ik}(U_h) d\mathcal{K}, \tag{24}$$

and the integrals of the stabilization operator $\mathcal{D} \in \mathbb{R}^{4 \times 4}$ are denoted as:

$$\mathcal{D}_{lm}(U_h|_{\mathcal{K}_j^n}, U_h^*|_{\mathcal{K}_j^n}) = \int_{\mathcal{K}_j^n} \frac{\partial \psi_l(\bar{x}, t)}{\partial x_k} \mathcal{D}_{kp}(U_h|_{\mathcal{K}_j^n}, U_h^*|_{\mathcal{K}_j^n}) \frac{\partial \psi_m(\bar{x}, t)}{\partial x_p} d\mathcal{K}, \tag{25}$$

with $U_h^*|_{\mathcal{K}_j^n}$ the solution in the elements $\mathcal{K} \in \mathcal{T}_h^n$ which connect to the element \mathcal{K}_j^n . The evaluation of the flux and stabilization operator integrals is discussed in Sections 2.2.4 and 2.2.5, respectively. The system of non-linear equations (21) for the expansion coefficients $\hat{U}_{mi}(\mathcal{K}_j^n)$ can be expressed as:

$$\mathcal{L}(\hat{U}^n, \hat{U}^{n-1}) = 0, \quad (26)$$

with $\hat{U}^n = \hat{U}_{mi}(\mathcal{K})$, $\mathcal{K} \in \mathcal{T}_h^n$, $0 \leq m \leq 4$, $1 \leq i \leq 5$, and $\mathcal{L} : \mathbb{R}^{5 \times 5} \times \mathbb{R}^{5 \times 5} \rightarrow \mathbb{R}^{5 \times 5}$ having components in each space-time element:

$$\mathcal{L}_{i0} = |K_j(t_{n+1}^-)| \bar{U}_i(K_j(t_{n+1}^-)) - B_{i0}(U_h^+|_{K_j(t_n^+)}) + \mathcal{R}_{i0}^1(U_h|_{\mathcal{K}_j^n}, U_h^*|_{\mathcal{K}_j^n}), \quad (27)$$

$$\begin{aligned} \mathcal{L}_{il} &= \sum_{m=1}^4 (\mathcal{A}_{lm}(\mathcal{K}_j^n) + \mathcal{D}_{lm}(U_h|_{\mathcal{K}_j^n}, U_h^*|_{\mathcal{K}_j^n})) \hat{U}_{mi}(\mathcal{K}_j^n) - B_{il}(\hat{U}_h^+|_{K_j(t_n^+)}) - \\ &A_{i0}^1 \bar{U}_i(K_j(t_{n+1}^-)) + \mathcal{R}_{il}^1(U_h^-|_{\mathcal{Q}_j^n}, U_h^+|_{\mathcal{Q}_j^n}) - \mathcal{R}_{il}^2(U_h|_{\mathcal{K}_j^n}), \quad l = 1, \dots, 4. \end{aligned} \quad (28)$$

The space-time discontinuous Galerkin discretization results in a set of non-linear equations (26) for the expansion coefficients \hat{U}^n . This set of non-linear equations is solved with a Full Approximation Storage (FAS) multigrid scheme, which is discussed in Section 2.3. Since the evaluation of the coupling terms B between space-time slabs is fairly complicated for general meshes it is also useful to consider the equations for continuous grid motion. In this case these integrals are relatively simple:

$$B_{il}(U_h^+|_{K_j(t_n^+)}) = \mathcal{B}_{lm} \hat{U}_{mi}(\mathcal{K}_j^{n-1})$$

with:

$$\mathcal{B}_{lm} = \int_{K_j(t_n)} \psi_l(\bar{x}, t_n^+) \psi_m(\bar{x}, t_n^-) dK.$$

If we use the relations $\mathcal{B}_{00} = |K_j(t_n)|$ and $\hat{U}_{0i}(\mathcal{K}_j^{n-1}) = \bar{U}_i(K_j(t_n^-))$ then (27) is a standard finite volume discretization for the element mean.

Remark 2.2.3 *It would have been more convenient to define the element mean flow field for the space-time element \mathcal{K} instead of using the element mean flow field in $K_j(t_{n+1}^-)$, but this would not result in a decoupling of the equations for the element mean from the equations for the fluctuations \tilde{U}_h due to the weak coupling between the different time slabs in the weak formulation (15).*

2.2.4 Flux Calculation

2.2.4.1 Extension of the HLLC scheme to moving meshes

In Section 2.2.2.3 we introduced the HLLC flux into the weak formulation in order to prevent numerical oscillations around discontinuities. The formulation of the HLLC scheme discussed

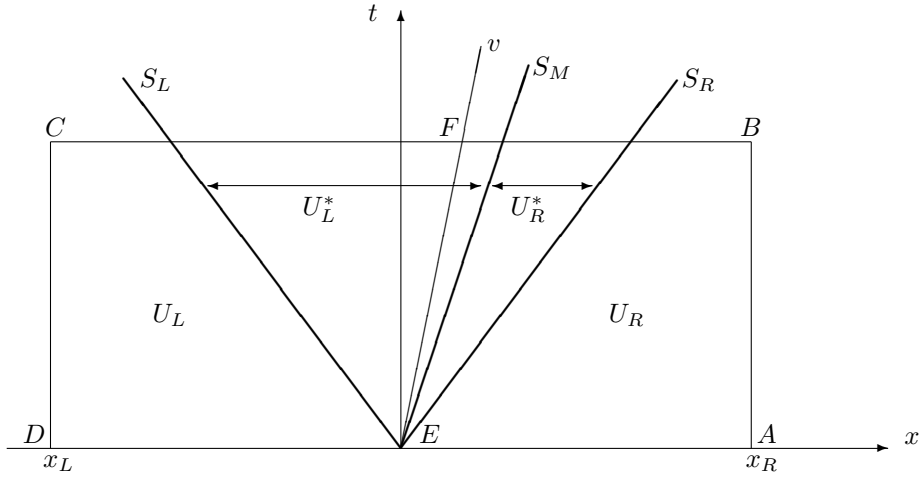


Fig. 2 Wave pattern used in the definition of the HLLC flux function for an element face moving with velocity v . Here S_L and S_R are the fastest left and right moving signal velocities. The solution in the star region U^* is divided by a wave with velocity S_M .

in Toro et al. (Ref. 40, 41) and Batten et al. (Ref. 5, 6) is, however, only valid for non-moving meshes. In this section we will discuss the extension of the HLLC scheme to moving meshes. This extension is most easily accomplished by considering the structure of the wave pattern in the Riemann problem which is assumed in the HLLC scheme, see Figure 2. The HLLC scheme assumes that we have two averaged intermediate states U_L^* and U_R^* in the star region, which is the region bounded by the waves with the slowest and fastest signal speeds S_L and S_R , respectively. The star region is divided into two parts by a contact wave which moves with velocity S_M . Outside the star region the solution still is at its initial values at time t_m , which are denoted U_L and U_R and are equal to the traces $U_h^-(t_m)$ and $U_h^+(t_m)$, respectively. In the time interval $[t_m, t_m + \Delta t)$ the solution U_{HLLC} at an element face which moves with the velocity v then is equal to:

$$U_{HLLC} = \begin{cases} U_L \equiv U_h^-(t_m) & \text{if } S_L > v, \\ U_L^* & \text{if } S_L \leq v < S_M, \\ U_R^* & \text{if } S_M \leq v < S_R, \\ U_R \equiv U_h^+(t_m) & \text{if } S_R \leq v, \end{cases} \quad (29)$$

where depending on the grid velocity v we have to consider four different cases. The time interval Δt is chosen such that there is no interaction with waves coming from other Riemann problems.

Assume that $S_L < v$, $S_R > v$, and $S_M \geq v$, then we can calculate the flux $H_{HLLC}(U_L, U_R)$ in the time interval $[t_m, t_m + \Delta t)$ by integrating the Euler equations over the control volumes $\square DEFC$ and $\square EABF$ as shown in Figure 2. Using Gauss' theorem we obtain for the control

volume $\square DEFC$ the relation:

$$\begin{aligned} & \int_{x_L}^{S_L \Delta t} U_L dx + \int_{S_L \Delta t}^{v \Delta t} U_h(x, t_m + \Delta t) dx \\ &= \int_{x_L}^0 U_h(x, t_m) dx + \int_{t_m}^{t_m + \Delta t} \hat{\mathcal{F}}(U_h(x_L, t)) dt - \int_{t_m}^{t_m + \Delta t} \hat{\mathcal{F}}(U_h^-(vt, t)) dt, \end{aligned} \quad (30)$$

and for the control volume $\square EABF$:

$$\begin{aligned} & \int_{v \Delta t}^{S_M \Delta t} U_h(x, t_m + \Delta t) dx + \int_{S_M \Delta t}^{S_R \Delta t} U_h(x, t_m + \Delta t) dx + \int_{S_R \Delta t}^{x_R} U_R dx \\ &= \int_0^{x_R} U_h(x, t_m) dx + \int_{t_m}^{t_m + \Delta t} \hat{\mathcal{F}}(U_h^+(vt, t)) dt - \int_{t_m}^{t_m + \Delta t} \hat{\mathcal{F}}(U_h(x_R, t)) dt, \end{aligned} \quad (31)$$

with $\hat{\mathcal{F}}(U_h) = \bar{n}_{\mathcal{K}} \bar{\mathcal{F}}(U_h)$. If we introduce now the averaged solutions U_L^* and U_R^* , which are defined as:

$$\begin{aligned} U_L^* &= \frac{1}{(S_M - S_L) \Delta t} \int_{S_L \Delta t}^{S_M \Delta t} U_h(x, t_m + \Delta t) dx, \\ U_R^* &= \frac{1}{(S_R - S_M) \Delta t} \int_{S_M \Delta t}^{S_R \Delta t} U_h(x, t_m + \Delta t) dx, \end{aligned}$$

and use the fact that U_h^\pm is constant along the line $x = vt$ in the Riemann problem then we obtain after subtracting (30) from (31) the following expression for the HLLC flux at the interface in the time interval $[t_m, t_m + \Delta t)$:

$$\begin{aligned} H_{HLLC}(U_L, U_R) &= \frac{1}{2} (\tilde{\mathcal{F}}(U_h^-(vt, t)) + \tilde{\mathcal{F}}(U_h^+(vt, t))) \\ &= \frac{1}{2} (\hat{\mathcal{F}}(U_L) + \hat{\mathcal{F}}(U_R) + ((S_L - v) + (S_M - v))U_L^* + \\ &\quad ((S_R - v) - (S_M - v))U_R^* - S_L U_L - S_R U_R). \end{aligned}$$

For the other three cases: $(S_L < v, S_R > v, S_M \leq v)$, $(S_L < v, S_R < v, S_M < v)$, and $(S_L > v, S_R > v, S_M > v)$ a similar analysis can be made. If we combine the four cases then we obtain the following expression for the HLLC flux at a moving interface in the time interval $[t_m, t_m + \Delta t)$:

$$\begin{aligned} H_{HLLC}(U_L, U_R) &= \frac{1}{2} (\hat{\mathcal{F}}(U_L) + \hat{\mathcal{F}}(U_R) - (|S_L - v| - |S_M - v|)U_L^* + \\ &\quad (|S_R - v| - |S_M - v|)U_R^* + |S_L - v|U_L - |S_R - v|U_R - \\ &\quad v(U_L + U_R)). \end{aligned} \quad (32)$$

In order to completely define the HLLC flux we still need to define the star states U_L^* and U_R^* , and the wave speeds S_L , S_R and S_M . This can be done in various ways, but since there is no difference with the HLLC scheme for non-moving meshes, we only state the final results. We will follow the approach of Batten et al. (Ref. 5) which assumed that:

$$S_M = \hat{u}_L^* = \hat{u}_R^* = \hat{u}^*,$$

with $\hat{u}_{L,R} = \bar{n}_{\mathcal{K}} \cdot u_{L,R}$, and \hat{u}^* the normal velocity calculated from the HLL approximation. This results in the following expression for S_M :

$$S_M = \frac{\rho_R \hat{u}_R (S_R - \hat{u}_R) - \rho_L \hat{u}_L (S_L - \hat{u}_L) + p_L - p_R}{\rho_R (S_R - \hat{u}_R) - \rho_L (S_L - \hat{u}_L)}. \quad (33)$$

The star states are obtained using the Rankine-Hugoniot relations across the waves moving with the velocities S_L and S_R :

$$U_L^* = \frac{S_L - \hat{u}_L}{S_L - S_M} U_L + \frac{1}{S_L - S_M} \begin{pmatrix} 0 \\ (p^* - p_L) \bar{n}_{\mathcal{K}} \\ p^* S_M - p_L \hat{u}_L \end{pmatrix}, \quad (34)$$

with an identical relation for U_R^* , only with L replaced with R . The intermediate pressures are equal to:

$$\begin{aligned} p_L^* &= \rho_L (S_L - \hat{u}_L) (S_M - \hat{u}_L) + p_L, \\ p_R^* &= \rho_R (S_R - \hat{u}_R) (S_M - \hat{u}_R) + p_R, \end{aligned} \quad (35)$$

but the definition of S_M ensures that $p_L^* = p_R^* = p^*$, as is required for a contact discontinuity. The wave speeds S_L and S_R are computed according to Davis (Ref. 20) as:

$$S_L = \min(\hat{u}_L - a_L, \hat{u}_R - a_R), \quad S_R = \max(\hat{u}_L + a_L, \hat{u}_R + a_R), \quad (36)$$

with $a = \sqrt{\gamma p / \rho}$ the speed of sound. Batten et al. (Ref. 6) showed that it is better to use wave velocities based on the Roe averaged velocities, but we did not notice any major difference with the simpler waves velocities defined in (36) for the simulations discussed in these notes.

2.2.4.2 Evaluation of flux integrals

The flux integrals (23) and (24) are computed by transforming the integrals to the reference face $(-1, 1)^3$ and reference element $\hat{\mathcal{K}}$, respectively, after which the integrals are approximated with product Gauss quadrature rules. For the element face flux integrals (23) a two-point product Gauss quadrature rule is used for the integration in the local coordinate directions ξ_1 , ξ_2 and ξ_3 , and a three point Gauss quadrature rule for the integration in the local coordinate direction ξ_4 . The

volume flux integrals (24) are computed with a three-point product Gauss quadrature rule. In Section 3.3.8 Corollary 3.3.16, it is shown that these quadrature rules are sufficiently accurate to ensure that the discontinuous Galerkin discretization discussed in these notes is second order accurate in a suitable Sobolev norm. The product Gauss quadrature rules also evaluate the flux integrals sufficiently accurate to satisfy the Geometric Conservation Law (GCL). The GCL, which is originally formulated by Thomas and Lombard (Ref. 39), requires that a uniform flow field is not disturbed by the grid motion and is an essential condition in order to obtain at least first order accuracy in time, as was proven by Guillard and Farhat (Ref. 24).

The product Gauss quadrature rules are easy to implement, but require 12 flux evaluations per element face integral and 81 flux evaluations per volume integral. This number can be slightly reduced using more sophisticated quadrature rules, as described by Stroud (Ref. 38), but the number of flux evaluations remains large. In Section 3 we describe and analyze a technique to reduce the number of flux evaluations in the flux integration to one, while maintaining the same second order accuracy as obtained with the product Gauss quadrature rules.

2.2.5 Stabilization operator

The discontinuous Galerkin finite element method without stabilization operator does not guarantee monotone solutions around discontinuities and sharp gradients. In these regions numerical oscillations develop when polynomials of degree one or higher are used. For the Runge-Kutta discontinuous Galerkin method Cockburn, Hou and Shu (Ref. 16) derived a local projection or slope limiter which guarantees monotone solutions for multi-dimensional scalar conservation laws. This approach was a major breakthrough for the numerical solution hyperbolic partial differential equations because initially discontinuous Galerkin finite element discretizations experienced severe stability limitations. The use of a slope limiter in combination with a DG method results in a robust numerical discretization and has become quite popular. We have used this technique to compute complex three-dimensional (unsteady) flows for aerodynamical applications in combination with local mesh refinement, Van der Vegt, Van der Ven and Boelens (Ref. 43, 44). Other applications of DG methods with limiters, including higher order discretizations, can be found in Cockburn and Shu (Ref. 17), Cockburn, Karniadakis and Shu (Ref. 19), and Kershaw et al. (Ref. 27).

Despite its robustness the use of a slope limiter has serious disadvantages since it may result in an unnecessary reduction in accuracy in smooth parts of the flow field and prevents convergence to steady state. The accuracy problem has been an important motivation for Cockburn and Shu to look at Total Variation Bounded (TVB) DG discretizations (Ref. 15), but these techniques are not easy to apply in multiple dimensions and contain problem dependent constants which are difficult to estimate. Recently, Burbeau, Sagaut and Bruneau (Ref. 12) proposed limiters for second and

higher order accurate DG methods without problem dependent constants which look promising but still need further testing on real applications.

The problems with the convergence to steady state caused by the limiter are more severe and originate from an inconsistency in the combination of a discontinuous Galerkin discretization and a limiter. Since the limited solution does not satisfy the steady state discontinuous Galerkin equations, it is not possible to reduce the residual to machine accuracy. Instead, the scheme tries to converge to the unlimited solution, which suffers however from numerical oscillations, and the limiter must remain active to prevent this. This is particularly annoying for industrial applications, since it is unclear when to stop the calculations. Convergence to steady state is also important for unsteady problems. In Section 2.3 we solve the non-linear equations for the DG expansion coefficients (26) by introducing a pseudo-time and marching the solution to steady state in pseudo-time with a FAS multigrid algorithm.

The problems in obtaining steady state solutions with a limited DG method are well known, but have received little attention since most applications of DG methods have been to unsteady problems in combination with an explicit Runge-Kutta time integration method. After extensive testing we came to the conclusion that a better alternative is provided by stabilizing the discontinuous Galerkin method by adding artificial dissipation. This approach is also followed by Barth (Ref. 3), Baumann (Ref. 7), Cockburn and Gresho (Ref. 14), and Jaffre, Johnson and Szepessy (Ref. 26) for the discontinuous Galerkin method and is standard in the Streamline Upwind Petrov Galerkin (SUPG) and Galerkin least squares methods. In this section we will discuss new stabilization operators for the space-time discontinuous Galerkin method and in later sections we will demonstrate that this technique provides excellent shock capturing and convergence to steady state in pseudo-time. The stabilization operators use the jump in the polynomial representation at the element faces in the discontinuous Galerkin discretization and the element residual. In this way optimal use is made of the information contained in a DG discretization and we maintain the compact stencil of the discontinuous Galerkin discretization.

The effectiveness of the stabilization operator \mathcal{D} defined in (25), strongly depends on the artificial viscosity matrix $\mathfrak{D}(U_h|_{\mathcal{K}_j^n}, U_h^*|_{\mathcal{K}_j^n}) \in \mathbb{R}^{4 \times 4}$. The definition of the artificial viscosity matrix is more straightforward if the stabilization operator acts independently in all computational coordinate directions. This is achieved by introducing the artificial viscosity matrix $\tilde{\mathfrak{D}} \in \mathbb{R}^{4 \times 4}$ in computational space using the relation:

$$\mathfrak{D}(U_h|_{\mathcal{K}_j^n}, U_h^*|_{\mathcal{K}_j^n}) = R^T \tilde{\mathfrak{D}}(U_h|_{\mathcal{K}_j^n}, U_h^*|_{\mathcal{K}_j^n}) R, \quad (37)$$

where the matrix $R \in \mathbb{R}^{4 \times 4}$ is defined as:

$$R = 2 H^{-1} \text{grad } G_K. \quad (38)$$

The matrix $H \in \mathbb{R}^{4 \times 4}$ is introduced to ensure that both \mathfrak{D} and $\tilde{\mathfrak{D}}$ have the same mesh dependence as a function of h_i , and is defined as:

$$H = \text{diag}(h_1, h_2, h_3, h_4),$$

with $h_i \in \mathbb{R}^+$ the leading terms of the expansion of the mapping G_K (3) in the computational coordinates ξ_i , ($1 \leq i \leq 4$). The multiplication with the factor two in (38) ensures that for orthogonal cells the matrix R is the rotation matrix from the computational space to the physical space. The integrals in the stabilization operator \mathcal{D}_{nm} given by (25) can now be further evaluated, resulting in:

$$\begin{aligned} \mathcal{D}_{nm}(U_h|_{\mathcal{K}_j^n}, U_h^*|_{\mathcal{K}_j^n}) &= \int_{\mathcal{K}_j^n} \frac{\partial \psi_n}{\partial x_k} R_{pk} \tilde{\mathfrak{D}}_{pq}(U_h|_{\mathcal{K}_j^n}, U_h^*|_{\mathcal{K}_j^n}) R_{ql} \frac{\partial \psi_m}{\partial x_l} d\mathcal{K} \\ &= 4 \int_{\hat{\mathcal{K}}} (H^{-1})_{pn} \tilde{\mathfrak{D}}_{pq}(U_h|_{\mathcal{K}_j^n}, U_h^*|_{\mathcal{K}_j^n}) (H^{-1})_{qm} |J_{G_K}| d\hat{\mathcal{K}}, \\ &= \frac{4|\mathcal{K}_j^n|}{h_n^2} \delta_{nm} \tilde{\mathfrak{D}}_{nm}(U_h|_{\mathcal{K}_j^n}, U_h^*|_{\mathcal{K}_j^n}) \end{aligned}$$

(no summation on n), where we used the relations: $(\text{grad } G_K)_{ij} = \partial x_j / \partial \xi_i$ and $\partial \psi_n / \partial \xi_p = \delta_{np}$ and made the assumption that $\tilde{\mathfrak{D}}$ is constant in each element.

The stabilization operator should act only in areas with discontinuities or when the mesh resolution is insufficient. This requirement can be directly coupled to the jump in the solution across element faces and the element residual, respectively, both of which are readily available in the discontinuous Galerkin discretization. In regions with smooth solutions these contributions are of the order of the truncation error and will therefore not reduce the accuracy in these regions. We have tested two models for the artificial coefficients:

Model I. In the artificial viscosity model I only the jump in the pressure across the element faces influences the stabilization matrix. This technique works very well in subsonic and transonic flows with weak shocks. The artificial viscosity matrix is defined as:

$$\begin{aligned} \tilde{\mathfrak{D}}_{qq}(U_h|_{\mathcal{K}_j^n}, U_h^*|_{\mathcal{K}_j^n}) &= \frac{C' \lambda h_q}{|\mathcal{Q}_j^n|} \sum_{m=1}^6 \frac{|p^+(x_{(m)}) - p^-(x_{(m)})| |\mathcal{S}_m|}{p^+(x_{(m)}) + p^-(x_{(m)})}, \quad q = 1, 2, 3, \\ &= 0, \quad \text{otherwise,} \end{aligned}$$

with $p^\pm(x_{(m)}) = \gamma^\pm(p(x_{(m)}))$ the pressure at the centers of the faces $\mathcal{S}_m \subset \mathcal{Q}_j^n$, and γ the trace operator. The scaling factor λ is defined as: $\lambda = |\bar{n}_{\mathcal{K}} \cdot (u - v)| + a$, and is the maximum

of the eigenvalues of the flux Jacobians $\partial\bar{\mathcal{F}}/\partial U$ at the midpoints $x_{(m)}$ of the faces \mathcal{S}_m , with $\bar{n}_{\mathcal{K}}$ the space normal at \mathcal{Q}_j^n , u and v the fluid and grid velocity, and $a = \sqrt{\gamma p/\rho}$ the speed of sound. The constant C' is of order one. Other discontinuity sensors, based for instance on the density, have also been tested, but the difference with the pressure sensor generally was very small.

Model II. For problems with stronger discontinuities the artificial viscosity model proposed and analyzed by Jaffre, Johnson and Szepessy (Ref. 26) is used. In this model both the jumps at the element faces and the element residual are used to define the artificial viscosity:

$$\begin{aligned} \tilde{\mathcal{D}}_{qq}(U_h|_{\mathcal{K}_j^n}, U_h^*|_{\mathcal{K}_j^n}) &= \max(C_2 h_{\mathcal{K}}^{2-\beta} R_q(U_h|_{\mathcal{K}_j^n}, U_h^*|_{\mathcal{K}_j^n}), C_1 h_{\mathcal{K}}^{\frac{3}{2}}), & q = 1, 2, 3, \\ &= 0, & \text{otherwise,} \end{aligned}$$

with

$$\begin{aligned} R(U_h|_{\mathcal{K}_j^n}, U_h^*|_{\mathcal{K}_j^n}) &= \left| \sum_{k=0}^3 \frac{\partial \mathcal{F}(U_h)}{\partial U_{h,i}} \frac{\partial U_{h,i}(G_K(0))}{\partial x_k} \right| + C_0 |U_h^+(x_{(\tau)}) - U_h^-(x_{(\tau)})|/h_{\mathcal{K}} + \\ &\quad \sum_{m=1}^6 \frac{1}{h_{\mathcal{K}}} |\bar{n}_{\mathcal{K}}^T \tilde{\mathcal{F}}(U_h^+(x_{(m)})) - \bar{n}_{\mathcal{K}}^T \tilde{\mathcal{F}}(U_h^-(x_{(m)}))|, \end{aligned} \quad (39)$$

with $h_{\mathcal{K}} = \sqrt{h_1^2 + h_2^2 + h_3^2 + h_4^2}$ and $U_{h,i}$ the components of U_h . The coefficients β , C_0 , C_1 and C_2 are positive constants and set equal to $C_0 = 1.2$, $C_1 = 0.1$, $C_2 = 1.0$ and $\beta = 0.1$. For stronger shocks the addition of the quasi-linear form of the conservation law in (39), which is the first contribution on the righthand side of (39), significantly improves the robustness of the numerical scheme, since this contribution detects discontinuities very well. Numerical tests showed that the contributions of the element residual of the quasi-linear equations and the contributions in the jump of the flux at the element faces are equally important.

2.3 Solution of the non-linear DG coefficient equations

2.3.1 Multigrid algorithm for pseudo-time integration

The space-time discontinuous Galerkin discretization results in each element in a system of coupled non-linear equations for the expansion coefficients \hat{U}^n . In this section we will describe an efficient multigrid technique to solve these non-linear equations. The use of a multigrid scheme is motivated by the fact that it maintains the local, element based structure of the discontinuous Galerkin discretization when a proper relaxation scheme is chosen. This greatly facilitates the use of a domain decomposition technique on parallel computers, which are our main target platforms. The multigrid technique has only been discussed for the linear advection-diffusion equation by

Gopalakrishnan and Kanschat (Ref. 22), which theoretically analyzed its performance. Until now multigrid techniques have not been used for DG discretizations of the Euler equations and on locally refined meshes. The development of an efficient technique has turned out to be non-trivial.

The non-linear equations of the space-time discontinuous Galerkin discretization (26) are solved by augmenting them with a pseudo-time derivative:

$$|K_j(t_{n+1}^-)| \frac{\partial \hat{U}(\mathcal{K}_j^n)}{\partial \tau} = -\frac{1}{\Delta t} \mathcal{L}(\hat{U}^n, \hat{U}^{n-1}), \quad (40)$$

where the righthand side of (40) is divided by Δt to make it possible to obtain also steady state solutions as $\Delta t \rightarrow \infty$, because $\frac{1}{\Delta t} \mathcal{L}$ is independent of Δt . The system (40) is integrated in pseudo-time using an optimized Runge-Kutta scheme in combination with a FAS multigrid algorithm to accelerate the convergence to steady state. On the coarse meshes only the equations for element mean are used. Depending on the type of artificial dissipation we must, however, modify the Runge-Kutta scheme.

We define the following five stage semi-implicit Runge-Kutta scheme as relaxation operator for the multigrid procedure:

Procedure $S_I^k(k, \mathcal{L}^k, \mathcal{F}_O^k, \hat{W}^k)$:

1. Initialize the first Runge-Kutta stage: $\hat{V}^{(0)} = \hat{W}^k$.
2. Do for all stages $s = 1$ to 5:

$$\begin{aligned} & \left(I + \frac{\alpha_s \bar{\lambda}}{|K^n|} (|K^n| I + \bar{\mathcal{D}}^k(\hat{V}^{(s-1)})) \right) \hat{V}^{(s)} = \\ & \hat{V}^{(0)} + \frac{\alpha_s \bar{\lambda}}{|K^n|} \left((|K^n| I + \bar{\mathcal{D}}^k(\hat{V}^{(s-1)})) \hat{V}^{(s-1)} - \mathcal{L}^k(\hat{V}^{(s-1)}, \hat{U}^k(\mathcal{K}^{n-1})) + \mathcal{F}_O^k \right) \end{aligned} \quad (41)$$

3. End do
4. Update solution: $\hat{W}^k = \hat{V}^{(5)}$.

End Procedure S_I^k ,

with $K^n = K_j(t_{n+1}^-)$. In this procedure \hat{W}^k are approximations to the expansion coefficients $\hat{U}(\mathcal{K}^n)$ at the different grid levels k , $\hat{U}^k(\mathcal{K}^{n-1})$ are the expansion coefficients of the restriction of $U_h(\mathcal{K}^{n-1})$ to the grid level k , and \mathcal{F}_O^k represents the forcing function, which is defined in Procedure FAS. At the fine grid level $k = M$, the non-linear operator $\mathcal{L}^M : \mathbb{R}^{5 \times 5} \times \mathbb{R}^{5 \times 5} \rightarrow \mathbb{R}^{5 \times 5}$ satisfies: $\mathcal{L}^M = \mathcal{L}$, with \mathcal{L} defined in (27)-(28), and we have $\hat{U}^M, \hat{V}^M, \hat{W}^M, \hat{\mathcal{F}}_O^M \in \mathbb{R}^{5 \times 5}$. At the coarse grid levels $1 \leq k < M$ the components of the operators $\mathcal{L}^k : \mathbb{R}^5 \times \mathbb{R}^5 \rightarrow \mathbb{R}^5$ are



equal to: $\mathcal{L}_i^k = \mathcal{L}_{i0}$, and we have $\hat{V}^k, \hat{W}^k, \hat{\mathcal{F}}_O^k \in \mathbb{R}^5$. The coefficients $\hat{U}^k \in \mathbb{R}^5$ only consist of the coefficients of the mean flow field \hat{U}_{0i} and the coefficient $\bar{\lambda}$ is defined as: $\bar{\lambda} = \frac{\Delta\tau}{\Delta t}$, with $\Delta\tau$ the time step in the pseudo-time integration. The Runge-Kutta coefficients α_s are defined as: $\alpha_1 = 0.0791451, \alpha_2 = 0.163551, \alpha_3 = 0.283663, \alpha_4 = 0.5, \text{ and } \alpha_5 = 1.0$, and optimized with a searching technique to improve the stability and smoothing properties of the Runge-Kutta scheme. The matrix $\bar{\mathcal{D}}^M \in \mathbb{R}^{5 \times 5}$ is defined as:

$$\bar{\mathcal{D}}^M = \begin{pmatrix} 0 & 0 \\ 0 & \mathcal{D} \end{pmatrix},$$

at the fine grid level, with the dissipation matrix $\mathcal{D} \in \mathbb{R}^{4 \times 4}$ given by (25), and $\bar{\mathcal{D}}^k$ is zero at the coarse grid levels. Note, the dissipation operators discussed in Section 2.2.5 both result in a diagonal matrix, hence the implicit treatment of this contribution is straightforward. The matrix $I \in \mathbb{R}^{5 \times 5}$ represents the identity matrix.

The Runge-Kutta scheme (41) is obtained from a second order accurate five-stage Runge-Kutta method:

$$\hat{V}^{(s)} = \hat{V}^{(0)} - \frac{\alpha_s \bar{\lambda}}{|K^n|} \mathcal{L}^k(\hat{V}^{(s-1)}, \hat{U}^k(\mathcal{K}^{n-1})), \quad \text{for } s = 1, \dots, 5, \quad (42)$$

by treating \hat{V} in $\mathcal{L}^k(\hat{V}, \hat{U}^k(\mathcal{K}^{n-1}))$ semi-implicitly. This is accomplished by approximating $(\bar{\mathcal{A}} + \bar{\mathcal{D}})\hat{V}$ as: $(|K^n|I + \bar{\mathcal{D}})\hat{V}^{(s)} + (\bar{\mathcal{A}} - |K^n|I)\hat{V}^{(s-1)}$. Here $\bar{\mathcal{A}}$ is the coefficient matrix multiplying \hat{V} in (27) and (28). The contribution $\alpha_s \bar{\lambda} (|K^n|I + \bar{\mathcal{D}})\hat{V}^{(s-1)} / |K^n|$ then is added and subtracted to the righthand side of (42) to restore the operator \mathcal{L}^k . This makes it possible to have a residual $\mathcal{L}^k(\hat{U}^n, \hat{U}^{n-1}) \approx 0$ when the solution converges to a steady state, which facilitates the definition of the multigrid algorithm.

The semi-implicit Runge-Kutta scheme is necessary because the pseudo-time integration would otherwise become unstable for values of $\bar{\lambda}$ of the order of one. The use of a semi-implicit Runge-Kutta scheme was proposed by Melson, Sanetrik and Atkins (Ref. 34) for time-accurate calculations with multigrid acceleration using a Jameson type finite volume discretization of the compressible Navier-Stokes equations. In Section 2.3.2 we analyze this procedure and show that for small values of $\bar{\lambda}$ it also greatly enhances the stability of the pseudo-time integration method for the space-time discontinuous Galerkin discretization.

The multigrid procedure also requires the definition of the coarse grid meshes and the restriction and prolongation operator. The unadapted mesh is generated such that it has a sufficient number of coarse grid levels. For most calculations at least three levels are used. In general the mesh is also

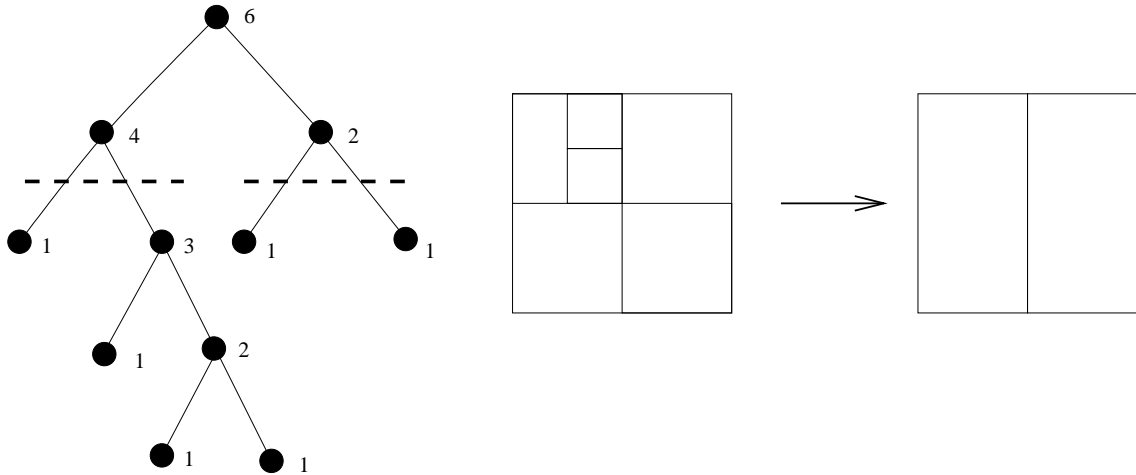


Fig. 3 Coarsening based on refinement tree. The numbers at the nodes of the tree refer to the number of leaves in the subtree. The dashed lines show where the tree is pruned. The fine grid cells and the resulting coarse grid cells are shown to the right.

locally refined, and starting at the leaves of the refinement tree, we traverse the tree backwards until a sufficiently large number of cells is merged into coarse grid cells. The ratio of the number of cells between two grid levels is approximately eight in three dimensions. In Figure 3 an example of this process is given. This process results in a number of tessellations $\mathcal{T}_{h,k}^n$, $1 \leq k \leq M$, for each grid level, which are defined as:

$$\mathcal{T}_{h,k}^n := \{\mathcal{K}_{j,k}^n \mid \mathcal{K}_{j,k}^n = \cup_{j' \in I_{j,k}} \mathcal{K}_{j'}^n, \mathcal{K}_{j'}^n \in \mathcal{T}_h^n\},$$

with $I_{j,k}$ the indices of the elements $\mathcal{K}_{j'}^n$ which agglomerate into the coarse grid element $\mathcal{K}_{j,k}^n$. Note, at the fine grid level $k = M$ we have $\mathcal{T}_{h,M}^n = \mathcal{T}_h^n$. An example of tree multigrid levels in a locally refined mesh is given in Figure 4.

We also have to correct for the fact that the agglomerated coarse grid cells are not necessarily hexahedral elements. This does not give serious problems since at the coarse grid levels we only use equations for the element mean. These equations are identical to a first order accurate finite volume discretization for which it is straightforward to obtain a discretization on agglomerated elements. This is considerably more complicated for a second or higher order accurate discontinuous Galerkin discretization, which also uses the equations for the flow field fluctuations, and is one of the main reasons for only using the equations for the element mean on the coarse grid levels.

For the discretization at the coarse grid levels we introduce the approximation spaces $V_{h,k}$, which

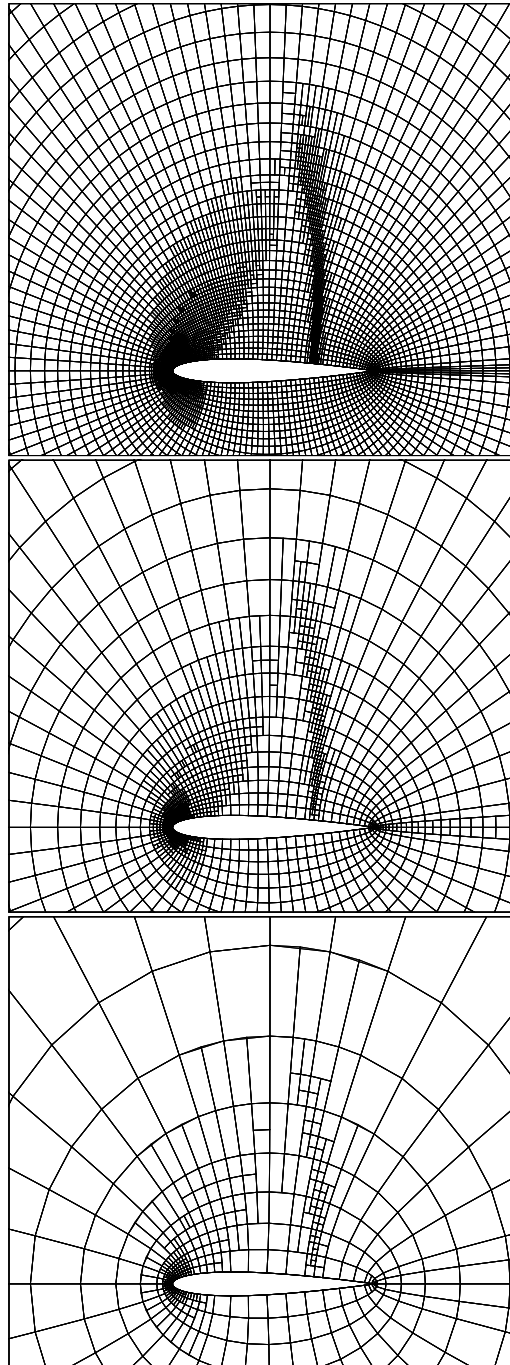


Fig. 4 Multigrid levels in an adapted mesh about the NACA 0012 airfoil.

are defined as:

$$V_{h,k}(\mathcal{T}_{h,k}^n) := \begin{cases} \{U_h \mid U_h|_{\mathcal{K}} = \bar{U}(K(t_{n+1}^-)), \forall \mathcal{K} \in \mathcal{T}_{h,k}^n\} & \text{if } 1 \leq k < M, \\ V^1(\mathcal{T}_h^n) & \text{if } k = M. \end{cases}$$

The restriction operator $I_k^{k-1} : V_{h,k}(\mathcal{T}_{h,k}^n) \rightarrow V_{h,k-1}(\mathcal{T}_{h,k-1}^n)$ is a volume weighted average and is defined as:

$$I_k^{k-1} U_h|_{\mathcal{K}_j^n} = \frac{\sum_{j' \in I_{j,k}} \hat{U}_{0i}(\mathcal{K}_{j'}^n) |\mathcal{K}_{j'}^n|}{\sum_{j' \in I_{j,k}} |\mathcal{K}_{j'}^n|}, \quad (43)$$

with $\mathcal{K}_j^n \in \mathcal{T}_{h,k}^n$. The prolongation operator $I_{k-1}^k : V_{h,k-1}(\mathcal{T}_{h,k-1}^n) \rightarrow V_{h,k}(\mathcal{T}_{h,k}^n)$ is a pure injection and defined as:

$$I_{k-1}^k U_h|_{\mathcal{K}_{j,k}^n} = \bar{U}(K_{j,k}(t_{n+1}^-)), \quad (44)$$

for all fine grid elements $\mathcal{K}_j \in \mathcal{T}_{h,k}^n$ which agglomerate into the coarse grid element $\mathcal{K}_{j,k}^n$. We can now define a FAS multigrid algorithm for the space-time discontinuous Galerkin discretization on locally refined meshes:

Procedure FAS($k, \mathcal{L}^k, \mathcal{F}_O^k, \hat{W}^k$):

1. Do m_1 Runge-Kutta steps $S^k(k, \mathcal{L}^k, \mathcal{F}_O^k, \hat{W}^k)$ at grid level k .
2. Compute forcing function:

$$F_O^{k-1} = \mathcal{L}^{k-1}(I_k^{k-1} \hat{W}^k, I_k^{k-1} \hat{U}^k(\mathcal{K}^{n-1})) + I_k^{k-1}(\mathcal{F}_O^k - \mathcal{L}^k(\hat{W}^k, \hat{U}^k(\mathcal{K}^{n-1}))),$$

with $\mathcal{F}_O^M = 0$.

3. If $k > 0$ Do Procedure FAS($k-1, \mathcal{L}^{k-1}, \mathcal{F}_O^{k-1}, \hat{W}^{k-1}$)
4. Update element mean solution at grid level k : $\hat{W}_{i0}^k = \hat{W}_{i0}^k + I_{k-1}^k(\hat{W}_{i0}^{k-1} - I_k^{k-1} \hat{W}_{i0}^k)$.
5. Do m_2 Runge-Kutta steps $S^k(k, \mathcal{L}^k, \mathcal{F}_O^k, \hat{W}^k)$ at level k .

End Procedure FAS.

In the definition of the Procedure FAS we used (17)-(18), which allow us to apply the restriction and prolongation operator directly to the coefficients \hat{U} without first projecting U_h to the basis functions ψ_m . The Procedure FAS uses a V-cycle multigrid strategy. Other cycling strategies, such as the W-cycle can be obtained with minor changes to the Procedure FAS. The present multigrid algorithm makes rather crude assumptions at the coarse grid levels, but has a good performance in practice. An example is given in Figure 5 for calculations of the transonic flow about a NACA 0012 airfoil on a locally refined mesh. This figure shows that after each adaptation step,

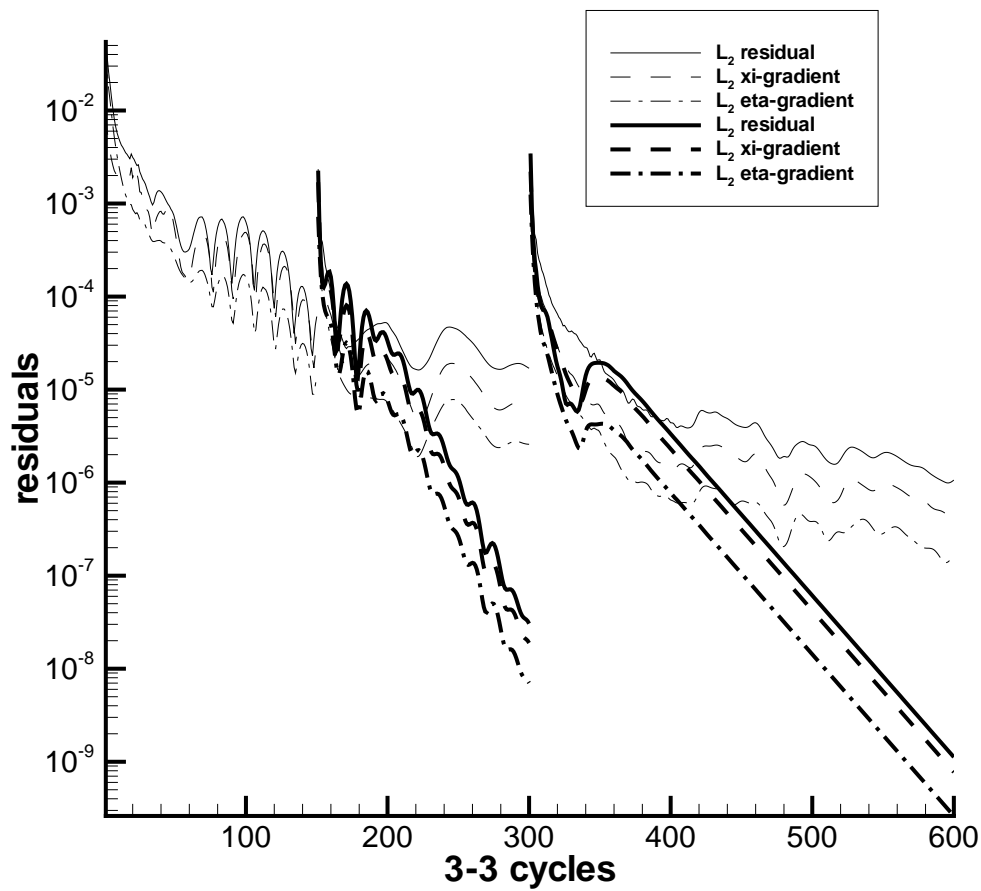


Fig. 5 Convergence rate comparison of the residual for the element mean and fluctuating DG coefficient equations using single and multigrid computations (dark lines) on a twice adapted mesh of a NACA 0012 airfoil.

which result in the peaks in the residual, the residual is efficiently reduced by the multigrid procedure, both for the equations of the element mean and the fluctuations. We have extensively tested several other multigrid strategies, including solving the equations for the flow field fluctuations \hat{U}_{mi} , $m \geq 1$ also on the coarse meshes and more elaborate restriction and prolongation operators. Although some of these methods were promising in a two-level smoothing analysis, and their theoretical performance was verified in calculations on simple model problems, none of these techniques came close to the performance of the multigrid algorithm for the solution of the Euler equations discussed in this section.

2.3.2 Stability analysis of pseudo-time integration

In this section we investigate the stability of the pseudo-time integration method discussed in Section 2.3.1. As a model problem we use the linear advection equation:

$$\frac{\partial u}{\partial t} + a \frac{\partial u}{\partial x} = 0,$$

with $a > 0$ a positive constant. This results in a relatively simple linear system, which is useful for analyzing the properties of the numerical discretization. The space-time discontinuous Galerkin discretization for the linear advection equation using a mesh with grid velocities $s_j \leq a$, $j = 1, \dots, N$, with N the number of mesh points, can be represented in matrix form as:

$$\mathcal{A}\hat{U}(\mathcal{K}_j^n) - \mathcal{B}\hat{U}(\mathcal{K}_{j-1}^n) = \mathcal{C}\hat{U}(\mathcal{K}_j^{n-1}),$$

with:

$$\mathcal{A} = \begin{pmatrix} \Delta x_j^{n+1} + c_{j+\frac{1}{2}}^n & c_{j+\frac{1}{2}}^n & -c_{j+\frac{1}{2}}^n \\ 2a_1 + c_{j+\frac{1}{2}}^n - 2a\Delta t_n & \frac{1}{3}a_2 + c_{j+\frac{1}{2}}^n + d_{11} & -2a_1 - c_{j+\frac{1}{2}}^n + 2a\Delta t_n \\ -\Delta x_j^n - \Delta x_j^{n+1} - c_{j+\frac{1}{2}}^n & -c_{j+\frac{1}{2}}^n & \frac{2}{3}a_3 + \frac{4}{3}c_{j+\frac{1}{2}}^n + d_{22} \end{pmatrix}$$

$$\mathcal{B} = \begin{pmatrix} c_{j-\frac{1}{2}}^n & c_{j-\frac{1}{2}}^n & -c_{j-\frac{1}{2}}^n \\ -c_{j-\frac{1}{2}}^n & -c_{j-\frac{1}{2}}^n & c_{j-\frac{1}{2}}^n \\ -c_{j-\frac{1}{2}}^n & -c_{j-\frac{1}{2}}^n & \frac{4}{3}c_{j-\frac{1}{2}}^n \end{pmatrix}, \quad \mathcal{C} = \begin{pmatrix} \Delta x_j^n & 0 & 0 \\ 0 & \frac{1}{3}\Delta x_j^n & 0 \\ -2\Delta x_j^n & 0 & 0 \end{pmatrix},$$

with $\Delta x_j^n = x_{j+1}^n - x_j^n$, $\bar{x}_j^n = \frac{1}{2}(x_j^n + x_{j+1}^n)$, $a_1 = \bar{x}_j^{n+1} - \bar{x}_j^n$, $a_2 = 2\Delta x_j^{n+1} - \Delta x_j^n$, $a_3 = 2\Delta x_j^n + \Delta x_j^{n+1}$, $c_{j\pm\frac{1}{2}}^n = \Delta t_n(a - s_{j\pm\frac{1}{2}})$, and $s_{j+\frac{1}{2}}^{n+1} = (x_{j+1}^{n+1} - x_{j+1}^n)/\Delta t_n$. Here x_j^n and x_{j+1}^n denote the begin and end points of the element at time t_n , respectively. The terms d_{11} and d_{22} are determined by the artificial dissipation operator.



For the stability analysis we assume that the time step, element size, and velocity remain constant, i.e. $\Delta t = \Delta t_n$, $\Delta x = \Delta x_j^{n+1} = \Delta x_j^n$, and $s = s_{j-\frac{1}{2}}^n = s_{j+\frac{1}{2}}^n$ for all j and n , and set the artificial viscosity coefficients equal to zero, then the operator \mathcal{L} can be expressed as:

$$\mathcal{L}(\hat{U}^n, \hat{U}^{n-1}) = \mathcal{A}\hat{U}(\mathcal{K}_j^n) - \mathcal{B}\hat{U}(\mathcal{K}_{j-1}^n) - \mathcal{C}\hat{U}(\mathcal{K}_j^{n-1}), \quad (45)$$

with the matrices $\mathcal{A}, \mathcal{B}, \mathcal{C} \in \mathbb{R}^{3 \times 3}$ defined as:

$$\mathcal{A} = \begin{pmatrix} 1 + \delta & \delta & -\delta \\ -\delta & \frac{1}{3} + \delta & \delta \\ -2 - \delta & -\delta & 2 + \frac{4}{3}\delta \end{pmatrix}, \quad \mathcal{B} = \begin{pmatrix} \delta & \delta & -\delta \\ -\delta & -\delta & \delta \\ -\delta & -\delta & \frac{4}{3}\delta \end{pmatrix}, \quad \mathcal{C} = \begin{pmatrix} 1 & 0 & 0 \\ 0 & \frac{1}{3} & 0 \\ -2 & 0 & 0 \end{pmatrix},$$

with $\delta = \Delta t(a - s)/\Delta x$ and $s \leq a$. The Runge-Kutta scheme (41) is used for the pseudo-time integration. Consider now the spatial Fourier mode:

$$\hat{U}(\mathcal{K}_j^n) = e^{i\theta j} \hat{U}^F,$$

with $\theta \in [0, 2\pi)$ and $i = \sqrt{-1}$. Since the stability of the pseudo-time integration is determined by the transients we only consider the homogeneous part of the equation for the Fourier coefficient \hat{U}^F :

$$\frac{d\hat{U}^F}{d\tau} = -\frac{1}{\Delta t} \mathcal{P}(\theta) \hat{U}^F, \quad (46)$$

with $\mathcal{P}(\theta) = \mathcal{A} - e^{-i\theta} \mathcal{B}$. The matrix $\mathcal{P} \in \mathbb{R}^{3 \times 3}$ is non-singular and we can write \mathcal{P} as: $\mathcal{P} = QMQ^{-1}$, with Q the matrix of right eigenvectors and M the diagonal matrix with the eigenvalues $\mu_m(\theta)$, ($m = 0, 1, 2$) of $\mathcal{P}(\theta)$. Introducing a new vector $\hat{V}^F = Q^{-1} \hat{U}^F$ then (46) becomes a system of uncoupled ordinary differential equations:

$$\frac{d\hat{V}_m^F}{d\tau} = -\frac{\mu_m(\theta)}{\Delta t} \hat{V}_m^F, \quad \text{for } m = 0, 1, 2.$$

This system of ordinary differential equations is solved with the semi-implicit Runge-Kutta scheme (41), which has an amplification factor $G(z)$, with $z \in \mathbb{C}$. The pseudo-time integration method is stable if the amplification factor G satisfies the condition $|G(z_m(\theta))| \leq 1$, for $m = 0, 1, 2$; $\theta \in [0, 2\pi)$ with $z_m(\theta)$ defined as $z_m(\theta) = -\frac{\Delta\tau}{\Delta t} \mu_m(\theta)$. The stability is analyzed for different values of the physical and pseudo-time step CFL-numbers (defined as $CFL_{\Delta t} = a\Delta t/\Delta x$ and $CFL_{\Delta\tau} = a\Delta\tau/\Delta x$, respectively), and the ratio s/a .

In Figure 6 contour values of the stability domain $|G(z)| \leq 1$ for the 5-stage semi-implicit Runge-Kutta scheme (41) with optimized coefficients are shown for the physical CFL numbers $CFL_{\Delta t} =$

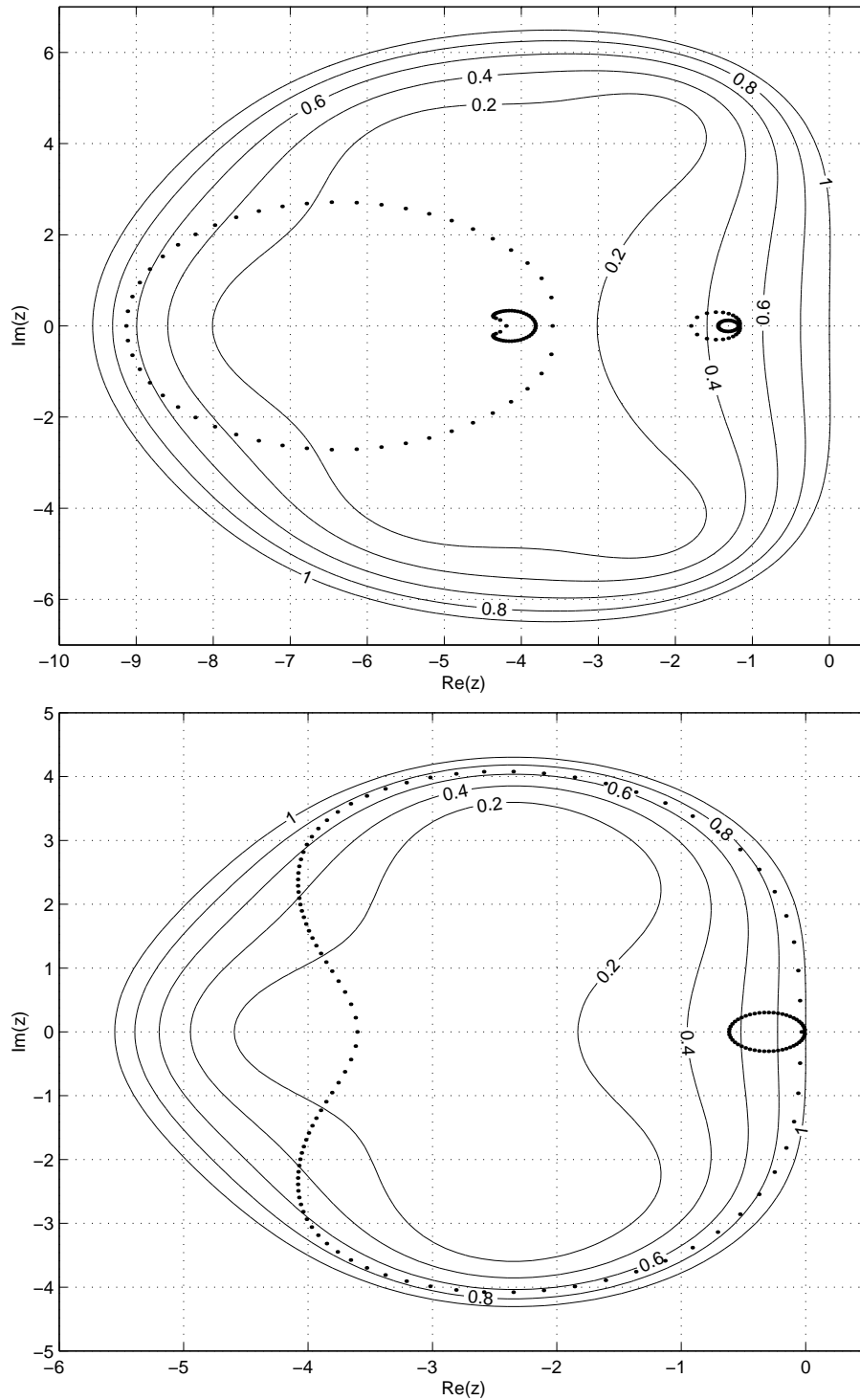


Fig. 6 Locus of the eigenvalues $z_m(\theta)$, $\theta \in [0, 2\pi)$, (dots) of the DG discretization of $u_t + au_x = 0$ and the stability domain of the 5-stage semi-implicit Runge-Kutta method with optimized coefficients. $CFL_{\Delta t} = 1.0$, $CFL_{\Delta \tau} = 1.8$ (top), $CFL_{\Delta t} = 100.0$, $CFL_{\Delta \tau} = 1.8$ (bottom), no grid velocity.



1 and 100, respectively. Also shown are the locus of the eigenvalues $z_m(\theta)$, $\theta \in [0, 2\pi)$, which must be inside the stability region to ensure the stability of the pseudo-time integration. For $CFL_{\Delta t} = 1$ the Runge-Kutta scheme is stable for $CFL_{\Delta \tau} \leq 1.94$ and for $CFL_{\Delta t} = 100$ the pseudo-time step CFL number must be less than $CFL_{\Delta \tau} \leq 1.85$, which is unchanged for larger values of $CFL_{\Delta t}$. The large stability domain and excellent smoothing properties of the semi-implicit Runge-Kutta method for small values of the physical time step CFL number is important for time-accurate simulations.

In Figure 7 the effect of the semi-implicit treatment of \hat{V} in (41) is shown for $CFL_{\Delta t} = 1$. For small physical time step CFL numbers the stabilizing effect of this technique is very large and the pseudo-time step CFL number must be reduced to 1.08 to ensure stability when the semi-implicit technique is not used. For physical CFL numbers larger than 100 the effect of the semi-implicit Runge-Kutta scheme is, however, negligible. The effect of using optimized coefficients in the Runge-Kutta scheme (41) is also large, as can be seen in Figure 7 where the stability contours for the semi-implicit Runge-Kutta scheme with coefficients $\alpha_s = \frac{1}{4}, \frac{1}{6}, \frac{3}{8}, \frac{1}{2}, 1$ for the stages $s = 1, \dots, 5$ are shown. This are the coefficients for the Jameson Runge-Kutta scheme, which is a popular Runge-Kutta method in computational fluid dynamics and also frequently used as a smoother in multigrid algorithms. For this Runge-Kutta scheme the pseudo-time CFL number must be reduced to $CFL_{\Delta \tau} \leq 0.88$, when the physical CFL number is equal to $CFL_{\Delta t} = 1$. When the physical CFL number is equal to $CFL_{\Delta t} = 100$ then the pseudo-time CFL number must be reduced to $CFL_{\Delta \tau} \leq 0.95$ for the Jameson Runge-Kutta scheme. The effect of grid velocity is stabilizing if the grid velocity is in the range $0 \leq s \leq a$. This is a direct consequence of the relation $\delta = CFL_{\Delta t}(1 - s/a)$. When the grid velocity is in this range then it reduces the effective physical time step CFL number and since the pseudo-time integration has a larger stability domain for smaller values of $CFL_{\Delta t}$ this improves stability.

2.4 Mesh adaptation

In order to improve the accuracy of the discontinuous Galerkin discretization the computational mesh is adapted to provide more resolution in important flow structures. The mesh adaptation procedure is based on anisotropic refinement and coarsening of the mesh by subdividing and merging elements, independently in each of the local coordinate directions ξ_i , ($1 \leq i \leq 4$), of the reference element. The data structures and searching techniques for local mesh refinement and coarsening, which are suitable for the space-time discontinuous Galerkin finite element discretization, are essentially the same as discussed in Van der Vegt and Van der Ven (Ref. 43). The mesh adaptation is controlled with a sensor function which is based on the following quantities:

- shock sensor, which measures differences in flow quantities and total pressure loss across

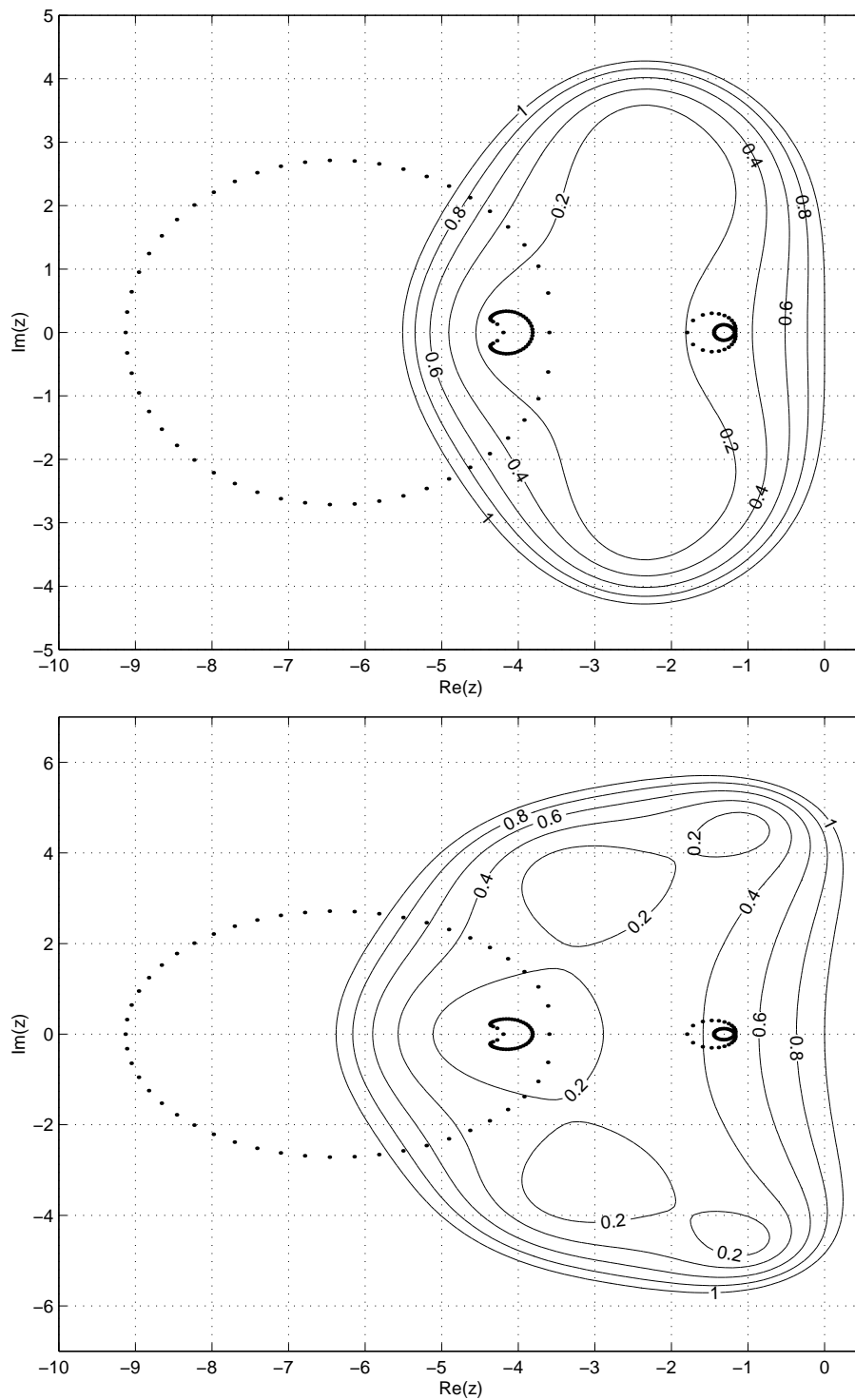


Fig. 7 Locus of the eigenvalues $z_m(\theta)$, $\theta \in [0, 2\pi)$, (dots) of the DG discretization of $u_t + au_x = 0$ and the stability domain of the explicit 5-stage Runge-Kutta method (42) with optimized coefficients (top) and the five stage semi-implicit Jameson Runge-Kutta scheme (bottom). $CFL_{\Delta t} = 1.0$. $CFL_{\Delta \tau} = 1.8$, no grid velocity.

cell faces;

- vorticity sensor, which measures the vorticity within an element;
- grid sensor, which either measures the anisotropy of the mesh or the mesh width of a cell.

We do not control the adaptation procedure using a-posteriori error estimates, since this technique presently is not sufficiently well developed for the Euler equations. After the mesh adaptation the coupling coefficients (22), which link the old and new space-time slabs, have to be computed in order to preserve time accuracy. In the next two sections we will discuss the evaluation of this contribution for element refinement and coarsening.

2.4.1 Space-time slab coupling for element refinement

Given a refinement between two space-time slabs, where an element is divided in half in one of the computational coordinate directions, let \mathcal{K}_j^{n-1} be an element in the space-time slab \mathcal{T}_h^{n-1} , and $\mathcal{K}_{j_0}^n, \mathcal{K}_{j_1}^n$ two space-time elements in \mathcal{T}_h^n such that: $K_j^n := \bar{K}_j(t_n^-) = \bar{K}_{j_0}(t_n^+) \cup \bar{K}_{j_1}(t_n^+)$. The solution $U_h(\bar{x}, t_n^-)$ in element \mathcal{K}_j^{n-1} is approximated as:

$$U_{h,j}(\bar{x}, t_n^-) = \sum_{m=0}^4 \hat{U}_m(\mathcal{K}_j^{n-1}) \psi_{m,j}(\bar{x}, t_n^-),$$

where the element index j is added to U_h and the basis functions ψ_m to indicate to which element they belong. The space-time slab coupling coefficients (22) for the elements $\mathcal{K}_{j_k}^n$, $k = 0$ or 1 , can now be evaluated as:

$$\begin{aligned} B_l(U_h^+|_{\mathcal{K}_{j_k}(t_n^+)}) &= \int_{\mathcal{K}_{j_k}(t_n^+)} U_{h,j}(\bar{x}, t_n^-) \psi_{l,j_k}(\bar{x}, t_n^+) dK \\ &= \sum_{m=0}^3 \hat{U}_m(\mathcal{K}_j^{n-1}) \int_{\mathcal{K}_{j_k}(t_n^+)} \psi_{m,j}(\bar{x}, t_n^-) \psi_{l,j_k}(\bar{x}, t_n^+) dK, \quad l = 0, \dots, 4. \end{aligned} \tag{47}$$

The summation over the DG expansion coefficients is from zero to three, since $\psi_{4,j}(\bar{x}, t_n^-) = 0$ (cf. (5)). The evaluation of the integrals on the right hand side of (47) requires an explicit expression for $\psi_{m,j}(\bar{x}, t_n^-)$ in the element \mathcal{K}_{j_k} . Since the basis functions ψ_m are defined in the reference element $\hat{\mathcal{K}}$ using the basis functions $\hat{\psi}_m$, we must link $\psi_{m,j}(\bar{x}, t_n^-)$ to its representation in the reference element. Introduce the mappings L_i^k , with $1 \leq i \leq 3$, and $k = 0$ or 1 , which are defined as:

$$L_i^k : \hat{\mathcal{K}} \rightarrow \hat{\mathcal{K}}' : \xi_m \mapsto \begin{cases} \frac{1}{2}\xi_m - \frac{1}{2} + k & \text{if } i = m \\ \xi_m & \text{if } i \neq m, \end{cases}$$

with:

$$\hat{\mathcal{K}}^i = (-1, 1) \times \dots \times (-1 + k, k) \times \dots \times (-1, 1).$$

i -th entry

Here the subscript i denotes the coordinate direction in which the element is refined. Note that $G_{K_{j_k}}$ and $G_{K_j} \circ L_i^k$ are identical isoparametric mappings of \mathcal{K}_{j_k} . We can use this property to relate the basis function in the element \mathcal{K}_j to the basis functions in its children \mathcal{K}_{j_0} and \mathcal{K}_{j_1} . The basis functions $\psi_{m,j}$, restricted to K_{j_0} and K_{j_1} in (47), transform to:

$$\psi_{m,j} = \hat{\psi}_m \circ G_{K_j}^{-1} = \hat{\psi}_m \circ L_i^k \circ G_{K_{j_k}}^{-1} = \begin{cases} \frac{1}{2}\psi_{m,j_k} - \frac{1}{2} + k & \text{if } i = m \\ \psi_{m,j_k} & \text{if } i \neq m, \end{cases} \quad (48)$$

and we can use (48) to define the basis functions $\psi_{m,j}$ in the elements K_{j_k} . If we introduce (48) into (47) and transform back to the reference element \hat{K} then we obtain simple expressions for the element integrals which can be evaluated with a product Gauss quadrature rule with three points in each coordinate direction.

2.4.2 Space-time slab coupling for element coarsening

Given a de-refinement between two space-time slabs, let $\mathcal{K}_{j_0}^{n-1}$ and $\mathcal{K}_{j_1}^{n-1}$ be two elements in the space-time slab \mathcal{T}_h^{n-1} , and $\mathcal{K}_j^n \in \mathcal{T}_h^n$, the space-time element such that: $K_j^n := \bar{K}_j(t_n^+) = \bar{K}_{j_0}(t_n^-) \cup \bar{K}_{j_1}(t_n^-)$. The integral for the coupling coefficients (22) then can be evaluated as:

$$\begin{aligned} B_l(U_h^+|_{K(t_n^+)}) &= \int_{K_{j_0}(t_n^-)} U_{h,j_0}(\bar{x}, t_n^-) \psi_{l,j}(\bar{x}, t_n^+) dK + \\ &\quad \int_{K_{j_1}(t_n^-)} U_{h,j_1}(\bar{x}, t_n^-) \psi_{l,j}(\bar{x}, t_n^+) dK \\ &= \sum_{m=0}^3 \left(\hat{U}_m(\mathcal{K}_{j_0}^{n-1}) \int_{K_{j_0}(t_n^-)} \psi_{m,j}(\bar{x}, t_n^-) \psi_{l,j}(\bar{x}, t_n^+) dK + \right. \\ &\quad \left. \hat{U}_m(\mathcal{K}_{j_1}^{n-1}) \int_{K_{j_1}(t_n^-)} \psi_{m,j}(\bar{x}, t_n^-) \psi_{l,j}(\bar{x}, t_n^+) dK \right), \end{aligned} \quad (49)$$

with $\psi_{m,j}$ restricted to \mathcal{K}_{j_0} and \mathcal{K}_{j_1} given by (48). After transformation to the reference element it is straightforward to calculate the integrals in (49) with a product Gauss quadrature rule with three points in each coordinate direction.

2.5 Grid deformation

The grid in the time slabs is constructed using the motion of the boundary, following the procedure proposed by Masud and Hughes (Ref. 33). For a given time level $t = t_n$ let $\partial\Omega(t_n)$ be the



boundary of $\Omega(t_n) \subset \mathbb{R}^3$. Decompose $\partial\Omega(t_n) = \Gamma_m \cup \Gamma_f$ into a moving boundary Γ_m and a fixed boundary Γ_f , with $\Gamma_m \cap \Gamma_f = \emptyset$. The position of Γ_m at time level $t = t_{n+1}$ is prescribed by a displacement function g , which describes the movement of the boundary. The grid is deformed to accommodate the movement of the boundary by solving the following equation for the displacement function $s : \Omega(t_n) \rightarrow \mathbb{R}^3$:

$$\begin{aligned} \nabla \cdot ([1 + \tau_m] \nabla s) &= 0, & x \in \Omega(t_n) \\ s &= g, & x \in \Gamma_m \\ s &= 0, & x \in \Gamma_f, \end{aligned} \tag{50}$$

with $\tau_m : \Omega(t_n) \rightarrow \mathbb{R}^+ \cup \{0\}$ a function designed such that small elements mainly experience solid body motion in order to prevent grid inversion at sharp corners. For the Euler simulations discussed in these notes this term was, however, not necessary to preserve grid consistency. The mesh at time level $t = t_{n+1}$ then is obtained by adding the displacement s to the position of the grid points at time t_n . The system (50) is discretized using a standard (continuous) Galerkin discretization with linear tetrahedron elements. The resulting linear system of equations is solved using a diagonal preconditioned conjugate gradient method.

The grid deformation procedure can deform elements in such a way that the isoparametric mapping F_K^n from the master element \hat{K} is not invertible. In order to detect these elements the conditions derived by Knupp (Ref. 28) and Van der Vegt (Ref. 47) on the invertibility of the isoparametric mapping are used. If elements are detected which do not fulfill this condition then their deformation is limited by increasing the value of τ , but in most practical simulations this has not been necessary.

3 Efficient Flux Quadrature

The computation of the element face and volume flux integrals is by far the most computing intensive part in the space-time discontinuous Galerkin finite element method. The use of Gauss quadrature rules for the evaluation of the flux integrals, as discussed in Section 2.2.4.2, is straightforward but requires a large number of flux evaluations and makes the algorithm unnecessarily expensive. In order to improve the computational efficiency we discuss and analyze in this section an alternative flux quadrature technique. This technique is based on a Taylor series expansion of the flux and uses also information of the flow field gradients, which is readily available in a discontinuous Galerkin discretization.

3.1 Preliminaries

The evaluation of the flux integrals will be performed in a reference element, and to this end the following notation is introduced. Let $d\hat{\mathcal{S}}^m$ (resp. $d\bar{\mathcal{S}}^m$) be the \mathbb{R}^4 valued (resp. \mathbb{R}^3 valued) measure on $\hat{\mathcal{S}} = (-1, 1)^3$ such that:

$$\begin{aligned} \int_{\mathcal{S}_m} f n_{\mathcal{K}} dx &= \int_{\hat{\mathcal{S}}} f d\hat{\mathcal{S}}^m, \\ \int_{\mathcal{S}_m} f \bar{n}_{\mathcal{K}} dx &= \int_{\hat{\mathcal{S}}} f d\bar{\mathcal{S}}^m, \end{aligned}$$

($1 \leq m \leq 6$), where f is a function on $\mathcal{S}_m \subset \partial\mathcal{K}$ and dx is the Euclidean measure on \mathcal{S}_m . The precise expression for the two measures is given in Appendix B. In Appendix B it will be shown that the vector-valued measures $d\hat{\mathcal{S}}^m$ and $d\bar{\mathcal{S}}^m$ satisfy the following relation for $1 \leq m \leq 6$:

$$\int_{\hat{\mathcal{S}}} f \cdot d\hat{\mathcal{S}}^m = \frac{1}{2} \Delta t \left(\int_{\hat{\mathcal{S}}} \bar{f} \cdot d\bar{\mathcal{S}}^m - \int_{\hat{\mathcal{S}}} f_4 v \cdot d\bar{\mathcal{S}}^m \right), \quad (51)$$

for any integrable function $f : \mathcal{S}_m \rightarrow \mathbb{R}^4$, where $v = (F_K^{n+1} - F_K^n) / \Delta t$ is the local grid velocity. Taking $f = W_h^T \mathcal{F}$ we have:

$$\int_{\mathcal{S}_m} W_h^T \mathcal{F} n_{\mathcal{K}} dx = \frac{1}{2} \Delta t \left(\int_{\hat{\mathcal{S}}} W_h^T \bar{\mathcal{F}} \cdot d\bar{\mathcal{S}}^m - \int_{\hat{\mathcal{S}}} W_h^T U v \cdot d\bar{\mathcal{S}}^m \right), \quad (52)$$

in which we recognize the ALE formulation containing the grid velocity. In the remainder of these notes we will drop the subscript \mathcal{K} from the space-time normal n .

For the analysis of the local truncation error Section 3.3.4 it is beneficial to rewrite the weak formulation (15) by introducing the space-time numerical flux H_{SP} as:

$$H_{\text{SP}}(U_h^-, U_h^+, n_{\mathcal{K}}) = \begin{cases} H(U_h^-, U_h^+, \bar{n}_{\mathcal{K}}) & \text{if } \bar{n}_{\mathcal{K}} \neq 0, \\ \frac{1}{2}(U_h^- + U_h^+) n_{\mathcal{K},4} - \frac{1}{2} |n_{\mathcal{K},4}| (U_h^+ - U_h^-) & \text{if } \bar{n}_{\mathcal{K}} = 0, \end{cases}$$

The weak formulation (15) then is equal to:

$$\sum_{j=1}^{N_n} \left\{ - \int_{\mathcal{K}_j^n} (\text{grad } W_h)^T : \mathcal{F}(U_h) d\mathcal{K} + \int_{\partial\mathcal{K}_j^n} W_h^- \cdot H_{\text{SP}}(U_h^-, U_h^+, n_{\mathcal{K}}) d(\partial\mathcal{K}) + \right. \quad (53)$$

$$\left. \int_{\mathcal{K}_j^n} ((\text{grad } W_h)^T \cdot \mathfrak{D}(U_h)) : \text{grad } U_h d\mathcal{K} \right\} = 0. \quad (54)$$

3.2 Taylor quadrature rule

In an attempt to improve the computational efficiency of the second order accurate DG method a novel approximation of the flux integrals is proposed. The flux function in the integrand is replaced by the second order Taylor series of the flux evaluated at the face center. Terms containing the gradients transversal to the face are introduced into the discretized equations, enhancing the stability of the discretized system. Moreover, second order accuracy of this Taylor approximation of the flux integrals is proved in Section 3.3.4. Based on a flop count analysis (not presented here) it is estimated that this approximation is computationally more efficient than Gauss quadrature, because of the reduction in the number of flux evaluations. Also, the locality of the required flow data (only data in the face center is required) will improve the speed of the flux quadrature algorithm.

First, we will explain the basic concept of the so-called Taylor quadrature for the face flux integrals, after which we will present the general formulation for both face and volume flux integrals. In the Taylor quadrature rule, the central part of the HLLC flux, namely the contribution $\frac{1}{2}(\hat{\mathcal{F}}(U_L) + \hat{\mathcal{F}}(U_R))$ in (32), is approximated as:

$$\begin{aligned} \int_{\mathcal{S}_m} \phi_m \bar{\mathcal{F}}_{ik}(U_*) \bar{n}_k dx &\approx \bar{\mathcal{F}}_{ik}(U_*(\bar{\xi}_m)) \int_{\hat{\mathcal{S}}} \xi_m d\bar{\mathcal{S}}_k^m \\ &+ \sum_{l \in I(\mathcal{S}_m)} \frac{\partial \bar{\mathcal{F}}_{ik}}{\partial U_*^j}(U_*(\bar{\xi}_m)) \frac{\partial U_*^j}{\partial \xi_l}(\bar{\xi}_m) \int_{\hat{\mathcal{S}}} \xi_l \xi_m d\bar{\mathcal{S}}_k^m, \end{aligned} \quad (55)$$

where $U_* = U_L$ or U_R , $\bar{\xi}_m$ is the computational face center of the face \mathcal{S}_m defined by $\bar{\xi}_{m,i} = \pm \delta_{im}$, and $I(\mathcal{S}_m)$ is the ordered index set defined by $I(\mathcal{S}_m) = \{m_2, m_3, m_4\}$, $m_2 < m_3 < m_4$, the complement of $\{m\}$ in $\{1, 2, 3, 4\}$. These are the first four terms in a Taylor expansion of the integrand on $\hat{\mathcal{S}}$. The remaining integrals, which depend solely on the geometry of the face, are evaluated exactly — only the flux terms are expanded in a Taylor series. The exact evaluation of the geometric terms is crucial in order to maintain the second order accuracy of the DG method.

The flow derivatives necessary for the quadrature rule can be easily computed, since in computational coordinates the solution vector U_h in cell \mathcal{K} , restricted to the face \mathcal{S}_{m_1} , can be written as:

$$U|_{\mathcal{S}_{m_1}} = U(\bar{\xi}_{m_1}) + \xi_{m_2} \hat{U}_{m_2}(\mathcal{K}) + \xi_{m_3} \hat{U}_{m_3}(\mathcal{K}) + \xi_4 \hat{U}_4(\mathcal{K}); \quad (56)$$

hence, the flow derivatives are equal to $\frac{\partial U}{\partial \xi_l}(\bar{\xi}_{m_1}) = \hat{U}_l$ for $l \in I(\mathcal{S}_{m_1})$. The fact that the gradients occur directly in the approximation of the face flux integrals, demonstrates that DG methods provide a natural setting for the Taylor quadrature rule.

For the general formulation of the Taylor quadrature rule for both face and volume flux integrals we return to the weak formulation (54) of the Euler equations using the space-time flux. This allows us to treat the space-time fluxes through the different element faces in a uniform way.

The first step is to transform the integrals in physical space to integrals in computational space,

$$\int_{\mathcal{Q}} W_h^- \cdot \mathcal{F}^\pm n^T d\mathcal{Q} = \sum_{m=1}^8 \int_{\hat{\mathcal{S}}_m} \hat{W}_{h,i}^- \cdot \mathcal{F}_{ik}^\pm d\hat{\mathcal{S}}_k^m. \quad (57)$$

Likewise the volume flux integrals are transformed to computational space:

$$\int_{\mathcal{K}} \nabla W_h : \mathcal{F} d\mathcal{K} = \int_{\hat{\mathcal{K}}} \nabla \hat{W}_h : \mathcal{F} |J_{G_K}| d\hat{\mathcal{K}}. \quad (58)$$

Subsequently the flux in the integrand is expanded in a second order Taylor series, and the following Taylor quadrature rules for the face and volume integrals are obtained:

$$\int_{\partial\mathcal{K}} W_h^- \cdot \mathcal{F}^\pm \cdot n_{\mathcal{K}} d\partial\mathcal{K} \approx \sum_{m=1}^8 [\mathcal{F}_{ik}^\pm(\bar{\xi}_m) \int_{\hat{\mathcal{S}}} \hat{W}_{h,i}^- d\hat{\mathcal{S}}_k^m + \sum_{l \in I(\mathcal{S}_m)} \frac{\partial \mathcal{F}_{ik}^\pm(\bar{\xi}_m)}{\partial \xi_l} \int_{\hat{\mathcal{S}}} \hat{W}_{h,i}^- \xi_l d\hat{\mathcal{S}}_k^m], \quad (59)$$

$$\int_{\mathcal{K}} \nabla W_h : \mathcal{F} d\mathcal{K} \approx \mathcal{F}_{ij}(0) \int_{\hat{\mathcal{K}}} \frac{\partial W_{h,i}}{\partial x_j} |J_{G_K}| d\hat{\mathcal{K}} + \frac{\partial \mathcal{F}_{ij}(0)}{\partial \xi_l} \int_{\hat{\mathcal{K}}} \frac{\partial W_{h,i}}{\partial x_j} \xi_l |J_{G_K}| d\hat{\mathcal{K}}, \quad (60)$$

with $\mathcal{F}^\pm = \mathcal{F}(U^\pm)$.

In Section 3.3.5, Lemma 3.3.3, the conditions for the flux tensor will be given such that the approximations above are well defined.

3.3 Taylor approximation

For the stability of the discretization, it was found to be essential to not just expand the central part of the numerical flux, but also the dissipative part. This has been one of the main reasons to apply the HLLC flux, where one can hope to obtain reasonably simple expressions for the derivatives of the dissipative part. Note that in smooth parts of the flow field the dissipative part of the numerical flux is of higher order than the central part, hence the approximation of the face integrals of the dissipative part does not affect the local truncation error analyzed in Section 3.3.4. This section only deals with the numerical flux through the space-time faces. The time-numerical flux, including the dissipative part of the time-numerical flux, is computed analytically, which is consistent with the Taylor quadrature rule, since the time-flux is linear.

The application of the Taylor quadrature rule to the HLLC flux can be most easily accomplished by rewriting the intermediate states (34) as:

$$\begin{aligned} U_L^* &= \frac{S_L - \hat{u}_L}{S_L - S_M} U_L + \frac{1}{S_L - S_M} \begin{pmatrix} 0 \\ (p^* - p_L)\bar{n} \\ p^* S_M - p_L \hat{u}_L \end{pmatrix} \\ &= \frac{S_L}{S_L - S_M} U_L - \frac{1}{S_L - S_M} \left[\hat{u}_L U_L + p_L \begin{pmatrix} 0 \\ \bar{n} \\ \hat{u}_L \end{pmatrix} \right] + \frac{1}{S_L - S_M} p^* \begin{pmatrix} 0 \\ \bar{n} \\ S_M \end{pmatrix} \end{aligned}$$

(right intermediate state is computed likewise). Recognizing the second term between square brackets on the right hand side as a flux term, the HLLC flux can be expressed as:

$$\begin{aligned} H_{\text{HLLC}}(U_L, U_R, n) &= c_L \hat{\mathcal{F}}_L + c_R \hat{\mathcal{F}}_R - \frac{1}{2} v (U_L + U_R) \\ &+ \frac{1}{2} \left(|\tilde{S}_L| - S_L \frac{|\tilde{S}_L| - |\tilde{S}_M|}{S_L - S_M} \right) U_L - \frac{1}{2} \left(|\tilde{S}_R| - S_R \frac{|\tilde{S}_R| - |\tilde{S}_M|}{S_R - S_M} \right) U_R \\ &- \frac{1}{2} \left(\frac{|\tilde{S}_L| - |\tilde{S}_M|}{S_L - S_M} - \frac{|\tilde{S}_R| - |\tilde{S}_M|}{S_R - S_M} \right) p^* v_p, \end{aligned} \quad (61)$$

where $\hat{\mathcal{F}}_L = \hat{\mathcal{F}}(U_L) = \bar{\mathcal{F}}(U_L) \cdot \bar{n}$ is the normal flux. The corrected wave speeds are defined as $\tilde{S}_* = S_* - v$, the constants c_L and c_R are given by the relations:

$$\begin{aligned} c_L &= \frac{1}{2} \left(1 + \frac{|\tilde{S}_L| - |\tilde{S}_M|}{S_L - S_M} \right), \\ c_R &= \frac{1}{2} \left(1 - \frac{|\tilde{S}_R| - |\tilde{S}_M|}{S_R - S_M} \right), \end{aligned}$$

and the vector $v_p \in \mathbb{R}^5$ is defined by:

$$v_p = \begin{pmatrix} 0 \\ \bar{n} \\ S_M \end{pmatrix}.$$

The term $\frac{1}{2}(\hat{\mathcal{F}}(U_L) + \hat{\mathcal{F}}(U_R))$ in (61) is referred to as the central part of the numerical flux, the remaining terms as the dissipative part of the numerical flux.

A complete linearization of the HLLC flux would require the linearization of all wave speeds. Linearization of the wave speeds is a tedious exercise, not only because the expressions for the left and right wave speeds are complex, but also because of the upwind character of the HLLC flux. An efficient linearization of the flux integral would be a linearization where the left and right wave speeds are assumed to be constant, while retaining certain desirable properties of the HLLC flux. These properties are stability of the discretization scheme, preservation of uniform flow, and the contact wave analogy for the contact wave speed. Such a linearization is presented below, for a given space-time face $\mathcal{S} = \mathcal{S}_m$, ($1 \leq m \leq 6$), using the following assumptions:

Assumption 1 *The wave speeds S_L and S_R are assumed constant in the face, the contact wave speed S_M is allowed to vary with the flow. Variations with respect to the face normal are ignored for all wave speeds.*

Assumption 2 *The wave speeds are computed based on the face average normal $\int_{\mathcal{S}} \bar{n} dx / |\int_{\mathcal{S}} \bar{n} dx|$.*

Assumption 3 *The face moments are approximated as $\int_{\hat{\mathcal{S}}} P J_{\mathcal{S}} d\xi \approx |\int_{\hat{\mathcal{S}}} P d\bar{\mathcal{S}}|$, for an arbitrary polynomial P on $\hat{\mathcal{S}}$, where $J_{\mathcal{S}}$ is the Jacobian of the parameterization of \mathcal{S} .*

Assumption 4 *The coefficients in the dissipative flux containing the contact wave speed are assumed constant.*

As will be shown in Section 3.3.1, the first assumption is sufficient to ensure that the intermediate pressures are equal across the contact wave up to second order in the left and right states. In Section 3.3.2 it will be shown that the other assumptions are sufficient to ensure the preservation of uniform flow when the Taylor quadrature rule is used. The stability of the scheme will be demonstrated experimentally in Section 4. It is important to note that the Taylor quadrature rule puts no restriction on the specific choice of the left and right wave speeds.

Using Assumption 1 to 4 and the formulation of the HLLC flux in (61) we obtain the following approximation of the face flux integrals:

$$\int_{\mathcal{S}_m} \phi_n H_{\text{HLLC}}^i(U_L, U_R, \bar{n}) dx \approx \tag{62}$$

$$\begin{aligned}
& \frac{1}{2} (c_L \bar{\mathcal{F}}_{ik}(U_L(\bar{\xi}_m)) + c_R \bar{\mathcal{F}}_{ik}(U_R(\bar{\xi}_m))) \int_{\hat{S}} \xi_n d\bar{\mathcal{S}}_k^m \\
& + \frac{1}{2} c_L \sum_{l \in I(S)} \frac{\partial \bar{\mathcal{F}}_{ik}}{\partial U^j}(U_L(\bar{\xi}_m)) \hat{U}_{L,l}^j \int_{\hat{S}} \xi_l \xi_n d\bar{\mathcal{S}}_k^m \\
& + \frac{1}{2} c_R \sum_{l \in I(S)} \frac{\partial \bar{\mathcal{F}}_{ik}}{\partial U^j}(U_R(\bar{\xi}_m)) \hat{U}_{R,l}^j \int_{\hat{S}} \xi_l \xi_n d\bar{\mathcal{S}}_k^m \\
& - \frac{1}{2} \int_{\hat{S}} (U_L + U_R) \xi_n v_k d\bar{\mathcal{S}}_k^m \\
& + \frac{1}{2} \left(|\tilde{S}_L| - S_L \frac{|\tilde{S}_L| - |\tilde{S}_M|}{S_L - S_M} \right) \int_{\hat{S}} U_L^i \xi_n J_{S_m} d\xi \tag{63}
\end{aligned}$$

$$\begin{aligned}
& - \frac{1}{2} \left(|\tilde{S}_R| - S_R \frac{|\tilde{S}_R| - |\tilde{S}_M|}{S_R - S_M} \right) \int_{\hat{S}} U_R^i \xi_n J_{S_m} d\xi \tag{64} \\
& - \frac{1}{2} \left(\frac{|\tilde{S}_L| - |\tilde{S}_M|}{S_L - S_M} - \frac{|\tilde{S}_R| - |\tilde{S}_M|}{S_R - S_M} \right) \tilde{F}^i(p^*).
\end{aligned}$$

The first three terms on the right hand side of (62) follow directly from (55). In the last term the functions $\tilde{F}^i(p^*)$ are defined as:

$$\begin{aligned}
\tilde{F}^1(p^*) &= 0 \\
\tilde{F}^i(p^*) &= p^*(\bar{\xi}_m) \int_{\hat{S}} \xi_n d\bar{\mathcal{S}}_{i-1}^m + \tag{2 \leq i \leq 4} \\
& + \sum_{l \in I(S)} \left(\frac{\partial p^*}{\partial U_L^j} \hat{U}_{L,l}^j + \frac{\partial p^*}{\partial U_R^j} \hat{U}_{R,l}^j \right) \int_{\hat{S}} \xi_l \xi_n d\bar{\mathcal{S}}_{i-1}^m \\
\tilde{F}^5(p^*) &= S_M(\bar{\xi}_m) p^*(\bar{\xi}_m) \int_{\hat{S}} \xi_n J_{S_m} d\xi + \\
& + \sum_{l \in I(S)} S_M(\bar{\xi}_m) \left(\frac{\partial p^*}{\partial U_L^j} \hat{U}_{L,l}^j + \frac{\partial p^*}{\partial U_R^j} \hat{U}_{R,l}^j \right) \int_{\hat{S}} \xi_l \xi_n J_{S_m} d\xi \\
& + \sum_{l \in I(S)} p^*(\bar{\xi}_m) \left(\frac{\partial S_M}{\partial U_L^j} \hat{U}_{L,l}^j + \frac{\partial S_M}{\partial U_R^j} \hat{U}_{R,l}^j \right) \int_{\hat{S}} \xi_l \xi_n J_{S_m} d\xi,
\end{aligned}$$

which essentially is the differentiation product rule applied to $p^* v_p$ in (61). The integrals in (63) and (64) are written out using (56) and Assumption 3 for the face moments:

$$\begin{aligned}
\int_{S_m} U \xi_n J_{S_m} d\xi &= U(\bar{\xi}_m) \int_{\hat{S}} \xi_n J_{S_m} d\xi + \sum_{l \in I(S)} \hat{U}_l \int_{\hat{S}} \xi_l \xi_n J_{S_m} d\xi \\
&\approx U(\bar{\xi}_m) \left| \int_{\hat{S}} \xi_n d\bar{\mathcal{S}}^m \right| + \sum_{l \in I(S)} \hat{U}_l \left| \int_{\hat{S}} \xi_l \xi_n d\bar{\mathcal{S}}^m \right|.
\end{aligned}$$

The grid velocity term is treated in the same way:

$$\int_{\hat{S}} U \xi_n v \cdot \bar{n} J_S d\xi = U(\bar{\xi}_m) \int_{\hat{S}} \xi_n v \cdot d\bar{S}^m + \sum_{l \in I(S)} \hat{U}_l \int_{\hat{S}} \xi_l \xi_n v \cdot d\bar{S}^m$$

(note that this is not an approximation). The analytical expressions for the geometric integrals $\int_{\hat{S}} \xi_l \xi_n d\bar{S}^m$ and $\int_{\hat{S}} \xi_l \xi_n v \cdot d\bar{S}^m$ are presented in Appendix C.

3.3.1 Contact wave analogy

The intermediate pressures defined in (35) are equal if all flow quantities are evaluated at the same point. If we assume all wave speeds to be constant in a face, we would have $\frac{\partial p_R^*}{\partial U_L} = 0$, whereas clearly $\frac{\partial p_L^*}{\partial U_L}$ is nonzero. Hence a variation in the left state would have no effect on the right intermediate pressure, so the intermediate pressures will in general not be equal across the face. Since the introduction of the contact wave analogy into the HLL flux has significantly improved the accuracy of the HLLC flux, we want to preserve the contact wave analogy within the quadrature rule. We will show that taking the variation of S_M into account, but assuming S_L and S_R constant across the face, implies that the left and right intermediate pressures are equal up to second order (compare with Batten et al. (Ref. 6)), which is consistent with the Taylor quadrature rule.

Lemma 3.3.1 *Given Assumption 1, we have:*

$$(p_L^* - p_R^*)(U_L + \Delta U_L, U_R + \Delta U_R) = \mathcal{O}(|\Delta U_L|^2, |\Delta U_R|^2), \quad (|\Delta U_L|, |\Delta U_R| \rightarrow 0).$$

Since the intermediate pressures are equal in the face center by the construction of the contact wave speed S_M , it is sufficient to prove that the linear variations of the intermediate pressures are equal.

Define $\tilde{\rho} = \rho_R(S_R - \hat{u}_R) - \rho_L(S_L - \hat{u}_L)$. Given the definition of S_M in (33) the derivative of S_M with respect to the left state is obtained as follows:

$$\begin{aligned} \frac{\partial S_M}{\partial U_L} &= -\frac{S_M}{\tilde{\rho}} \frac{\partial \tilde{\rho}}{\partial U_L} + \frac{1}{\tilde{\rho}} \frac{\partial}{\partial U_L} (-\rho_L \hat{u}_L (S_L - \hat{u}_L) + p_L) \\ &= -\frac{S_M}{\tilde{\rho}} \frac{\partial \tilde{\rho}}{\partial U_L} + \frac{1}{\tilde{\rho}} \frac{\partial}{\partial U_L} (p_L^* - \rho_L S_M (S_L - \hat{u}_L)) \\ &= -\frac{S_M}{\tilde{\rho}} \frac{\partial \tilde{\rho}}{\partial U_L} + \frac{1}{\tilde{\rho}} \frac{\partial p_L^*}{\partial U_L} - \frac{\rho_L (S_L - \hat{u}_L)}{\tilde{\rho}} \frac{\partial S_M}{\partial U_L} + \frac{S_M}{\tilde{\rho}} \frac{\partial \tilde{\rho}}{\partial U_L} \\ &= \frac{1}{\tilde{\rho}} \frac{\partial p_L^*}{\partial U_L} - \frac{\rho_L (S_L - \hat{u}_L)}{\tilde{\rho}} \frac{\partial S_M}{\partial U_L} \end{aligned}$$

which is equivalent with:

$$\rho_R (S_R - \hat{u}_R) \frac{\partial S_M}{\partial U_L} = \frac{\partial p_L^*}{\partial U_L}.$$

Hence,

$$\frac{\partial p_R^*}{\partial U_L} = \rho_R(S_R - \hat{u}_R) \frac{\partial S_M}{\partial U_L} = \frac{\partial p_L^*}{\partial U_L},$$

where the first equality follows directly from (35). Likewise it can be proven that the derivatives with respect to U_R are equal. \square

3.3.2 Consistency of the approximation

Lemma 3.3.2 *Given Assumption 2 to 4, the Taylor approximation of the flux integrals preserves uniform flow. Hence the flux evaluation satisfies the Geometric Conservation Law for moving meshes.*

To prove the preservation of uniform flow, it is sufficient to show that the dissipative part of the HLLC scheme vanishes in uniform flow, since the geometric terms in the central flux are evaluated exactly.

Without loss of generality we may assume $S_L < v < S_M < S_R$. The dissipative part of the HLLC scheme is given pointwise by (compare with (61))

$$\frac{\tilde{S}_L}{S_L - S_M} \left(S_M U + p v_p - \hat{\mathcal{F}} \right),$$

where the subscripts R and L are omitted from the flow variables since $U_L = U_R = U$. For uniform flow, the contact wave speed S_M is equal to the normal velocity. With the definition of the normal in the definition of the wave speeds, Assumption 2, we have:

$$S_M = \frac{u \cdot \int_{\mathcal{S}} \bar{n} dx}{\left| \int_{\mathcal{S}} \bar{n} dx \right|},$$

hence,

$$u \cdot \int_{\mathcal{S}} \bar{n} dx = S_M \left| \int_{\mathcal{S}} \bar{n} dx \right| \stackrel{\text{Ass. 3}}{=} S_M \int_{\mathcal{S}} dx.$$

If we now use Assumption 4 in the first equality, we obtain:

$$\begin{aligned} \int_{\mathcal{S}} \frac{\tilde{S}_L}{S_L - S_M} \left(S_M U + p v_p - \hat{\mathcal{F}} \right) dx &= \\ &= \frac{\tilde{S}_L}{S_L - S_M} \int_{\mathcal{S}} \left(S_M U + p v_p - \hat{\mathcal{F}} \right) dx \\ &= \frac{\tilde{S}_L}{S_L - S_M} \left(U u \cdot \int_{\mathcal{S}} \bar{n} dx + \int_{\mathcal{S}} p v_p dx - \bar{\mathcal{F}} \cdot \int_{\mathcal{S}} \bar{n} dx \right) \\ &= \frac{\tilde{S}_L}{S_L - S_M} \left(\begin{array}{c} \rho u \cdot \int_{\mathcal{S}} \bar{n} dx \\ (\rho u + p) \int_{\mathcal{S}} \bar{n} dx \\ (\rho E + p) u \cdot \int_{\mathcal{S}} \bar{n} dx \end{array} \right) - \bar{\mathcal{F}} \cdot \int_{\mathcal{S}} \bar{n} dx = 0, \end{aligned}$$

hence, uniform flow is preserved. Combined with the exact evaluation of the geometrical coefficients this proves that the Taylor quadrature rule satisfies the Geometric Conservation Law. \square

3.3.3 Boundary conditions

The Taylor quadrature rule described above is extended to boundary faces by consistently expanding the boundary conditions in Taylor series. Since the flux for a boundary face is computed using a right state based on the left state, the expansion only depends on the left state. To be more precise, for a specific boundary condition let $f : \mathbb{R}^5 \rightarrow \mathbb{R}^5$ define the mapping describing the dummy state as function of the left state:

$$U_R = f_w(U_L) =: \mathcal{B}(U_L, U_w),$$

then

$$\begin{aligned} \frac{\partial}{\partial \xi_l} \bar{\mathcal{F}}(U_R) &= \frac{\partial}{\partial \xi_l} \bar{\mathcal{F}}(f_w(U_L)) \\ &= \frac{\partial \bar{\mathcal{F}}}{\partial U^k}(U_R) \frac{\partial f_w^k}{\partial U^j} \hat{U}_{L,l}^j. \end{aligned}$$

It is natural to approximate the integrals of the dissipative flux using the Taylor expansion of f :

$$\int_{\mathcal{S}} U_R^i \phi_n dx \approx U_R^i(\bar{\xi}_m) \int_{\mathcal{S}} \xi_n J_S d\xi + \sum_{l \in I(\mathcal{S})} \frac{\partial f_w^i}{\partial U^j} \hat{U}_{L,l}^j \int_{\mathcal{S}} \xi_l \xi_n J_S d\xi$$

The above two formulas show that the Taylor quadrature rule for boundary faces is equal to the Taylor quadrature rule for internal faces if we define:

$$\hat{U}_{R,l}^i = \frac{\partial f_w^i}{\partial U^j} \hat{U}_{L,l}^j. \quad (65)$$

It is straightforward to expand the boundary conditions into a Taylor series. For the slip wall boundary condition for strongly curved surfaces it may be beneficial to incorporate the variation of the face normal and grid velocity.

An unexpected benefit of using the Taylor quadrature rule at slip flow boundaries is that it results in considerably smaller entropy and total pressure losses near the slip flow boundary. This will be demonstrated in Section 4.3.2 and more details can be found in Van der Vegt and Van der Ven (Ref. 46).

3.3.4 Local truncation error

In this section we will analyze the accuracy of the Taylor and Gauss quadrature rules for the flux integration. The Gauss quadrature rules are straightforward to implement but computationally expensive in comparison with the Taylor quadrature rules. The main result, Proposition 3.3.12, provides an estimate for the truncation error of the space-time discontinuous Galerkin discretization, including the effect of the Taylor quadrature rules. The analysis shows that the Taylor quadrature rules result in the same truncation error for the space-time DG discretization of the conservation laws, when linear test and trial functions in the reference element are used, as is obtained with Gauss quadrature rules. Both quadrature rules result in a second order truncation error of the discretization in the same properly chosen norm. Also, conditions on the flux tensor \mathcal{F} , and implicitly also on U , are given which guarantee the applicability of the Taylor and Gauss quadrature rules. These conditions and the error estimates require a high degree of smoothness. The required smoothness is, however, not available when discontinuities are present in the flow, but in these areas the numerical discretization will have a reduced accuracy anyway, independent of the quadrature rule. Definitions of the various Sobolev spaces and (semi)-norms used in this section can be found in Appendix A.

3.3.5 Validity of the approximation

Sufficient conditions on the flux tensor such that the Taylor quadrature rules (59) and (60) are applicable are given by the following lemma:

Lemma 3.3.3 *Let $G_K : \hat{\mathcal{K}} \rightarrow \mathcal{K}$ be a C^1 diffeomorphism for all $\mathcal{K} \in \mathcal{T}_h^n$. If $\mathcal{F} \in (W_B^{s,q}(\mathcal{T}_h^n))^{5 \times 4}$, with $s, q \in \mathbb{R}$, $1 \leq q < \infty$, s integer when $q = 1$, and $(s - 1)q > 4$, then the Taylor quadrature rules presented in (59) and (60) are well defined.*

The proof of this lemma is immediate using a Taylor series expansion of the traces \mathcal{F}^\pm and the flux tensor \mathcal{F} , if we can ensure that we can consider pointwise values of \mathcal{F}^\pm at $\partial\hat{\mathcal{K}}$ and \mathcal{F} in $\hat{\mathcal{K}}$, and also for their derivatives. This requires that we can imbed the flux tensor \mathcal{F} in $C^1(\bar{\hat{\mathcal{K}}})$, the space of continuously differentiable functions on $\bar{\hat{\mathcal{K}}}$, the closure of $\hat{\mathcal{K}}$. Since $\hat{\mathcal{K}}$ is a bounded domain with the cone property (see Appendix A) and $(s - 1)q > \dim(\hat{\mathcal{K}}) = 4$, with $s \in \mathbb{R}$ and $1 \leq q < \infty$, s integer when $q = 1$, the following imbedding exists:

$$W^{s,q}(\hat{\mathcal{K}}) \hookrightarrow C^1(\bar{\hat{\mathcal{K}}}). \quad (66)$$

For integer values of s this is part of the Rellich-Kondrachov theorem, see Adams (Ref. 1) Theorem 6.2 part II, page 144. For fractional order spaces, with s not an integer and $1 < q < \infty$, this is a direct consequence of Theorem 4.6.1/6 in Triebel (Ref. 42), pages 327–328, using the relation

between fractional order Sobolev spaces and Besov spaces, see Triebel (Ref. 42), page 323 and also Nikol'skii (Ref. 35). This means that pointwise values of \mathcal{F} and its derivatives exist and the quadrature rules (59)-(60) are well defined, because the Jacobian J_{G_K} is finite when G_K is a C^1 diffeomorphism. \square

Remark 3.3.4 *For the error estimates in Section 3.3.6 we must know to which Sobolev space the traces \mathcal{F}^\pm belong. The imbedding theorem (66) ensures that $\mathcal{F}^\pm \in C^1(\hat{\mathcal{S}}_m)$, but we can also apply the imbedding theorem directly to $\hat{\mathcal{S}}_m$. If we compare the imbedding conditions $(s-1)q > 4$ for \mathcal{F} in the domain $\hat{\mathcal{K}}$ and the equivalent condition $(s'-1)q > 3$ for the imbedding of \mathcal{F}^\pm in $\hat{\mathcal{S}}_m$, then we see that $\mathcal{F}^\pm \in W^{s-1/q,q}(\hat{\mathcal{S}}_m)$. This result can also be obtained from the trace theorem when $s-1/q$ is not an integer, see Grisvard (Ref. 23). In the present analysis also integer values $s-1/q$ are required and we need to use (66) to determine the Sobolev spaces for \mathcal{F}^\pm .*

3.3.6 Analysis of element face quadrature errors

Combining (57) and (59) we can now define the quadrature error functional $E_{\partial\mathcal{K}}$ for the integration of the element face fluxes at $\partial\mathcal{K}$ as:

$$E_{\partial\mathcal{K}}(W_h^-, \mathcal{F}^\pm) = \sum_{m=1}^8 \int_{\hat{\mathcal{S}}_m} \hat{W}_{h,i}^-(\xi) \left(\mathcal{F}_{ik}^\pm(\xi) - \mathcal{F}_{ik}^\pm(\bar{\xi}_m) - \sum_{l \in I(\mathcal{S}_m)} \xi_l \frac{\partial \mathcal{F}_{ik}^\pm(\bar{\xi}_m)}{\partial \xi_l} \right) d\hat{\mathcal{S}}_m^m. \quad (67)$$

An upper bound for the quadrature error of the flux integrals over $\partial\mathcal{K}$ is provided by the following lemma:

Lemma 3.3.5 *Let the tessellation \mathcal{T}_h^n satisfy the condition $0 < h_{\mathcal{T}} \leq 1$, with $h_{\mathcal{T}}$ the diameter of the smallest ball containing the elements $\mathcal{K} \in \mathcal{T}_h^n$. Suppose that for all $\mathcal{K} \in \mathcal{T}_h^n$ the mapping G_K is a C^1 diffeomorphism with $|J_{G_K^{-1}}| \leq C/h_{\mathcal{K}}^4$. Let $\mathcal{F} \in (W_B^{s,q}(\mathcal{T}_h^n))^{5 \times 4}$, with $s, q \in \mathbb{R}$, $1 \leq q < \infty$, s integer when $q = 1$, $(s-1)q > 4$, $(s-2)q \geq 1$, and $W_h \in V_h^1(\mathcal{T}_h^n)$, then the quadrature error $|E_{\partial\mathcal{K}}|$ can be estimated for all $\mathcal{K} \in \mathcal{T}_h^n$ as:*

$$|E_{\partial\mathcal{K}}(W_h^-, \mathcal{F}^\pm)| \leq Ch_{\mathcal{T}}^{2-1/p} |\mathcal{F}^\pm|_{2,q,\partial\mathcal{K}} \|W_h\|_{1,p,\mathcal{K}},$$

with $\frac{1}{p} + \frac{1}{q} = 1$, and C a positive constant independent of $h_{\mathcal{T}}$, \mathcal{F}^\pm and W_h , but dependent on the grid velocity.

Remark 3.3.6 *The bound on the inverse of the Jacobian of G_K^{-1} stated in Lemma 3.3.5 is trivial for a square hexahedral space-time element and also valid for mappings close to the identity. Geometric conditions to ensure this condition for general elements are discussed in van der Vegt (Ref. 47).*



Using the triangle inequality in (67) we obtain the following estimate:

$$\begin{aligned} |E_{\partial\mathcal{K}}(W_h^-, \mathcal{F}^\pm)| &\leq \sum_{m=1}^8 \int_{\hat{\mathcal{S}}_m} |\hat{W}_{h,i}^-(\xi)| |\mathcal{F}_{ik}^\pm(\xi) - \mathcal{F}_{ik}^\pm(\bar{\xi}_m) - \sum_{l \in I(\mathcal{S}_m)} \xi_l \frac{\partial \mathcal{F}_{ik}^\pm(\bar{\xi}_m)}{\partial \xi_l}| |d\hat{\mathcal{S}}_k^m| \\ &\leq Ch_{\mathcal{T}}^3 \|\hat{W}_h^-\|_{0,\infty,\hat{\mathcal{S}}} \|\mathcal{F}^\pm\|_{1,\infty,\hat{\mathcal{S}}}, \end{aligned}$$

where we used in the second step the estimate $|\xi| \leq \sqrt{3}$ for $\xi \in \hat{\mathcal{S}}_m$, and

$$\begin{aligned} \int_{\hat{\mathcal{S}}_m} |d\hat{\mathcal{S}}^m| &\leq \frac{1}{2} \Delta t \left(\int_{\hat{\mathcal{S}}_m} |d\bar{\mathcal{S}}^m| + \int_{\hat{\mathcal{S}}_m} |v \cdot d\bar{\mathcal{S}}^m| \right) \\ &\leq C \Delta t h_{\mathcal{T}}^2 \leq Ch_{\mathcal{T}}^3, \quad \text{for } m = 1, \dots, 6, \end{aligned}$$

which can be obtained directly from the geometric integrals discussed in Appendix C. The estimates for the integrals over \mathcal{S}_7 and \mathcal{S}_8 follow directly from Appendix C. The constant C depends on the grid velocity v . We also used the fact that $\mathcal{F}^\pm \in W^{1,\infty}(\hat{\mathcal{S}})$. This is a direct consequence of the imbedding (66), which is applicable since $(s-1)q > 4$ and the relation $C^1(\tilde{\mathcal{K}}) \hookrightarrow W^{1,\infty}(\tilde{\mathcal{K}})$. This implies, as discussed in Remark 3.3.4, that $\mathcal{F}^\pm \in W^{s-1/q,q}(\hat{\mathcal{S}}) \hookrightarrow W^{1,\infty}(\hat{\mathcal{S}})$ and we obtain the estimate:

$$|E_{\partial\mathcal{K}}(W_h^-, \mathcal{F}^\pm)| \leq Ch_{\mathcal{T}}^3 \|\hat{W}_h^-\|_{0,\infty,\hat{\mathcal{S}}} \|\mathcal{F}^\pm\|_{s-1/q,q,\hat{\mathcal{S}}}.$$

We can further improve the estimate for $|E_{\partial\mathcal{K}}|$ using the generalized Bramble-Hilbert lemma, see Bramble and Hilbert (Ref. 10).

First assume that $s - 1/q = 2$. Define the set of polynomials Q_k , such that $\frac{\partial^{k+1} q}{\partial \xi_j^{k+1}} = 0$ for $j = 1, \dots, 4$. For any fixed $W_h(x) = \hat{W}_h(F_{\mathcal{S}}(\xi)) \in (W^{m,q}(\hat{\mathcal{S}}))^5$, with $m \geq 0$, integer, the bounded linear functional $E_{\partial\mathcal{K}}$ satisfies the relation:

$$E_{\partial\mathcal{K}}(W_h^-, \mathcal{F}^\pm) = 0, \quad \forall \mathcal{F}^\pm \in (Q_1(\hat{\mathcal{S}}))^{5 \times 4}.$$

The Bramble-Hilbert lemma (Ref. 10) then states that there is a positive constant $C(\hat{\mathcal{S}})$, such that for all $\mathcal{F}^\pm \in (W^{2,q}(\hat{\mathcal{S}}))^{5 \times 4}$, we have the inequality:

$$|E_{\partial\mathcal{K}}(W_h^-, \mathcal{F}^\pm)| \leq C(\hat{\mathcal{S}}) \|E_{\partial\mathcal{K}}\|_{2,q,\hat{\mathcal{S}}}^* [\mathcal{F}^\pm]_{2,q,\hat{\mathcal{S}}}, \quad (68)$$

with:

$$\|E_{\partial\mathcal{K}}\|_{2,q,\hat{\mathcal{S}}}^* := \sup_{0 \neq \mathcal{F}^\pm \in (W^{2,q}(\hat{\mathcal{S}}))^{5 \times 4}} \frac{|E_{\partial\mathcal{K}}(W_h^-, \mathcal{F}^\pm)|}{\|\mathcal{F}^\pm\|_{2,q,\hat{\mathcal{S}}}}.$$

The semi-norms $[\mathcal{F}^\pm]_{2,q,\hat{\mathcal{S}}_m}$, $1 \leq m \leq 8$, can be expressed as a semi-norm with respect to \mathcal{S}_m using the following inequality (Ciarlet (Ref. 13), p. 246):

$$[\mathcal{F}^\pm]_{2,q,\hat{\mathcal{S}}_m} \leq C |J_{F_S^{-1}}|_{0,\infty,\mathcal{S}_m}^{1/q} (|[FS]_{1,\infty,\hat{\mathcal{S}}_m}^2|_{\mathcal{F}^\pm}|_{2,q,\mathcal{S}_m} + |[FS]_{2,\infty,\hat{\mathcal{S}}_m}|_{\mathcal{F}^\pm}|_{1,q,\mathcal{S}_m}). \quad (69)$$

The semi-norms $[[FS]]_{k,\infty,\hat{\mathcal{S}}_m}$, $k \in \{1, 2\}$ can be directly estimated from the isoparametric mapping G_K :

$$[[FS]]_{1,\infty,\hat{\mathcal{S}}_m} \leq Ch_{\mathcal{T}}, \quad (70)$$

$$[[FS]]_{2,\infty,\hat{\mathcal{S}}_m} = 0. \quad (71)$$

Introducing (69)-(71) into (68) and using the assumption on the Jacobian of G_K^{-1} , restricted to \mathcal{S} , as stated in Lemma 3.3.5, we obtain an improved estimate for $|E_{\partial\mathcal{K}}|$:

$$|E_{\partial\mathcal{K}}(W_h^-, \mathcal{F}^\pm)| \leq Ch_{\mathcal{T}}^{5-3/q} |\mathcal{F}^\pm|_{2,q,\partial\mathcal{K}} \|\hat{W}_h^-\|_{0,\infty,\hat{\mathcal{S}}}, \quad (72)$$

where the positive constant C is independent of $h_{\mathcal{T}}$, \mathcal{F}^\pm and \hat{W}_h , but depends on the grid velocity.

For $(s-2)q \geq 1$ we have $W^{s-1/q,q}(\hat{\mathcal{S}}) \subseteq W^{2,q}(\hat{\mathcal{S}})$, which implies that inequality (72) is also valid for $\mathcal{F}^\pm \in W^{s-1/q,q}(\hat{\mathcal{S}})$. This provides more flexibility to choose optimal values of s and q in the estimates for the truncation error discussed later, but does not improve the Bramble-Hilbert estimate.

The test functions W_h are chosen from the finite dimensional space $V_h^1(\mathcal{T}_h^n)$, which implies that $W_h \in (W_B^{t,p}(\mathcal{T}_h^n))^5$ with $t \geq 1$ and $\frac{1}{p} + \frac{1}{q} = 1$, because $\mathcal{F} \in (W_B^{s,q}(\mathcal{T}_h^n))^{5 \times 4}$. Since all norms are equivalent in a finite dimensional space we can use a homogeneity argument (see Brenner and Scott (Ref. 11)) to obtain the following inequality:

$$\begin{aligned} \|\hat{W}_h\|_{1,\infty,\hat{\mathcal{K}}} &\leq C |J_{G_K^{-1}}|_{0,\infty,\mathcal{K}}^{1/p} (\|W_h\|_{0,p,\mathcal{K}} + |G_K|_{1,\infty,\hat{\mathcal{K}}} |W_h|_{1,p,\mathcal{K}}) \\ &\leq Ch_{\mathcal{T}}^{-4/p} \|W_h\|_{1,p,\mathcal{K}}, \quad \text{if } 0 < h_{\mathcal{T}} \leq 1. \end{aligned} \quad (73)$$

Together with the trace theorem, we can use (73) to obtain the following estimate for $|E_{\partial\mathcal{K}}|$:

$$\begin{aligned} |E_{\partial\mathcal{K}}(W_h^-, \mathcal{F}^\pm)| &\leq Ch_{\mathcal{T}}^{5-3/q} |\mathcal{F}^\pm|_{2,q,\partial\mathcal{K}} \|\hat{W}_h^-\|_{0,\infty,\hat{\mathcal{S}}} \\ &\leq Ch_{\mathcal{T}}^{5-3/q} |\mathcal{F}^\pm|_{2,q,\partial\mathcal{K}} \|\hat{W}_h\|_{1,\infty,\hat{\mathcal{K}}} \\ &\leq Ch_{\mathcal{T}}^{2-1/p} |\mathcal{F}^\pm|_{2,q,\partial\mathcal{K}} \|W_h\|_{1,p,\mathcal{K}}, \end{aligned} \quad (74)$$

with $0 < h_{\mathcal{T}} \leq 1$. In the last step we used the relation $\frac{1}{p} + \frac{1}{q} = 1$. \square



As discussed in Section 2.2.4.2 we can also use a product Gauss quadrature rule to approximate (57). A two-point quadrature rule is applied for the three spatial computational coordinates ξ_1, ξ_2 and ξ_3 , and a three-point quadrature rule for the temporal computational coordinate ξ_4 . Define the quadrature error functional $E_{\partial\mathcal{K}}^G$ for the integration of the element face fluxes at $\partial\mathcal{K}$ in the same way as $E_{\partial\mathcal{K}}$ in (67) with the Taylor quadrature rule replaced with the product Gauss quadrature rule. An upper bound for the quadrature error of the flux integrals over $\partial\mathcal{K}$ using the product Gauss quadrature rule is provided by the following lemma:

Lemma 3.3.7 *Let the tessellation \mathcal{T}_h^n be as in Lemma 3.3.5. Let $\mathcal{F} \in (W_B^{s,q}(\mathcal{T}_h^n))^{5 \times 4}$, with $s, q \in \mathbb{R}, 1 \leq q < \infty, s$ integer when $q = 1, sq > 4, (s - 2)q \geq 1$, and $W_h \in V_h^1(\mathcal{T}_h^n)$, then the quadrature error $|E_{\partial\mathcal{K}}^G|$ can be estimated for all $\mathcal{K} \in \mathcal{T}_h^n$ as:*

$$|E_{\partial\mathcal{K}}^G(W_h^-, \mathcal{F}^\pm)| \leq Ch_{\mathcal{T}}^{2-1/p} |\mathcal{F}^\pm|_{2,q,\partial\mathcal{K}} \|W_h\|_{1,p,\mathcal{K}},$$

with $\frac{1}{p} + \frac{1}{q} = 1$, and C a positive constant independent of $h_{\mathcal{T}}, \mathcal{F}^\pm$ and W_h , but dependent on the grid velocity.

Given the expressions of the geometric quantities in Appendix C, the product Gauss quadrature rule with two points in the spatial directions and three in the temporal direction is exact if $\hat{W}_h \in (Q_1(\hat{\mathcal{S}}))^5$ and $\mathcal{F}^\pm \in (Q_1(\hat{\mathcal{S}}))^{5 \times 4}$ and we can apply the Bramble-Hilbert lemma in the same way as for Lemma 3.3.5. The remaining part of the proof is nearly identical to Lemma 3.3.5 and is not repeated here. \square

Remark 3.3.8 *The product Gauss quadrature rule with two points in the spatial directions and three in the temporal direction uses the minimum number of quadrature points in a product Gauss quadrature rule necessary to satisfy the requirements of the Bramble-Hilbert lemma, which is used in the proof of Lemma 3.3.7.*

Remark 3.3.9 *Since the Gauss quadrature rule does not use derivatives we can relax the condition $(s - 1)q > 4$ to $sq > 4$ to ensure the validity of the quadrature rule. For more details, see Lemma 3.3.3.*

3.3.7 Analysis of element volume quadrature error

The quadrature error functional $E_{\mathcal{K}}$ for the integration of the element volume fluxes can be defined as:

$$E_{\mathcal{K}}(W_h, \mathcal{F}) = \int_{\hat{\mathcal{K}}} \frac{\partial W_{h,i}}{\partial x_j} \left(\mathcal{F}_{ij}(\xi) - \mathcal{F}_{ij}(0) - \xi_l \frac{\partial \mathcal{F}_{ij}(0)}{\partial \xi_l} \right) |J_{G_{\mathcal{K}}}| d\hat{\mathcal{K}} \quad (75)$$

using (58) and (60). The following lemma provides an upper bound for the error in the approximation of the volume flux integrals:

Lemma 3.3.10 *Let the tessellation \mathcal{T}_h^n be as in Lemma 3.3.5. Let $\mathcal{F} \in (W_B^{s,q}(\mathcal{T}_h^n))^{5 \times 4}$, with $s, q \in \mathbb{R}$, $1 \leq q < \infty$, $(s-1)q > 4$, $(s-2)q \geq 1$, s integer when $q = 1$, and $W_h \in V_h^1(\mathcal{T}_h^1)$, then the quadrature error $|E_{\mathcal{K}}|$ can be estimated for all $\mathcal{K} \in \mathcal{T}_h^n$ as:*

$$|E_{\mathcal{K}}(W_h, \mathcal{F})| \leq Ch_{\mathcal{T}}^{6-4/q} |\mathcal{F}|_{2,q,\mathcal{K}_j^n} \|W_h\|_{1,p,\mathcal{K}}, \quad (76)$$

with $\frac{1}{p} + \frac{1}{q} = 1$, and C a constant independent of h_k , \mathcal{F} and W_h .

The quadrature error $E_{\mathcal{K}}(W_h, \mathcal{F})$ can be estimated as:

$$\begin{aligned} |E_{\mathcal{K}}(W_h, \mathcal{F})| &\leq \int_{\hat{\mathcal{K}}} \left| \frac{\partial W_{h,i}}{\partial x_j} \right| |\mathcal{F}_{ij}(\xi) - \mathcal{F}_{ij}(0) - \xi_l \frac{\partial \mathcal{F}_{ij}(0)}{\partial \xi_l}| |J_{G_{\mathcal{K}}}| d\hat{\mathcal{K}} \\ &\leq Ch_{\mathcal{T}}^4 \| \mathcal{F} \|_{1,\infty,\hat{\mathcal{K}}} \| W_h \|_{1,\infty,\mathcal{K}} \\ &\leq Ch_{\mathcal{T}}^4 \| \mathcal{F} \|_{s,q,\hat{\mathcal{K}}} \| W_h \|_{1,\infty,\mathcal{K}}, \end{aligned}$$

where we used the imbedding (66), which is valid since $(s-1)q > 4$. In addition we used fact that $|\xi| \leq 2$ for $\xi \in \hat{\mathcal{K}}$ and the estimate $\int_{\hat{\mathcal{K}}} |J_{G_{\mathcal{K}}}| d\hat{\mathcal{K}} \leq Ch_{\mathcal{T}}^4$, which can be obtained directly from the geometric integrals discussed in the appendix.

The estimate of the quadrature error functional can be improved with the generalized Bramble-Hilbert lemma (Ref. 10). Due to the close resemblance with the analysis for $E_{\partial\mathcal{K}}$ only the main steps will be discussed. For any fixed value of $W_h \in (W^{m,q}(\mathcal{K}))^5$ with $m \geq 1$, the bounded linear functional $E_{\mathcal{K}}$ satisfies the relation:

$$E_{\mathcal{K}}(W_h, \mathcal{F}) = 0, \quad \forall \mathcal{F} \in (Q_1(\hat{\mathcal{K}}))^{5 \times 4},$$

hence there is a constant $C(\hat{\mathcal{K}})$, such that for all $\mathcal{F} \in (W^{2,q}(\hat{\mathcal{K}}))^{5 \times 4}$, we have the inequality:

$$|E_{\mathcal{K}}(W_h, \mathcal{F})| \leq C(\hat{\mathcal{K}}) \| E_{\mathcal{K}} \|_{2,q,\hat{\mathcal{K}}}^* [\mathcal{F}]_{2,q,\hat{\mathcal{K}}}$$

with:

$$\| E_{\mathcal{K}} \|_{2,q,\hat{\mathcal{K}}}^* := \sup_{0 \neq \mathcal{F} \in (W^{2,q}(\hat{\mathcal{K}}))^{5 \times 4}} \frac{|E_{\mathcal{K}}(W_h, \mathcal{F})|}{\| \mathcal{F} \|_{2,q,\hat{\mathcal{K}}}} \leq Ch_{\mathcal{T}}^4 \| W_h \|_{1,\infty,\mathcal{K}}.$$

Using the following inequalities (69)-(71), which are also valid with $\hat{\mathcal{S}}_m$ replaced with $\hat{\mathcal{K}}$ and \mathcal{S}_m with \mathcal{K} , we obtain the following estimate:

$$|E_{\mathcal{K}}(W_h, \mathcal{F})| \leq Ch_{\mathcal{T}}^{6-4/q} |\mathcal{F}|_{2,q,\mathcal{K}_j^n} \| W_h \|_{1,\infty,\mathcal{K}}. \quad (77)$$

The estimate (76) then results from the fact that the W_h are chosen from the finite dimensional space $V_h^1(\mathcal{T}_h^n)$ in which all norms are equivalent. \square

We can also approximate (58) with a three point product Gauss quadrature rule and define the quadrature error functional $E_{\mathcal{K}}^G$ for the integration of the element volume fluxes in the same way as $E_{\mathcal{K}}$ in (75) with the Taylor quadrature rule replaced with the product Gauss quadrature rule.

An upper bound for the quadrature error of the volume flux integrals using the three point product Gauss quadrature rule is provided by the following lemma:

Lemma 3.3.11 *Let the tessellation \mathcal{T}_h^n be as in Lemma 3.3.5. Let $\mathcal{F} \in (W_B^{s,q}(\mathcal{T}_h^n))^{5 \times 4}$, with $s, q \in \mathbb{R}$, $1 \leq q < \infty$, $sq > 4$, $(s-2)q \geq 1$, s integer when $q = 1$, and $W_h \in V_h^1(\mathcal{T}_h^1)$, then the quadrature error $|E_{\mathcal{K}}^G|$ can be estimated for all $\mathcal{K} \in \mathcal{T}_h^n$ as:*

$$|E_{\mathcal{K}}^G(W_h, \mathcal{F})| \leq Ch_{\mathcal{T}}^{6-4/q} |\mathcal{F}|_{2,q,\mathcal{K}_j^n} \|W_h\|_{1,p,\mathcal{K}}, \quad (78)$$

with $\frac{1}{p} + \frac{1}{q} = 1$, and C a constant independent of h_k , \mathcal{F} and W_h .

The three point product Gauss quadrature rule is exact if $\hat{W}_h \in (Q_1(\hat{\mathcal{S}}))^5$ and $\mathcal{F} \in (Q_1(\hat{\mathcal{S}}))^{5 \times 4}$ and we can apply the Bramble-Hilbert lemma in the same way as for Lemma 3.3.10. The remaining part of the proof is nearly identical to Lemma 3.3.10 and is not repeated here. \square

3.3.8 Truncation error of space-time discontinuous Galerkin discretization

The effect of the quadrature rule on the accuracy of the discontinuous Galerkin discretization can be investigated by analyzing the truncation error. If we integrate (54) by parts, and introduce the numerical discretization operator $L_h : V_h(\mathcal{T}_h^n) \rightarrow V_h^1(\mathcal{T}_h^n)$, then we can write the weak formulation for the DG discretization as:

Find an $\mathcal{F}_h \in V_h^1(\mathcal{T}_h^n)$, such that for all $W_h \in V_h^1(\mathcal{T}_h^n)$:

$$(L_h(\mathcal{F}_h), W_h)_{\mathcal{E}_h} = 0,$$

with $\mathcal{E}_h = \cup_{n=0}^{N_T} \cup_{j=1}^{N_n} \mathcal{K}_j^n$ and:

$$(U, V)_{\mathcal{E}_h} = \sum_{n=0}^{N_T} \sum_{j=1}^{N_n} \int_{\mathcal{K}_j^n} U \cdot V d\mathcal{K}, \quad \forall U, V \in V_h(\mathcal{T}_h^n).$$

The operator $L_h(\mathcal{F}_h)$ therefore is an approximation to $\text{div} \mathcal{F}$. We can state now the following proposition, which provides information about the truncation error of the numerical discretization, including the effect of the Taylor quadrature for the flux integrals.

Proposition 3.3.12 *Let the tessellation \mathcal{T}_h^n be as in Lemma 3.3.5, with $h_{\mathcal{T}}$ the diameter of the smallest ball containing the elements $\mathcal{K} \in \mathcal{T}_h^n$, with $h_{\mathcal{T}} \leq 1$. Let $W_h \in V_h^1(\mathcal{T}_h^1)$ and $\mathcal{F} \in (W_B^{t,q}(\mathcal{T}_h^n))^{5 \times 4}$ with $s, t, q \in \mathbb{R}$, $1 < q < \infty$, $(s-1)q > 4$, $(s-2)q \geq 1$, and $0 \leq s \leq t$, then the truncation error of the approximation to $\text{div}\mathcal{F}$ in each space-time element $\mathcal{K} \in \mathcal{T}_h^n$ is equal to:*

$$\begin{aligned} \|L_h(\mathcal{F}) - \text{div}\mathcal{F}\|_{s,q,\mathcal{T}_h^n} &\leq C_0 h_{\mathcal{T}}^{t-s} \|\mathcal{F}(U)\|_{t+1,q,\mathcal{T}_h^n} + C_1 h_{\mathcal{T}}^{6-4/q} [\mathcal{F}(U)]_{2,q,\mathcal{T}_h^n} + \\ &C_2 h_{\mathcal{T}}^{2-1/p} (\|\mathcal{F}^+(U)\|_{2,q,\mathcal{T}_h^n} + \|\mathcal{F}^-(U)\|_{2,q,\mathcal{T}_h^n}), \end{aligned} \quad (79)$$

with $\frac{1}{p} + \frac{1}{q} = 1$, and C_i , $i = 0, \dots, 2$, positive constants independent of \mathcal{F} and $h_{\mathcal{T}}$. The constant C_2 depends on the grid velocity.

We split the truncation error in each element $\mathcal{K} \in \mathcal{T}_h^n$ into a contribution related to the interpolation error and a contribution related to the discontinuous Galerkin discretization:

$$\begin{aligned} \|L_h(\mathcal{F}) - \text{div}\mathcal{F}\|_{s,q,\mathcal{K}} &\leq \|\text{div}\mathcal{F} - \mathbb{P}_{V_h^1(\mathcal{T}_h^n)}(\text{div}\mathcal{F})\|_{s,q,\mathcal{K}} + \\ &\|L_h(\mathcal{F}) - \mathbb{P}_{V_h^1(\mathcal{T}_h^n)}(\text{div}\mathcal{F})\|_{s,q,\mathcal{K}} \end{aligned} \quad (80)$$

$$= e_1 + e_2, \quad (81)$$

with $\mathbb{P}_{V_h^1(\mathcal{T}_h^n)}$ the projection onto the space $V_h^1(\mathcal{T}_h^n)$. The contributions e_1 and e_2 are provided by Lemmas 3.3.13 and 3.3.14. If we sum (81) over all elements $\mathcal{K} \in \mathcal{T}_h^n$ and use the Minkovski inequality then we obtain the estimate (79), with the norm and semi-norms in $W_B^{s,q}(\mathcal{T}_h^n)$ defined in Appendix A. \square

Lemma 3.3.13 *Let the tessellation \mathcal{T}_h^n be as in Lemma 3.3.5 and assume that each $\mathcal{K} \in \mathcal{T}_h^n$ is star shaped with respect to some ball. Suppose $s, t, q \in \mathbb{R}$ with $1 \leq q \leq \infty$ and either $(t-1)q > 4$ when $q > 1$ or $t \geq 5$ when $q = 1$. Then for all $\mathcal{F} \in (W^{t,q}(\mathcal{K}))^{5 \times 4}$ and $0 \leq s \leq t$ we have:*

$$\|\text{div}\mathcal{F} - \mathbb{P}_{V_h^1(\mathcal{T}_h^n)}(\text{div}\mathcal{F})\|_{s,q,\mathcal{K}} \leq C h_{\mathcal{T}}^{t-s} \|\mathcal{F}\|_{t+1,q,\mathcal{K}}. \quad (82)$$

For integer values of s and t this lemma is a direct consequence of Theorem 4.4.4 in Brenner and Scott (Ref. 11), because the condition $|J_{G_K^{-1}}| \leq C/h_{\mathcal{T}}^4$ also ensures that $\gamma_{\mathcal{K}} = h_{\mathcal{K}}/\rho_{\mathcal{K}} > 0$, with $\rho_{\mathcal{K}}$ the radius of the smallest sphere completely contained in \mathcal{K} . For non-integer values of s and t we use Banach space interpolation between the estimates for integer values of s and t . If we

define the operator $Tv := v - \mathbb{P}_{V_h^1(\mathcal{T}_h^n)}v$ and use the Banach space interpolation theorem for linear operators (Prop. 12.1.5 in (Ref. 11)) then we obtain with $m = [t]$ and $i = [s]$ the estimate:

$$\| T \|_{[W^{m,p}(\mathcal{K}), W^{m+1,p}(\mathcal{K})]_{\theta,p} \rightarrow [W^{i,p}(\mathcal{K}), W^{i+1,p}(\mathcal{K})]_{\theta,p}} \leq Ch_T^{m-i},$$

with $0 < \theta < 1$. Using Theorem 12.2.3 in (Ref. 11), which states that $W^{m+\theta,p}(\mathcal{K}) = [W^{m,p}(\mathcal{K}), W^{m+1,p}(\mathcal{K})]_{\theta,p}$ if the domain \mathcal{K} has a Lipschitz continuous boundary, we obtain the estimate (82) with $s = i + \theta$, $t = m + \theta$ and $v = \text{div}\mathcal{F}$. The Lipschitz condition on \mathcal{K} is satisfied because $\hat{\mathcal{K}}$ is Lipschitz and the mapping G_K , used to define $\mathcal{K} \in \mathcal{T}_h^n$ from $\hat{\mathcal{K}}$, is a C^1 diffeomorphism. \square

Lemma 3.3.14 *Let the tessellation \mathcal{T}_h^n , flux tensor \mathcal{F} , and test function W_h be as in Proposition 3.3.12, then for each $\mathcal{K} \in \mathcal{T}_h^n$ we have the estimate:*

$$\begin{aligned} \| L_h(\mathcal{F}) - \mathbb{P}_{V_h^1(\mathcal{T}_h^n)}(\text{div}\mathcal{F}) \|_{s,q,\mathcal{K}} &\leq C_1 h_T^{6-4/q} |\mathcal{F}(U)|_{2,q,\mathcal{K}} + \\ &C_2 h_T^{2-1/p} (|\mathcal{F}^+(U)|_{2,q,\partial\mathcal{K}} + |\mathcal{F}^-(U)|_{2,q,\partial\mathcal{K}}) \end{aligned}$$

with $\frac{1}{p} + \frac{1}{q} = 1$.

Define $E(W_h) = E_{\partial\mathcal{K}}(W_h) + E_{\mathcal{K}}(W_h)$ as the error functional, with $E_{\partial\mathcal{K}}$ and $E_{\mathcal{K}}$ defined in (67) and (75), respectively. To each $W_h \in (W^{m,q}(\mathcal{K}))^5$, with m integer, $\mathcal{K} \in \mathcal{T}_h^n$, we can associate the vector $P W_h := (D^\alpha W_h) \in (L_N^q(\mathcal{K}))^5$, (see Appendix A), by ordering the N multi-indices α , satisfying $|\alpha| \leq m$, in a convenient way. Let $1 \leq p < \infty$. The representation theorem for linear functions in the dual space of the Sobolev space $W^{m,p}(\mathcal{K})$ (Adams (Ref. 1), Theorem 3.8), states that there exists an element $v \in (L_N^q(\mathcal{K}))^5$, with $\frac{1}{p} + \frac{1}{q} = 1$, such that writing the vector v in the form $(v_\alpha)_{0 \leq |\alpha| \leq m}^5$ we have for all $W_h \in (W^{m,p}(\mathcal{K}))^5$ the following representation for the error functional $E(W_h)$:

$$E(W_h) = \sum_{0 \leq |\alpha| \leq m} \int_{\mathcal{K}} D^\alpha W_h v_\alpha d\hat{\mathcal{K}}. \quad (83)$$

Moreover,

$$\inf_{v \in \mathcal{B}} \| v \|_{(L_N^q(\mathcal{K}))^5} = \| E \|_{m,p,\mathcal{K}}^*, \quad (84)$$

with \mathcal{B} the set of all $v \in (L_N^q(\mathcal{K}))^5$ for which (83) holds for every $W_h \in (W^{m,p}(\mathcal{K}))^5$. For $1 < p < \infty$ the element $v \in (L_N^q(\mathcal{K}))^5$ satisfying (83) and (84) is unique. If we integrate E by parts then we obtain the representation:

$$\begin{aligned} E(W_h) &= \int_{\mathcal{K}} W_h \cdot (L_h(\mathcal{F}) - \text{div}\mathcal{F}) d\mathcal{K} \\ &= \int_{\mathcal{K}} W_h \cdot (L_h(\mathcal{F}) - \mathbb{P}_{V_h^1(\mathcal{T}_h^n)}(\text{div}\mathcal{F})) d\mathcal{K}. \end{aligned}$$

Since $v \in (L_N^q(\mathcal{K}))^5$ is unique for $1 < p < \infty$, we must have the relation:

$$v = L_h(\mathcal{F}) - \mathbb{P}_{V_h^1(\mathcal{T}_h^n)}(\operatorname{div}\mathcal{F}). \quad (85)$$

Hence, the minimum is attained when v satisfies (85), and using (84) we have the relation:

$$\| L_h(\mathcal{F}) - \mathbb{P}_{V_h^1(\mathcal{T}_h^n)}(\operatorname{div}\mathcal{F}) \|_{(L_N^q(\mathcal{K}))^5} = \| E \|_{m,p,\mathcal{K}}^*. \quad (86)$$

The space $(W^{m,q}(\mathcal{K}))^5$ is a closed subspace W of $(L_N^q)^5$ and there exists an isometric isomorphism from $(W^{m,q}(\mathcal{K}))^5$ onto $W \subset (L_N^q(\mathcal{K}))^5$ (see Adams (Ref. 1), page 46). Since $L_h(\mathcal{F}) - \operatorname{div}\mathcal{F} \in (W^{m,q}(\mathcal{K}))^5$, because $\mathcal{F} \in (W_B^{t,q}(\mathcal{T}_h^n))^{5 \times 4}$, we can therefore transform (86) into:

$$\| L_h(\mathcal{F}) - \mathbb{P}_{V_h^1(\mathcal{T}_h^n)}(\operatorname{div}\mathcal{F}) \|_{m,q,\mathcal{K}} = \| E \|_{m,p,\mathcal{K}}^*.$$

Using Banach space interpolation we can extend this relation also to noninteger values of m . For more details, see Lions (Ref. 30) and Adams (Ref. 1).

The proof is completed using the estimates provided by Lemmas 3.3.5 and 3.3.10 and the inequality $\| W_h \|_{1,p,\mathcal{K}} \leq \| W_h \|_{s,p,\mathcal{K}}$ for $s \geq 1$:

$$\begin{aligned} & \| L_h(\mathcal{F}) - \mathbb{P}_{V_h^1(\mathcal{T}_h^n)}(\operatorname{div}\mathcal{F}) \|_{s,q,\mathcal{K}} \\ & \leq \sup_{0 \neq W_h \in (W^{s,p}(\mathcal{K}))^5} \frac{|E_{\mathcal{K}}(\nabla W_h, \mathcal{F})|}{\| W_h \|_{s,p,\mathcal{K}}} + \sup_{0 \neq W_h \in (W^{s,p}(\mathcal{K}))^5} \frac{1}{2} \frac{|E_{\partial\mathcal{K}}(W_h^-, \mathcal{F}^+)|}{\| W_h \|_{s,p,\mathcal{K}}} + \\ & \quad \sup_{0 \neq W_h \in (W^{s,p}(\mathcal{K}))^5} \frac{1}{2} \frac{|E_{\partial\mathcal{K}}(W_h^-, \mathcal{F}^-)|}{\| W_h \|_{s,p,\mathcal{K}}} \\ & \leq C_1 h_{\mathcal{T}}^{6-4/q} |\mathcal{F}(U)|_{2,q,\mathcal{K}} + C_2 h_{\mathcal{T}}^{2-1/p} (|\mathcal{F}^+(U)|_{2,q,\partial\mathcal{K}} + |\mathcal{F}^-(U)|_{2,q,\partial\mathcal{K}}) \end{aligned} \quad (87)$$

with $\frac{1}{p} + \frac{1}{q} = 1$. \square

Remark 3.3.15 For $q = 1/(1 - \epsilon)$, $s > 5$ and $t \geq 7$ in Proposition 3.3.12, with $\epsilon \in \mathbb{R}^+$ an arbitrary positive number, the truncation error of the discontinuous Galerkin discretization, including the effect of the approximation of the element surface and volume integrals, is $O(h_{\mathcal{T}}^{2-\epsilon})$ in the $W_B^{s,q}(\mathcal{T}_h^n)$ norm. This shows that the Taylor quadrature rule does not negatively influence the second order accuracy of the numerical discretization, since we can choose ϵ arbitrary small.

Corrolary 3.3.16 Let the conditions of Proposition 3.3.12 be satisfied, with $(s-1)q > 4$ replaced by $sq > 4$, then the product Gauss quadrature rules defined above Lemma 3.3.7 and Lemma 3.3.11 result in the same truncation error as obtained for the Taylor quadrature rule in Proposition 3.3.12.



The proof is immediate if one uses the estimates provided by Lemmas 3.3.7 and 3.3.11 in (87).□

Remark 3.3.17 *The reader is referred to Section 4.2 for an experimental verification of the error. For a steady subsonic entropy preserving flow a global L^2 -error of the order $h_T^{2.5}$ was found from numerical experiments, using data at superconvergence points, even on locally refined meshes.*

4 Application of Space-Time Discontinuous Galerkin Methods to Aerodynamics

The space-time discontinuous Galerkin finite element method has been tested on a number of problems with increasing complexity. First we discuss results of simulations aimed at verifying and validating the algorithm and subsequently we present two and three-dimensional simulations, including a deforming wing, which demonstrate the applicability of the space-time DG method to unsteady aerodynamics.

4.1 Sod's shock tube problem

Sod's problem is one of the classical shock tube problems, see Toro (Ref. 41). Its solution consists of a left moving rarefaction wave and a right moving contact discontinuity and shock. Two simulations have been performed, one with and one without mesh adaptation. Both simulations start on a uniform mesh with 100 cells in space. The time step is chosen such that the physical CFL number $CFL_{\Delta t}$ is less than or equal to 0.9. For the simulation with mesh adaptation, in the first time step two refinements have been carried out, resulting in 21 extra cells. The minimum mesh width is now one quarter of the mesh width of the original mesh. The mesh adaptation on the initial solution is crucial because the error generated in the first time step cannot be recovered with adaptation during the simulation and a result similar to the uniform mesh solution would be obtained. In the subsequent time steps as many cells were added as removed, so the total number of cells remained constant in time. The maximum number of refinement levels has been restricted to one, which implies that no new cells with mesh widths less than half the mesh width of the original mesh are created. The adapted space-time mesh is shown in Figure 8. The space-time mesh clearly shows the structure of the solution and the adaptation based on coarsening and refinement of elements follows the discontinuities without smearing. The flow solutions on the uniform and adapted mesh at $t = 0.2531$ are shown in Figure 9. Clearly, the solution on the adapted mesh compares better with the exact solution. The flow solutions for Sod's problem have been obtained with dissipation model II, which results in nearly monotone solutions around the discontinuities. For all other subsonic and transonic problems the simpler dissipation model I is sufficient.

4.2 Accuracy study of the discontinuous Galerkin discretization

The local element-wise discretization obtained with discontinuous Galerkin methods combines well with local mesh refinement and the discretization does not strongly depend on the mesh smoothness. It must, however, be verified if the DG method maintains its accuracy on non-smooth meshes resulting from h -refinement. In order to verify this an accuracy study has been conducted using different meshes and comparing the numerical solution with the exact solution. For this purpose the subsonic two-dimensional flow through a channel with a \sin^3 bump is simulated on a

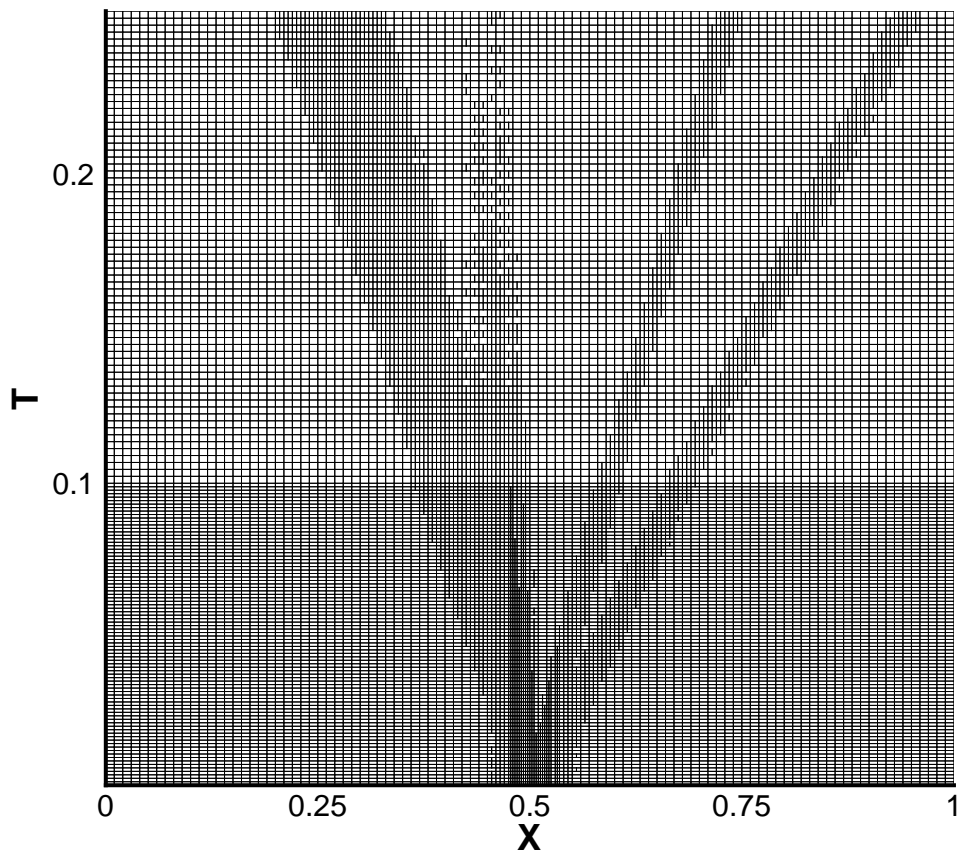


Fig. 8 Space-time mesh for the adaptive solution of Sod's shock tube problem.

Table 1 Number of mesh points in uniformly and adaptively refined meshes

	coarse grid	medium grid	fine grid
original	800	3200	12800
one adaptation	1120	4480	17920
two adaptations	1568	6272	25088

sequence of meshes with 800, 3200, and 12800 elements. The coarsest mesh is shown in Figure 10.

At the inflow boundary total pressure, total temperature, and the velocity direction (normal to the inflow plane) are prescribed. At the outflow boundary the freestream pressure is prescribed. Since the entropy p/ρ^γ should be conserved in subsonic isentropic flow, the L^2 -norm of the difference between the computed entropy and the freestream value is taken as a measure for the discretization error. In Figure 11 the L^2 -norm of the error is plotted for uniformly refined meshes. The L^2 -error is proportional with $h^{5/2}$, which is better than the theoretical results presented by Cockburn (Ref. 18) for the linear advection equation. This can be attributed to the fact that we use the data in the element center at t_{n+1}^- , which can be shown with a simple wave analysis for the linear advection equation to be $O(h)$ more accurate than the data at the element faces.

Each of the three meshes is also locally refined in two steps in order to test the accuracy of the method on non-smooth meshes with hanging nodes. At each adaptation step, the mesh size is increased with 40%. Since the mesh adaptation parameters are the same for all three grids, the fine to coarse meshes have the following property: for an arbitrary region of the mesh the average mesh width is halved with respect to the average mesh width in the next coarser mesh for the same region. Hence the series is suited for a grid convergence study to obtain the discretization error of the DG scheme on hanging nodes. A survey of the number of mesh points is given in Table 4.2. In the adaptation the correct geometry of the bump is preserved. A view of the one time adapted mesh, which initially has 800 mesh points, is shown in Figure 10. The L^2 -norm of the error on the adapted meshes is shown in Figure 11, which clearly demonstrates that the L^2 -error on locally refined meshes in the discontinuous Galerkin discretization has the same mesh dependence $h^{5/2}$ as on the uniformly refined meshes, despite the fact that the adapted mesh contains hanging nodes and is non-smooth.

4.3 Comparison of Taylor and Gauss quadrature

4.3.1 Aerodynamic forces

A first comparison of the two point product Gauss quadrature rule and the Taylor quadrature rule is presented in Figure 12. Transonic flow over a NACA0012 airfoil has been simulated with a

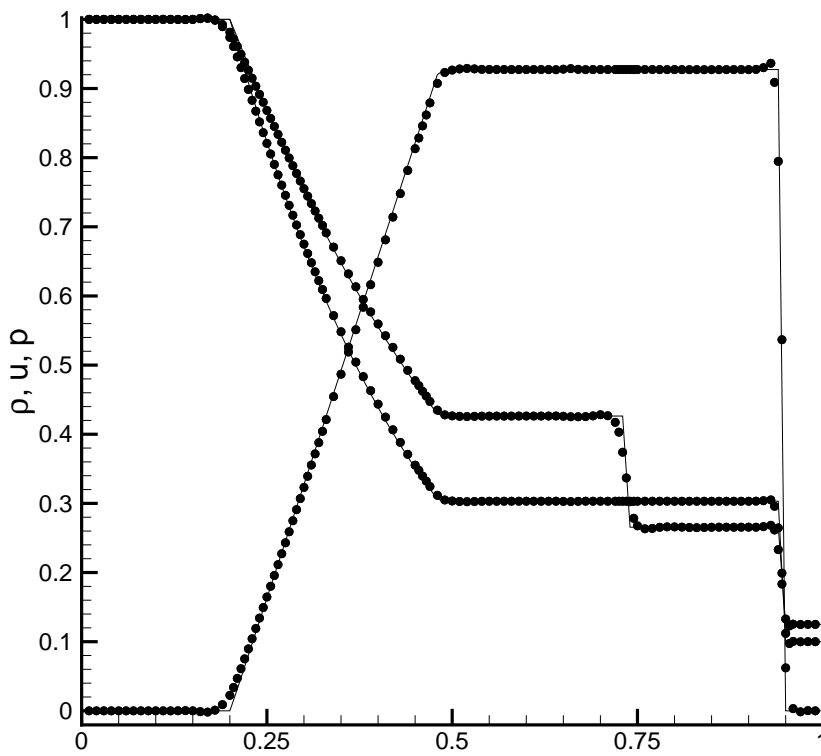
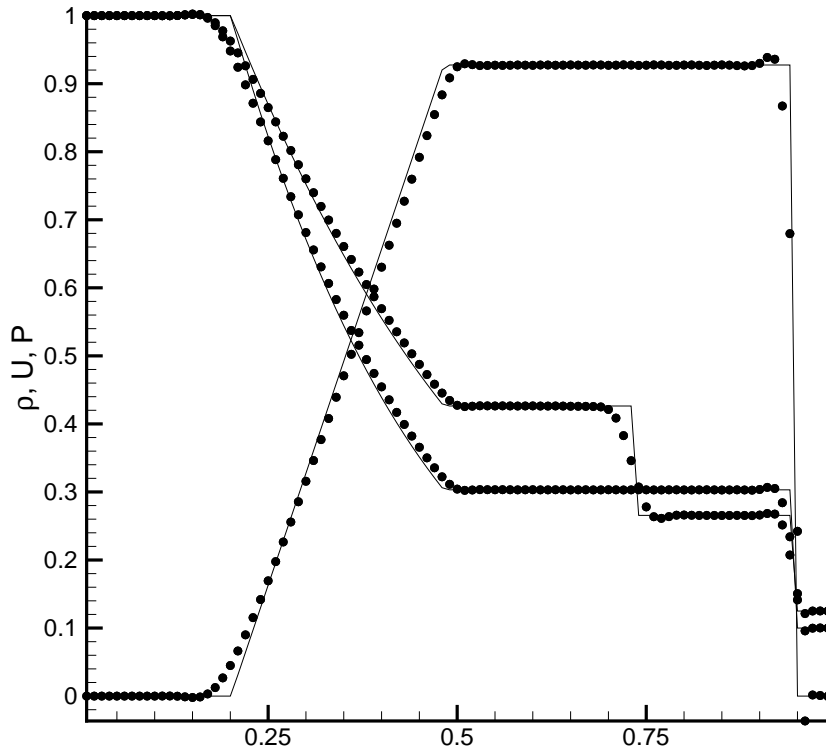


Fig. 9 Results of Sod's shock tube problem at $t = 0.2531$ on a uniform (top) and adapted mesh (bottom). Computed results plotted as circles, exact solution plotted as lines.

freestream Mach number of 0.8, and an angle of attack of 2 degrees. Both the Taylor and product Gauss quadrature rules have been used. Clearly, the results in Figure 12 show hardly any difference in the pressure distribution over the airfoil. The lift coefficient are computed to be 0.5387 for the Taylor quadrature rule, and 0.5348 for the Gauss quadrature rule. The small increase in lift is most probably caused by the fact that the Taylor quadrature rule is slightly less dissipative.

4.3.2 Slip flow boundary

In an interesting article, Bassi and Rebay (Ref. 4) found that the second order DG method using first order polynomials for both the flow representation and the geometry elements produced a severe numerical boundary layer for the inviscid subsonic flow past a cylinder. Bassi et al. apply the standard steady-state RKDG algorithm of Cockburn et al. (Ref. 16), but without the use of a limiter, since the flow is subsonic. In their simulations they used an exact Riemann solver, the equations were discretized on a triangular mesh, and a Gauss quadrature rule was used to evaluate the flux integrals.

The numerical experiment of Bassi and Rebay has been repeated. Subsonic flow past a cylinder has been simulated at a Mach number $M_\infty = 0.38$, on a fine 64×96 mesh and a coarse 32×48 mesh, both with rectangular elements, which are described using the bilinear isoparametric map. On the

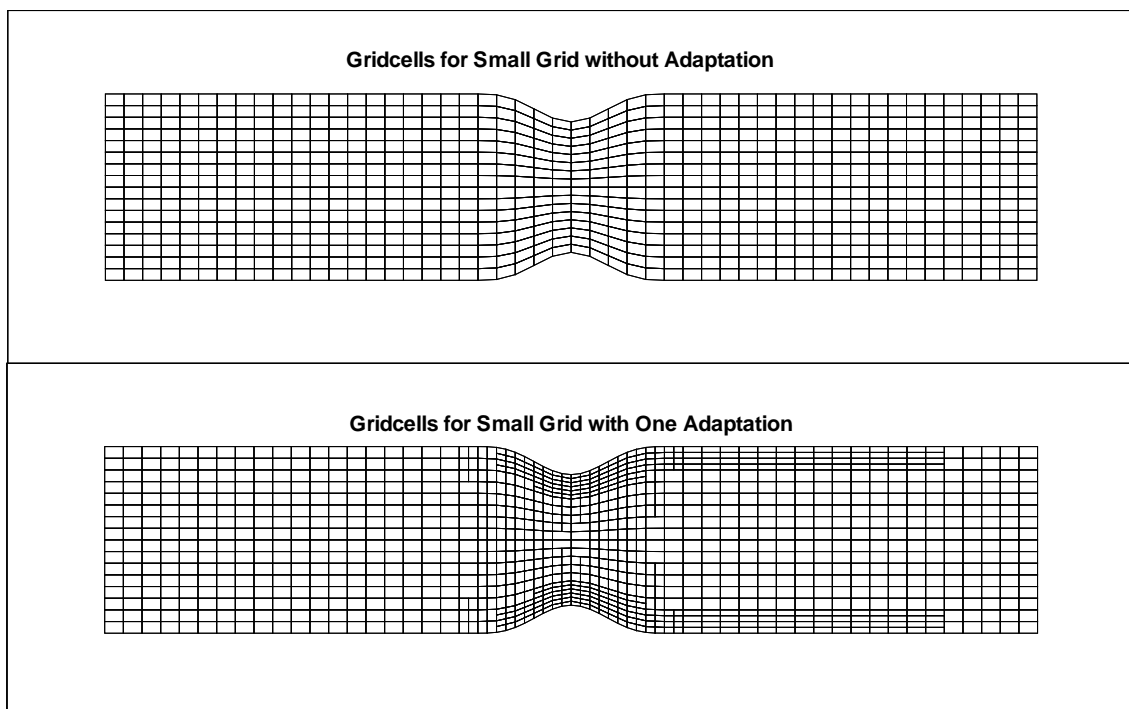


Fig. 10 Original and one time adapted mesh for converging-diverging channel.

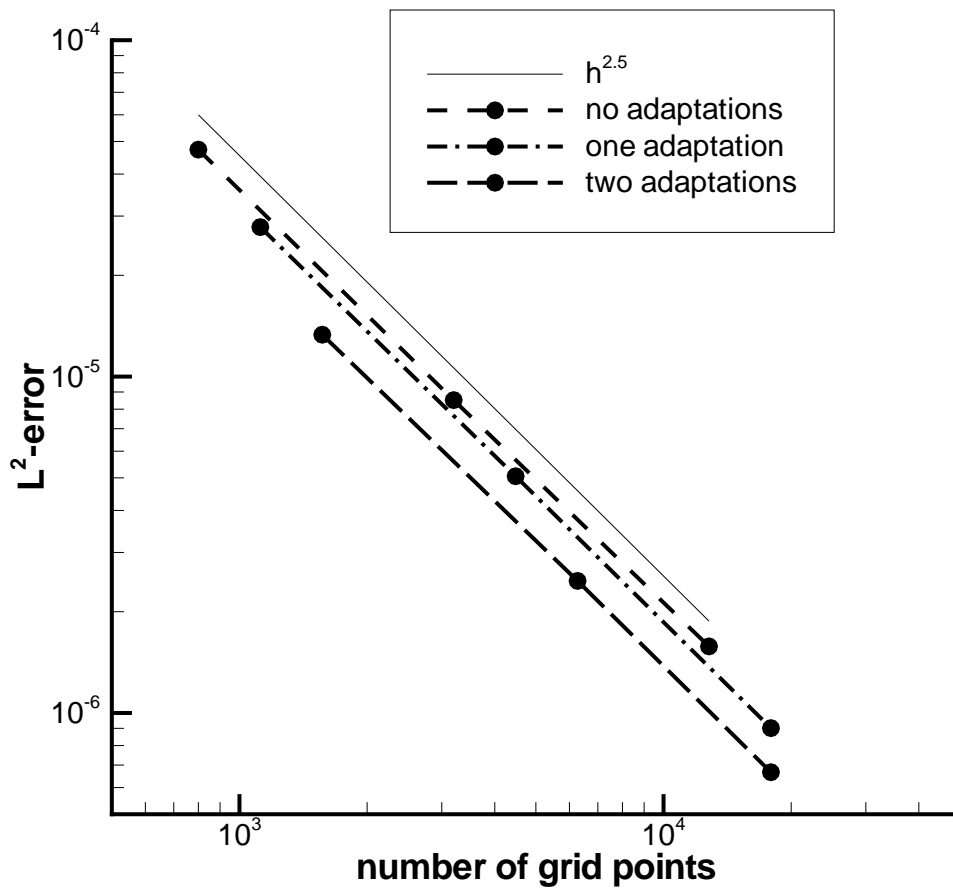


Fig. 11 L^2 -Error in flow calculations for converging-diverging channel on uniform and adapted meshes.

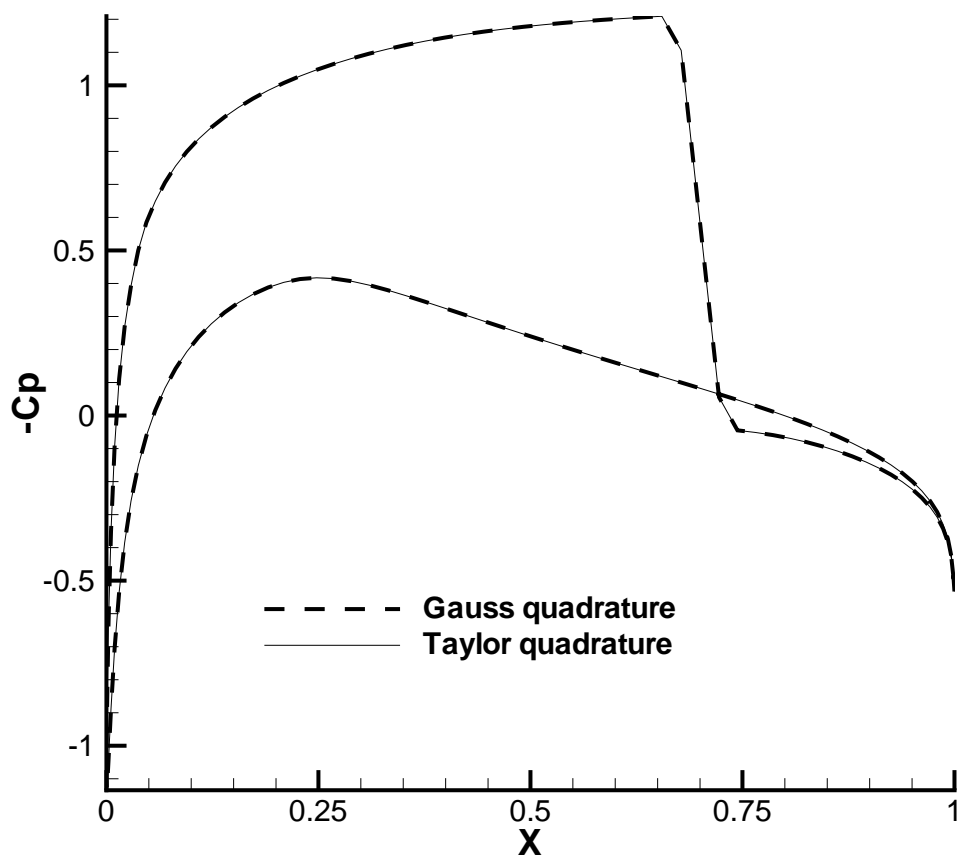


Fig. 12 Comparison of pressure distribution for the transonic over a NACA0012 foil.

coarse mesh also a quadratic superparametric representation of the boundary has been used. Both the Gauss and Taylor quadrature rule have been applied. No artificial dissipation has been added, and all simulations have been converged to machine accuracy. The numerical boundary layers are presented in Figure 13; the numerical boundary layer is represented by the total pressure loss, defined as:

$$p_{t-loss} = 1 - \frac{p}{p_\infty} \left(\frac{1 + \frac{1}{2}(\gamma - 1)M^2}{1 + \frac{1}{2}(\gamma - 1)M_\infty^2} \right)^{\frac{\gamma}{\gamma-1}},$$

where M is the local Mach number, and γ is the ratio of specific heats. Clearly, the Taylor quadrature rule results in a significant reduction of the numerical boundary layer. This difference can be attributed to the fact that in the Gauss quadrature rule the normal flux is computed at different locations in the element face. At each quadrature point we consider a one-dimensional Riemann problem and neglect the tangential variation of the solution in the element face. The tangential vectors at the quadrature points are slightly different and this results in different shear wave contributions from the quadrature points, which manifest themselves in spurious entropy generation near the wall. The Taylor quadrature rule considers the Riemann problem only at one point and therefore results in a more consistent discretization when combined with one-dimensional (approximate) Riemann solvers.

Bassi and Rebay reported that it was mandatory to use higher order boundary representation in order to get correct results. In particular, their numerical boundary was found *not* to disappear under grid refinement. This may have been caused by the fact that their computation failed to converge on the finer meshes. Though they do not present a total pressure loss distribution for linear boundary elements, the strength of the numerical wake shown in the Mach field plots, would imply a total pressure loss far exceeding 10%, which is more than experienced in our simulations. As shown in Figure 13, a superparametric boundary representation does improve the flow results, but since the numerical boundary layer on the coarse mesh is not all that bad, the improvement is not as dramatic as with Bassi and Rebay.

Actually, the accuracy improvement under grid refinement, uniform or local, is greater than when using superparametric elements. This is already clear from Figure 13 where the fine grid results are more accurate than the coarse superparametric results. The grid refinement efficiency is demonstrated more strongly in Figure 14, where the previous results are compared with results obtained under local grid refinement. The coarse mesh has been refined three times and the Mach number distributions are shown. The adapted meshes are obtained through local grid refinement near the cylinder, and at each adaptation the number of boundary cells in the circumferential direction is doubled. Accuracy on the one time refined mesh is comparable to the fine mesh computation, and

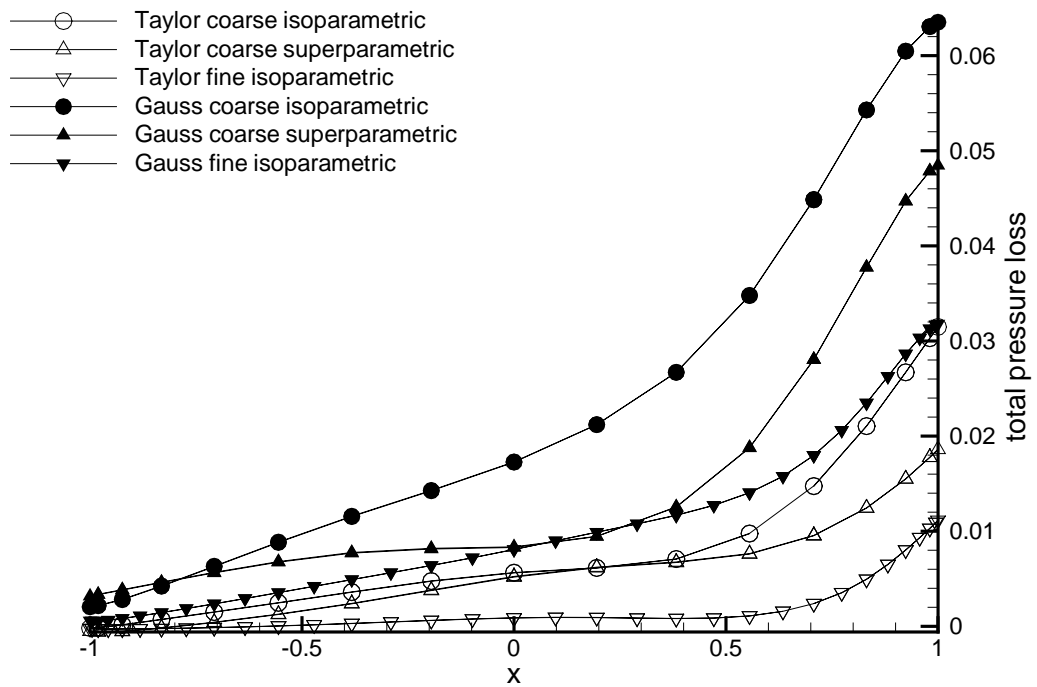


Fig. 13 Comparison of the total pressure loss at the wall for the flow around a circular cylinder ($M_\infty = 0.38$) using Gauss and Taylor flux quadrature rules for isoparametric elements on a coarse (32×48 elements) and fine mesh (64×96 elements) and superparametric elements on a coarse mesh (32×48 elements).

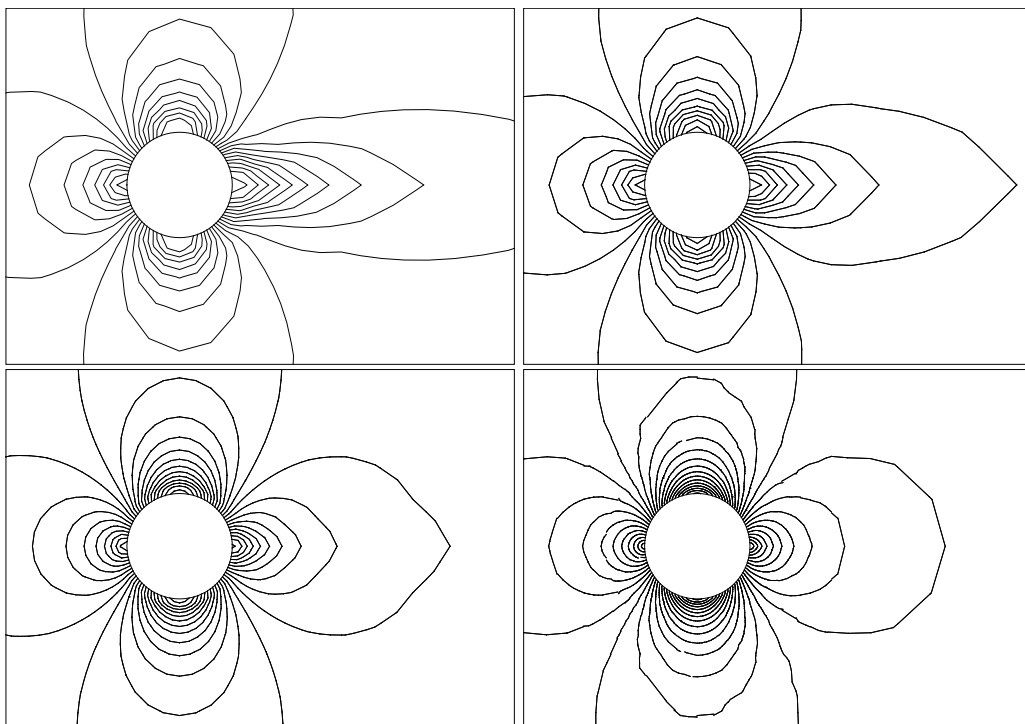


Fig. 14 Comparison of the Mach number field of a circular cylinder at $M_\infty = 0.38$ using Gauss (upper left) and Taylor quadrature with (locally refined) linear isoparametric elements (coarse mesh with 1536 cells (upper right), fine mesh with 6144 cells (lower left), and three times adapted coarse mesh with 8358 elements (lower right)).

Table 2 Performance comparison of the different methods.

method	computing time [s]	speed [Gflop/s]
Osher scheme with Gauss quadrature	1628	2.2
HLLC scheme with Gauss quadrature	754	2.9
HLLC scheme with Taylor quadrature	274	3.4

the numerical boundary layer all but disappears on the three times refined mesh (maximum total pressure loss of 0.2 percent). Hence it is not necessary to use a higher-order accurate boundary representation in order to obtain accurate simulation results. More details can be found in Van der Vegt et al. (Ref. 46).

4.3.3 Computational efficiency

Steady, subsonic flow over an ONERA M6 wing is simulated with a freestream Mach number of 0.4 and an angle of attack of six degrees. Even though the flow is stationary, it has been simulated with the space-time discretization. This example is chosen to measure the computational efficiency of the Taylor quadrature rule. Not only the quadrature rules are compared but also the numerical flux. The original version of the flow solver applied the Osher approximate Riemann solver. As explained above, for the development of the Taylor quadrature rule it proved necessary to change to the HLLC approximate Riemann solver. In Table 2 computing times and speeds for the complete execution of the flow solver are compared for three of the four combinations of quadrature rule and Riemann solver. Computing times are on a single processor NEC SX-5, for 100 multigrid cycles with one pre- and postrelaxation on a coarse mesh with 55,000 grid cells. In the transition from the Gauss quadrature rule combined with the Osher scheme to the Taylor quadrature rule combined with the HLLC scheme a speedup of six has been obtained. This is partly due to the reduced number of computations, and partly due to the data locality, which allows higher computational speeds.

4.3.4 Computational complexity of DG methods

As mentioned in the introduction, the prime motivation to develop the Taylor quadrature was to decrease the computational complexity of the DG method. In Section 4.3.3 the computational complexity of the Taylor quadrature rule has been compared with the complexity of the Gauss quadrature rule. So far, few authors have dared to compare DG methods with conventional CFD methods. In the following we will compare the DG methods with the finite volume method of Jameson, which is a very efficient algorithm for transsonic aerodynamics.

For both schemes the computationally most intensive part is the flux calculation. In Table 3 flop counts and memory I/O are presented for both methods. The analysis of the DG method is based



Table 3 Comparison of computational complexity of the space-time DG method and a Jameson finite volume scheme. The flop count is the number of floating point operations required to compute the flux through one element face. The memory access is the number of reads and writes, measured in words, required for this computation. The ratio of the flop count and memory access is also presented.

discretisation scheme	flop count	memory access [w]	ratio
finite volume	48	33	1.5
DG	885	178	5

on the Taylor quadrature rule, including the dissipative part of the HLLC flux. The analysis of the finite volume method neglects the artificial dissipative fluxes, and only the central differences are counted. Note that the finite volume method has five unknowns per cell, whereas the space-time DG method has 25 unknowns per cell.

Per cell the required flop counts is three times the tabulated flop counts (half of the six faces, since the above counts include residual updates of both cells connecting to the face). Hence a finite volume solver requires 144 flop per 5 unknowns, that is, 30 flop per unknown. The DG methods requires 2655 flops per 25 unknowns, that is, 105 flop per unknown. To balance the increase of flop with an increase in speed, a DG solver should run at four times the speed of a finite volume solver. For the DG discretisation the computation to communication ratio is more than three times larger than for the finite volume scheme. This implies that DG solvers will be less sensitive to unbalanced processor speed and bandwidth, and are expected to run at higher speeds than finite volume solvers. The average speed of the current DG solver on the NLR NEC SX-5 is 3 Gflop/s per processor, which is 37.5% of the peak speed. A typical run of a finite volume solver on the same machine runs at 1 Gflop/s per processor. For steady state simulations the convergence rate of both flow solvers are comparable. Based on the comparative speeds we can conclude that the increased number of flop counts of the DG method is balanced by its increased speed on current computer architectures.

The high computation to communication ratio of the DG method is also beneficial for cache-based scalar machines. Without any modification of the code, which has been optimised for vector architectures, the code has run at 20% of the peak speed on the Origin O3000 series. This again demonstrates that while the DG method may have a large computational complexity in terms of floating point operations, the throughput time per unknown is comparable to standard finite volume schemes.

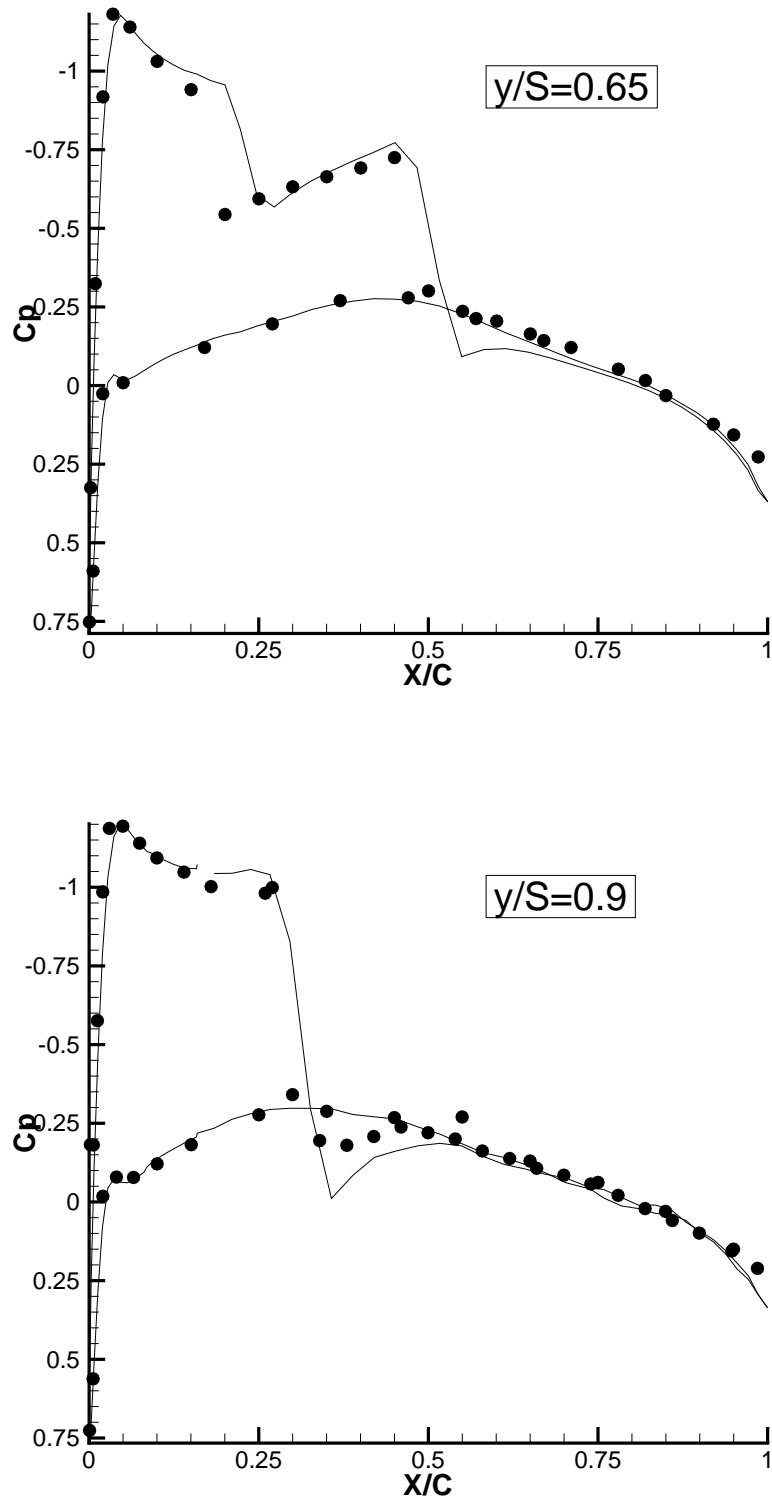


Fig. 15 Pressure coefficient C_p at 65% and 90% span for the ONERA M6 wing. Experimental results are shown with dots.

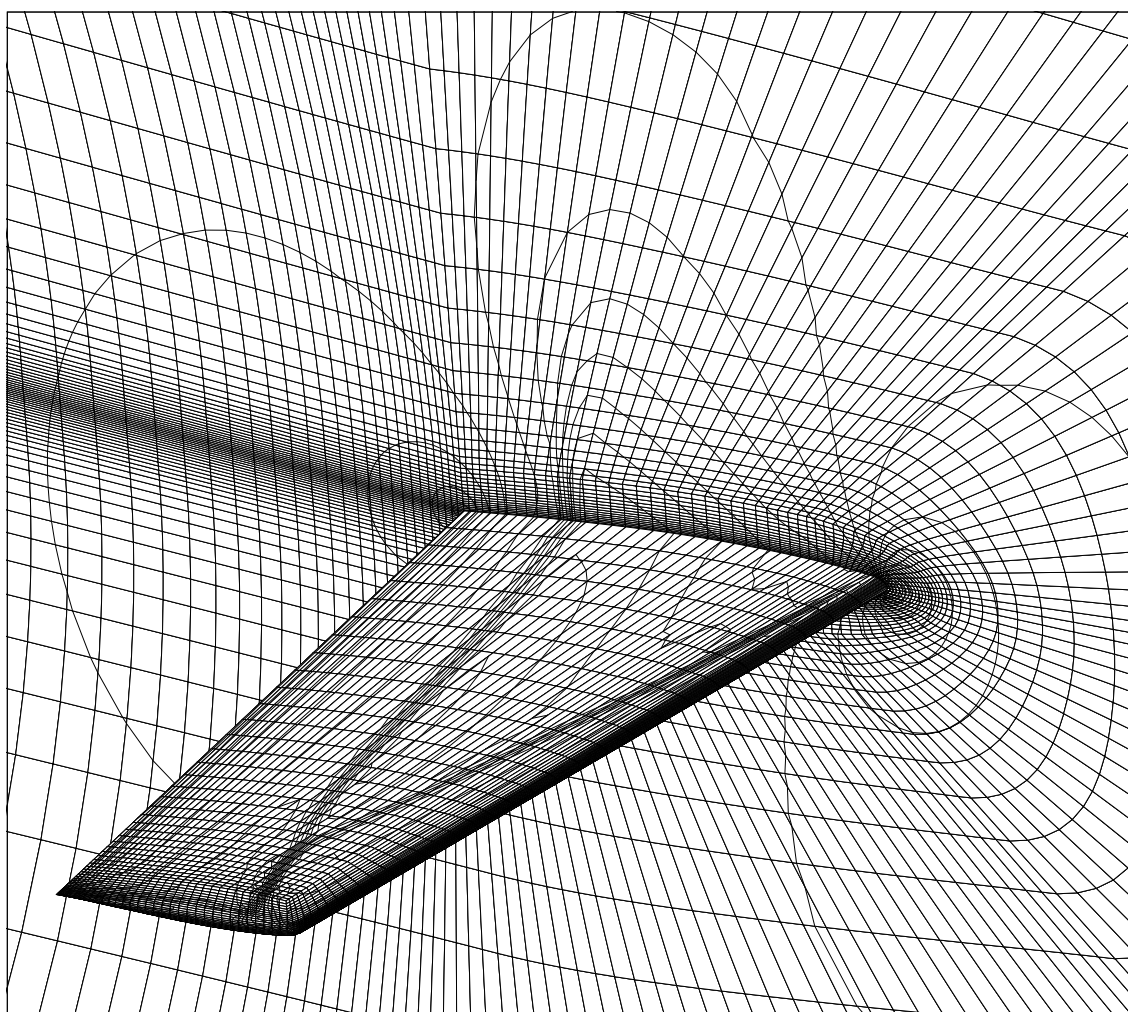


Fig. 16 Pressure distribution on wing and symmetry plane for the ONERA M6 wing.

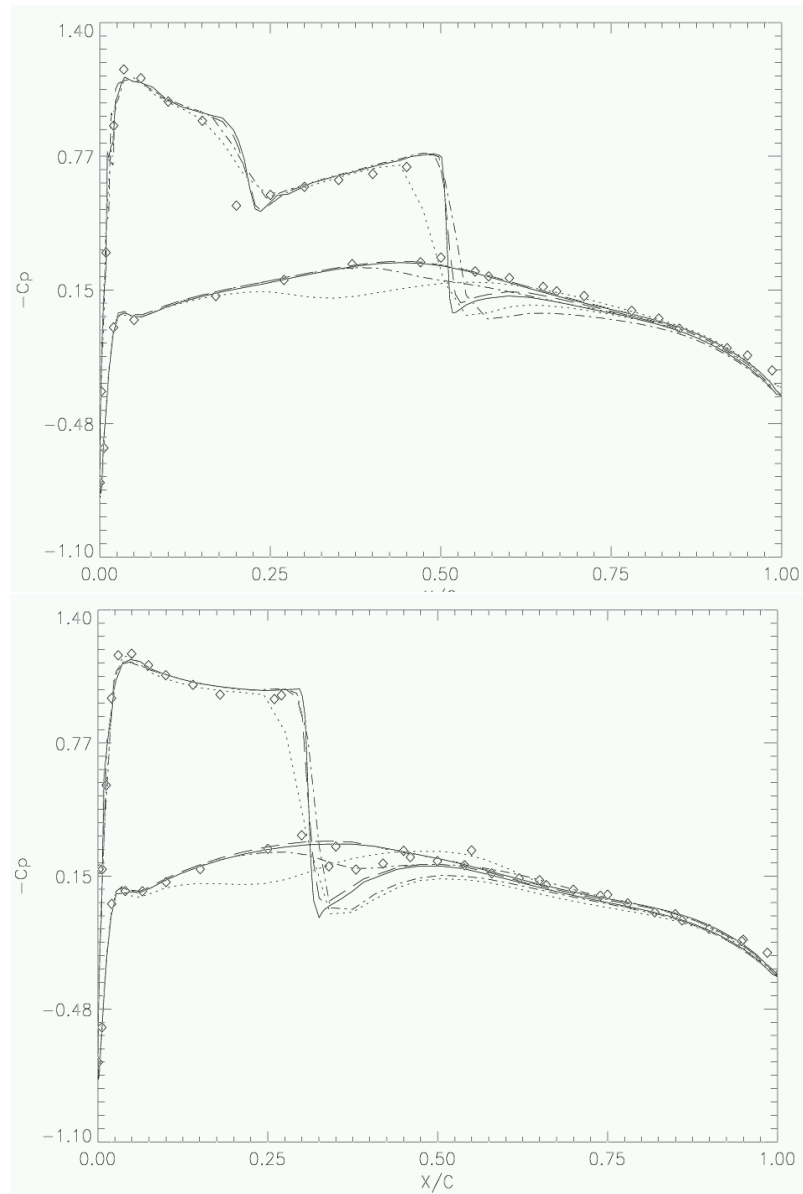


Fig. 17 Pressure coefficient C_p at 65% (top) and 90% span (bottom) for the ONERA M6 wing. (\cdots original grid, $-\ -$ one adaptation, $- \cdot -$ two adaptations, $—$ three adaptations, $\diamond \diamond \diamond$ experiment).

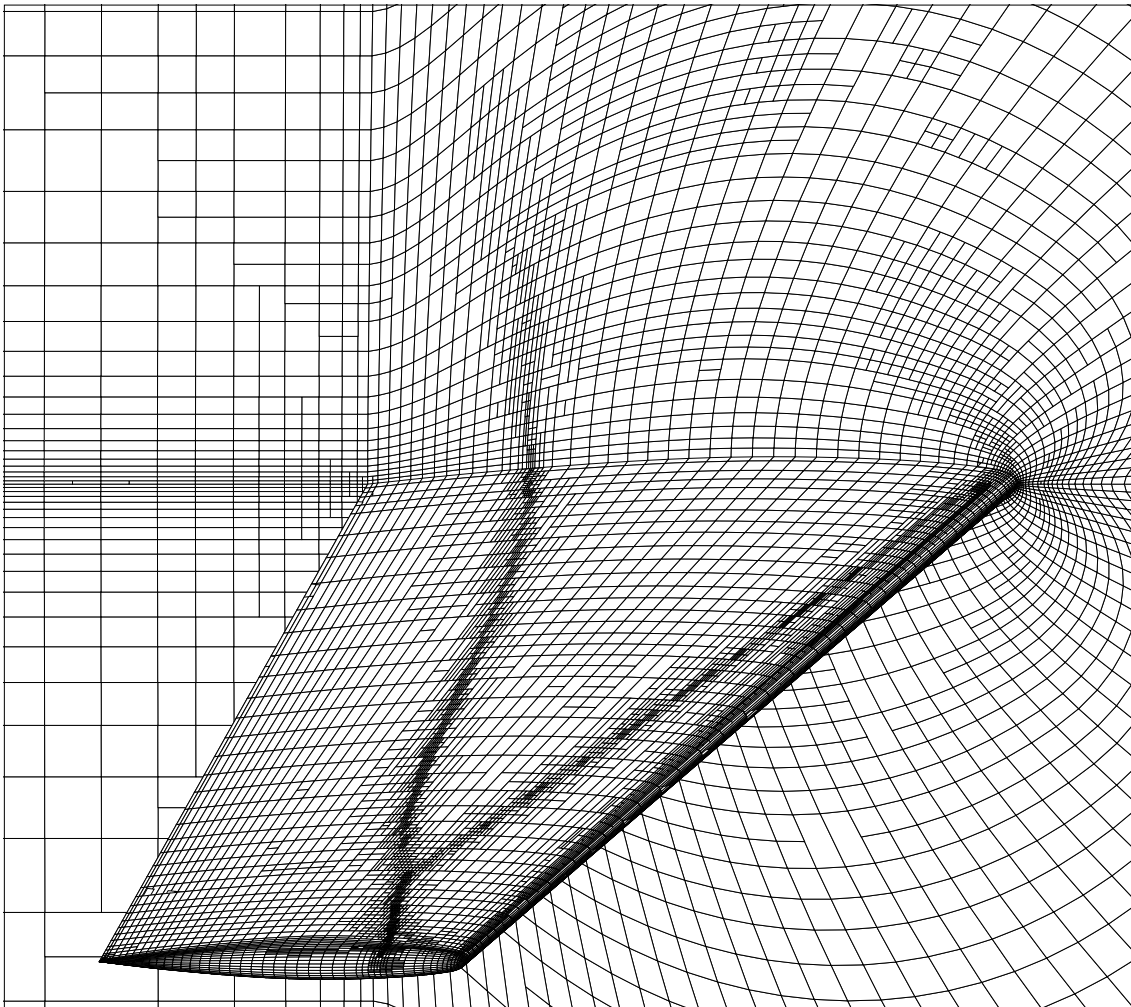


Fig. 18 Adapted mesh on ONERA M6 wing.

4.4 Steady transonic flow

In order to demonstrate the shock-capturing capabilities of the present DG method, transonic flow around the ONERA M6 wing has been computed. The ONERA M6 wing has a trapezoidal plan-form with 30° leading edge sweep and a taper ratio of 0.56. The wing sections are based on the symmetrical ONERA-D profile with 5% thickness/chord ratio. The wing tip is rounded by rotating the tip section around its symmetry axis. The free stream Mach number is 0.84 and the angle of attack is 3.06° . Calculations are performed on two meshes, a mesh of 440,000 cells (Mesh 1) and an adaptively refined mesh with a different mesh topology (Mesh 2). In Figure 15 the pressure distribution at the cross sections at 65% span and at 90% span in Mesh 1 are compared with experiments. The pressure coefficient is defined as $C_p = (p - p_\infty) / \frac{1}{2} \rho V_\infty^2$, with p_∞ and V_∞ the freestream pressure and velocity, respectively. The pressure distribution on the wing and at the symmetry plane is shown in Fig. 16 and shows that the two shocks merge at 87% span and separate at approximately 94% span. Considering the fact that in the simulations the flow is considered to be inviscid, the agreement is good.

The same computations are also performed on the adapted locally refined Mesh 2. The grid adaptation was started by first calculating a steady solution on the initial grid, which consists of 131072 elements. The grid is subsequently adapted three times, independently in all three directions and the final grid consists of 339226 elements. This adaptation process is completely controlled by the adaptation sensor. The only user interaction is the specification of the increase in number of elements during each adaptation step, which is done before the simulation started.

The pressure coefficients at 65% span and at 90% span are shown for the various adapted meshes in Figure 17. The adaptation process clearly improves the sharpness of the captured shocks. Fig. 18 shows the final adapted grid which clearly shows the lambda shock structure. The mesh adapts to regions with large flow activity and significantly improves resolution in the shock regions and around the tip. For efficient adaptation it proved to very important to be able to both add and delete elements, because initially the grid is primarily refined in the stagnation and rear shock regions which tend to become overresolved in the initial adaptation stages. The position of the shocks also significantly changes during the adaptation process when the flow field becomes better resolved. The shock sensor is, however, qualitative and further improvements in sensor functions based on some estimate of the numerical error will contribute to improved efficiency in the grid adaptation process.

4.5 Oscillating NACA 0012 airfoil in transonic flow

The performance of the space-time discretization and mesh adaptation algorithm on unsteady transonic flows has been investigated with the simulation of the flow field about an oscillating NACA

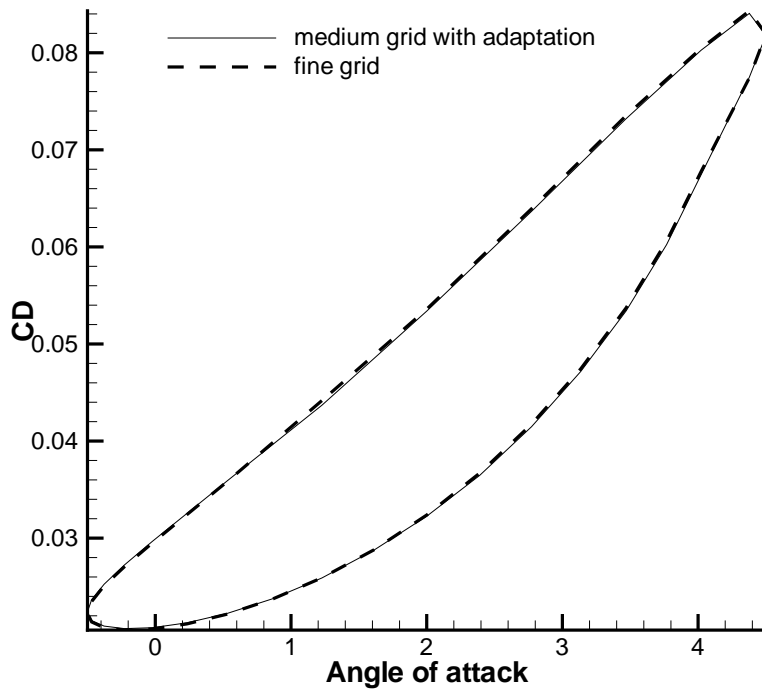
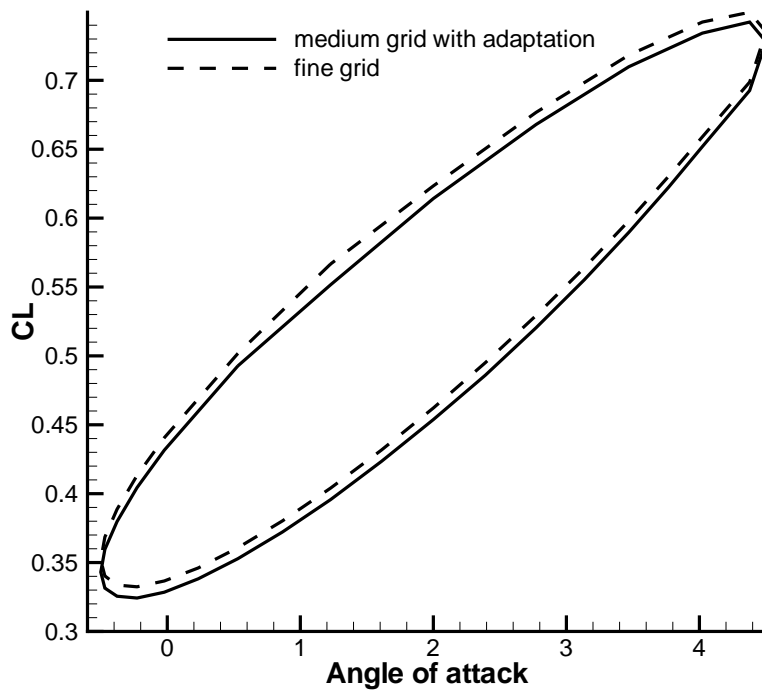


Fig. 19 Lift and drag coefficient on oscillating NACA 0012 airfoil ($M_\infty = 0.8, \omega = \pi/10$).

0012 airfoil. The freestream Mach number is 0.8, the pitching angle ranges between -0.5 and 4.5 degrees and the oscillation period is $T = 20$ (normalized with L/a_∞ , where L is the chord length and a_∞ is the freestream speed of sound), which results in a circular frequency $\omega = \pi/10$. The flow field is computed both on a fine mesh with 32,768 elements and an adapted mesh, which has approximately 9,400 elements during the simulation. During each time step the coarse mesh is adapted, with first coarsening followed by refinement. Both simulations used a time step of 1.0 for the interval $[3.0, 13.0]$ of a period, and a time step of 0.5 in the remaining part of the period. The smaller time steps during this part of the oscillation period are necessary since the shock at the lower side of the airfoil has a greater velocity than the shock at the upper side. If the shock moves through several cells during a time step this will result in numerical oscillations, since no artificial dissipation or limiting is applied in the time direction. In Figure 19 the hysteresis curves of the lift and drag force coefficients C_L and C_D are shown. The results on the fine and adapted mesh are nearly identical, where the difference in the lift coefficient can be attributed to the improved accuracy in the shock due to the mesh adaptation. This can be inferred from the pressure coefficients C_p at the wing shown in Figures 20 to 22. The pressure coefficients for the fine and adapted mesh are nearly identical, except in the shock, where the adapted mesh captures the discontinuity better. The physical interpretation of the flow phenomena shown in Figure 22 at time $t = 42.5$ which appear at the lower side of the airfoil when the shock disappears, is not clear. Even though smaller time steps are used in the corresponding time interval, it may be numerical oscillations caused by insufficient time resolution to capture the motion of the shock. This would be consistent with the fact that the adapted mesh and fine mesh flow results predict the same phenomena, since equal time steps are used.

The Figures 20 to 22 also show that the mesh adaptation does not negatively influence the time accuracy and is very efficient in capturing the flow discontinuities, also for the weak shock at the lower side of the wing which periodically disappears.

4.6 First torsion mode of the AGARD 445.6 wing

Transonic flow at a freestream Mach number of 0.96 is simulated over the deforming AGARD 445.6 wing. The geometry deformation corresponds to the first torsion mode of the wing. The grid point displacements are only in the z -direction, and the average displacement is zero. Views of the normally flat wing at the two extreme positions are shown in Figure 23. Maximum displacement occurs at the tip and is of the order of 10% root chord. The normalized frequency of the torsion mode is 0.192, normalized with L/a_∞ , where L is the root chord and a_∞ is the freestream speed of sound. The wing deformations are accommodated by the grid using a standard grid deformation algorithm to move the grid points. The deformation algorithm essentially solves a Laplace



equation for the grid point displacements (see Masud and Hughes (Ref. 33)). The grid contains 73,728 grid points. The time period is subdivided into 20 uniform time steps, which are chosen such that the movement of the shock is captured accurately. Per time step the L_2 -residual for the cell averages is reduced to the level of 10^{-5} , which required 150 multigrid cycles on average. Part of the convergence histories are shown in Figure 24. Including postprocessing, the simulation of a period required 15,000 seconds on a single processor NEC SX-5 at a speed of 3.5 Gflop/s. The Mach number distribution on the upper side of the wing and in the symmetry plane at $t = \frac{7}{20}T$, where T is the period of the torsion mode, is shown in Figure 25. The pressure coefficient C_p at 88% span is shown in Figure 26. Also shown is the shape of the cross section geometry. The pressure coefficient shows strong variations during the oscillation cycle and a rapidly moving and oscillating shock is captured without numerical oscillations. The results clearly demonstrate the maturity of the discontinuous Galerkin method. Efficient simulation of the three-dimensional unsteady flow over a deforming wing is possible using the space-time discontinuous Galerkin finite element method described in these notes.

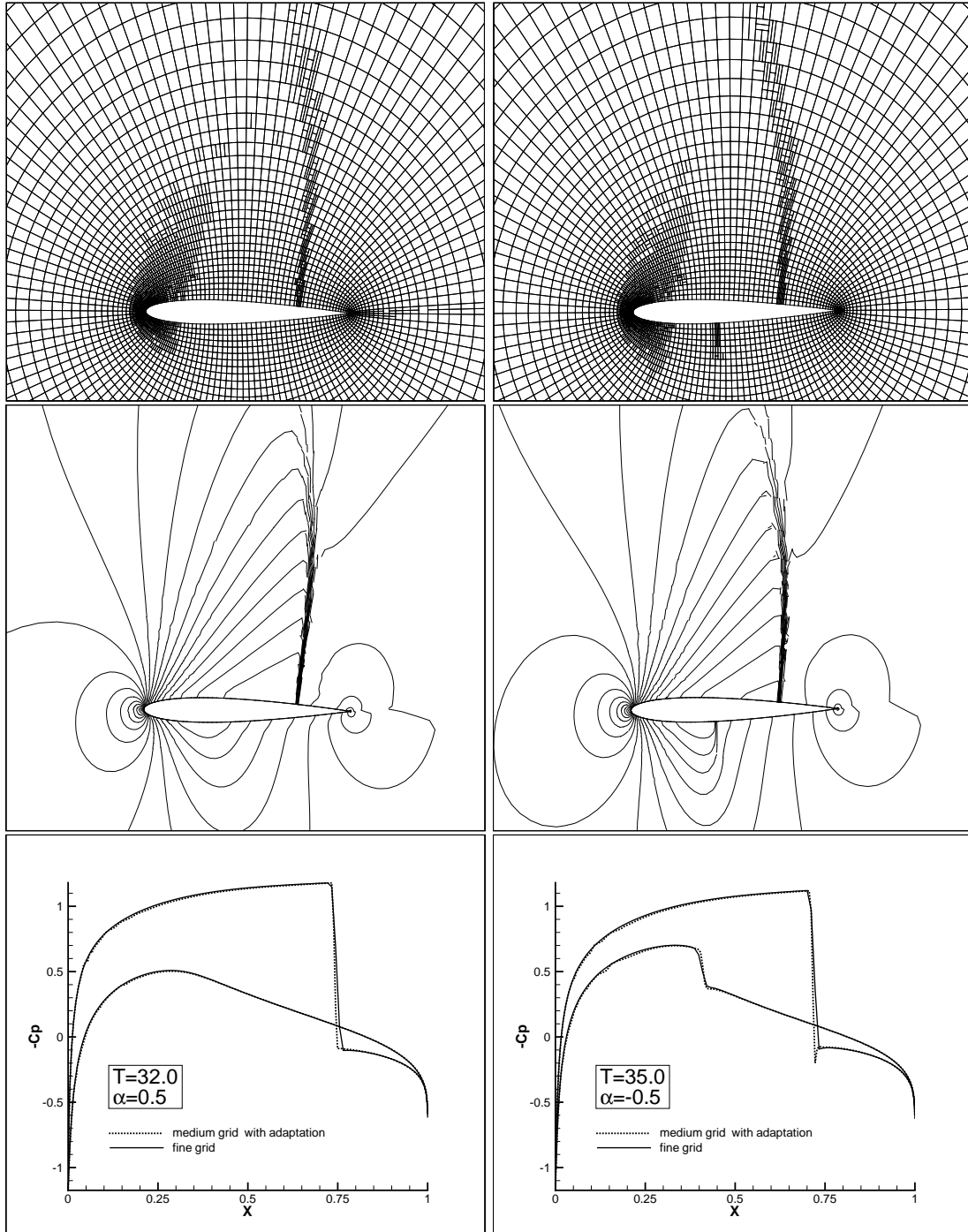


Fig. 20 Adapted mesh around oscillating NACA 0012 airfoil, contours of density, and pressure coefficient C_p on the airfoil surface for $\alpha = 0.5^\circ$ (pitching downward) and $\alpha = -0.5^\circ$ ($M_\infty = 0.8$, $\omega = \pi/10$).

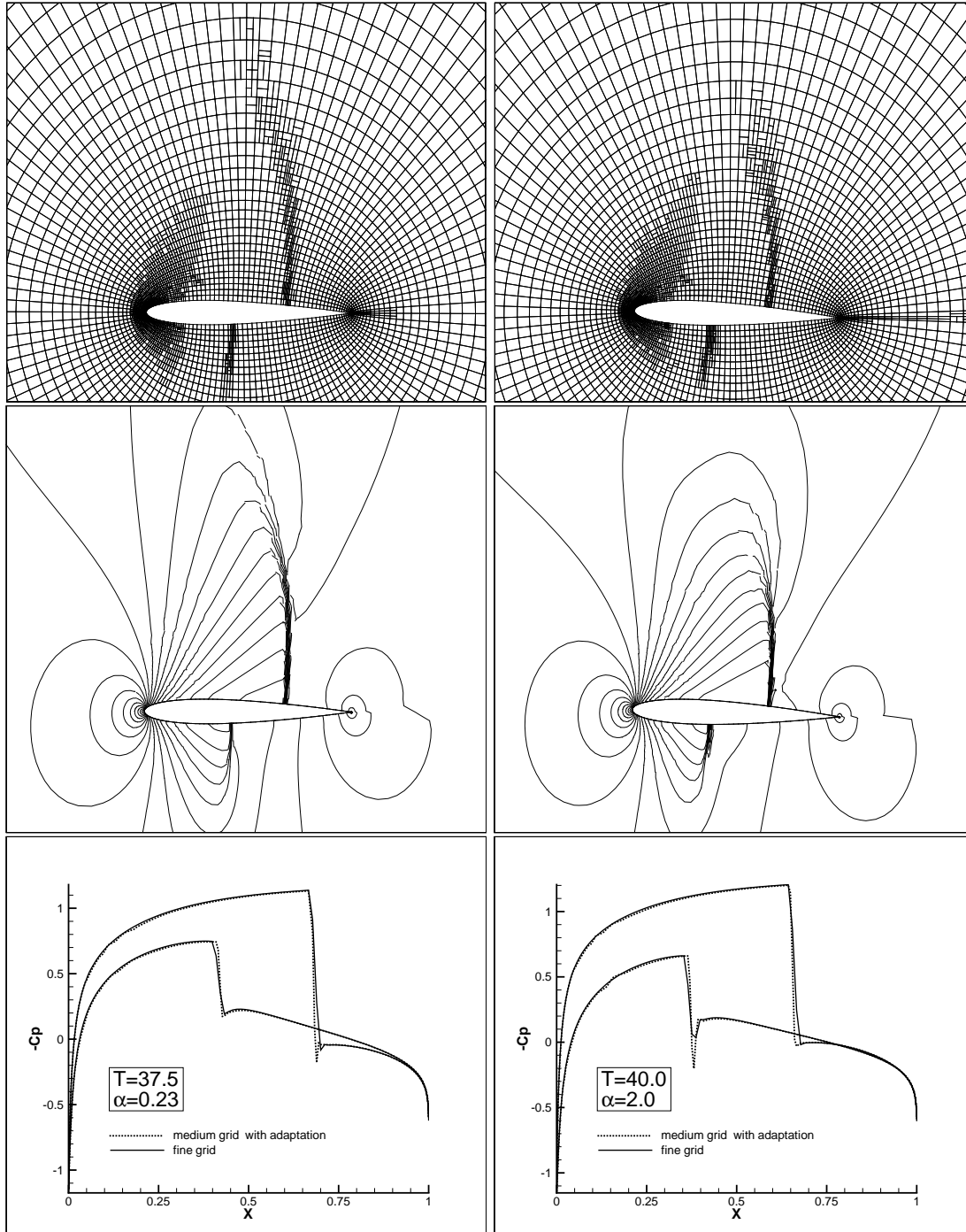


Fig. 21 Adapted mesh around oscillating NACA 0012 airfoil, contours of density, and pressure coefficient C_p on the airfoil surface for $\alpha = 0.23^\circ$ (pitching upward) and $\alpha = 2.0^\circ$ (pitching upward) ($M_\infty = 0.8$, $\omega = \pi/10$).

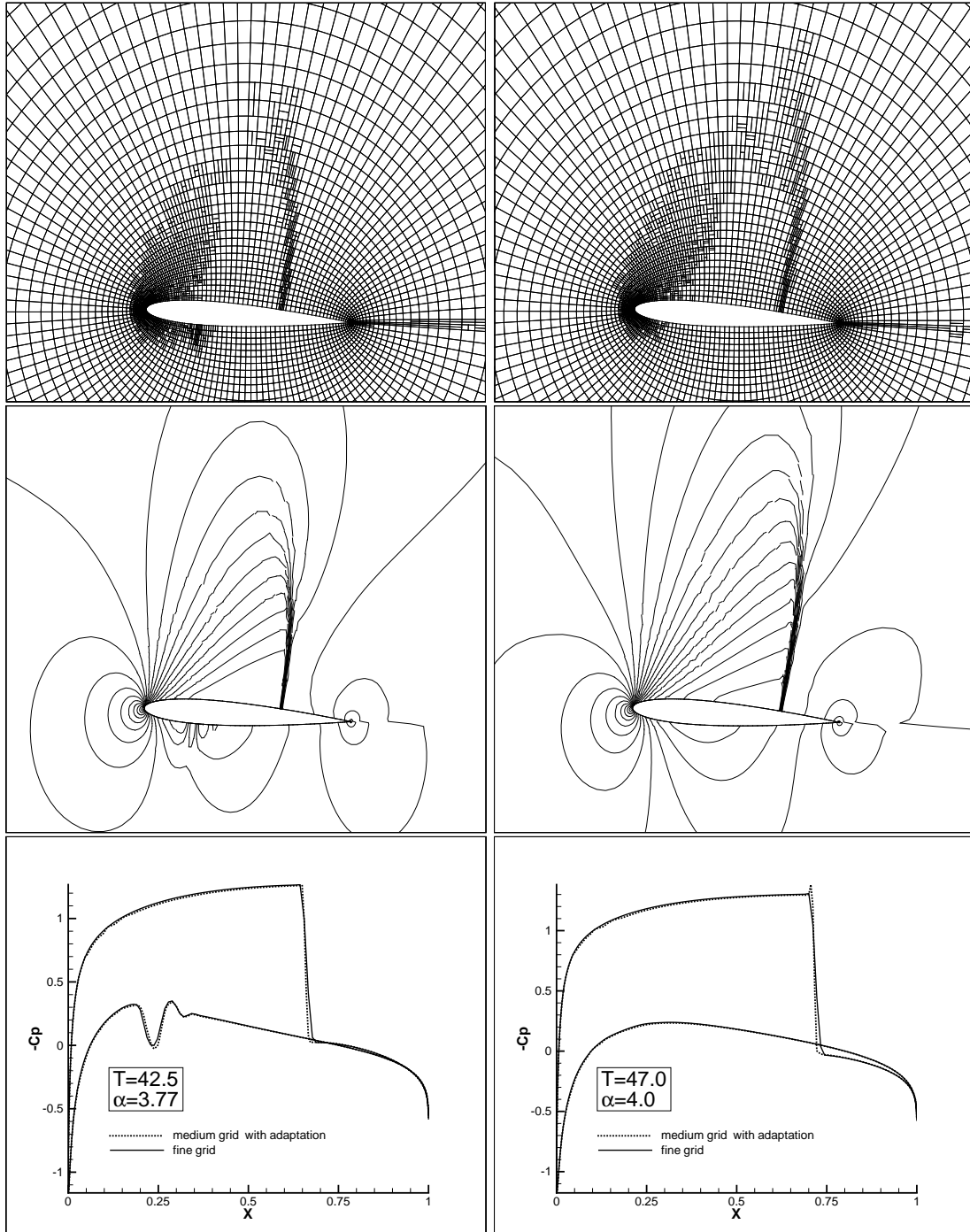


Fig. 22 Adapted mesh around oscillating NACA0012 airfoil, contours of density, and pressure coefficient C_p on the airfoil surface for $\alpha = 3.77^\circ$ (pitching upward) and $\alpha = 4.0^\circ$ (pitching downward) ($M_\infty = 0.8$, $\omega = \pi/10$).

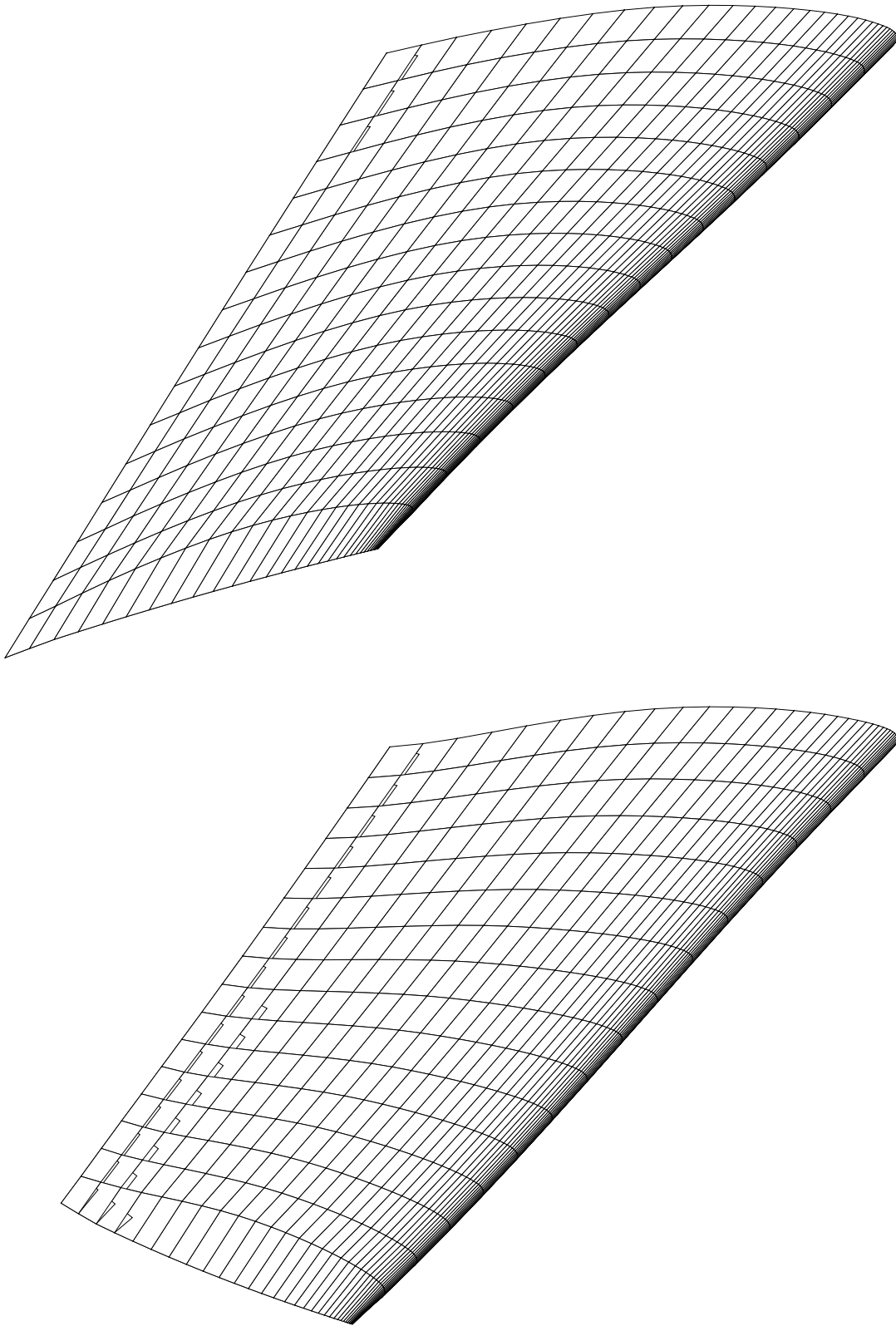


Fig. 23 Wing deformation at the two extreme positions. The vertical coordinate is multiplied with a factor 5, to make the deformation visible. The flow comes from the right.

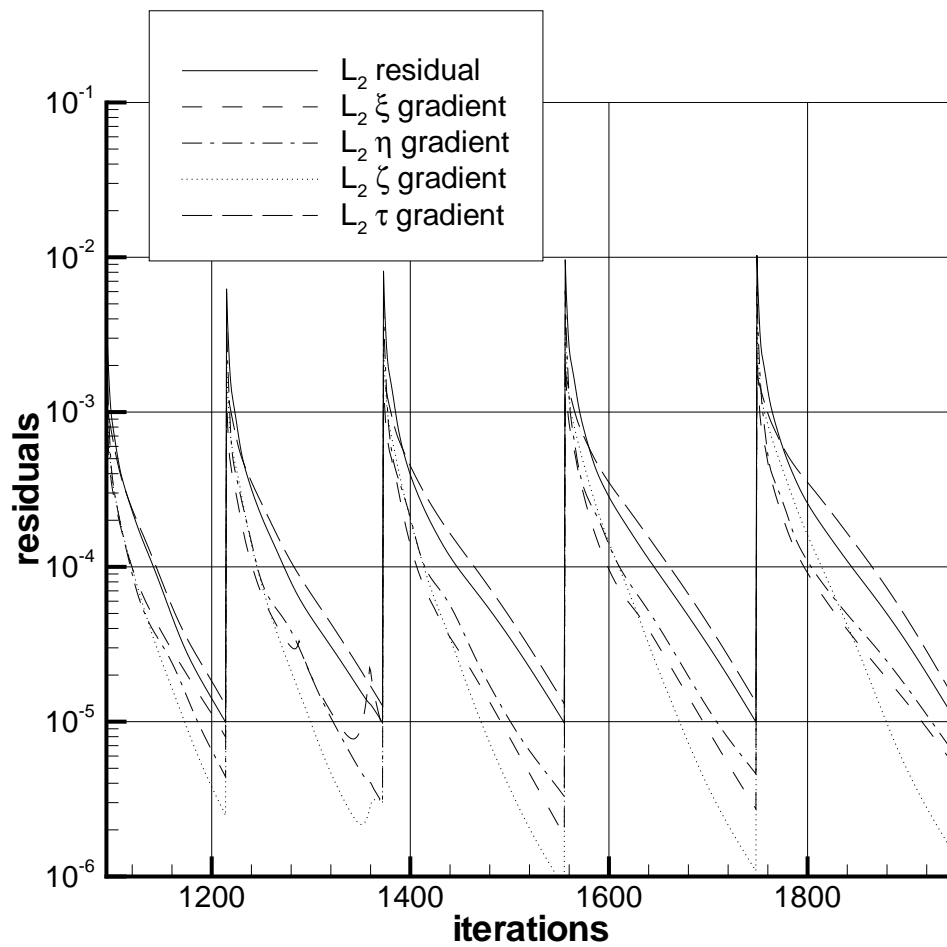


Fig. 24 Convergence history for five time steps of the simulation of the first torsion mode of the AGARD 445.6 wing

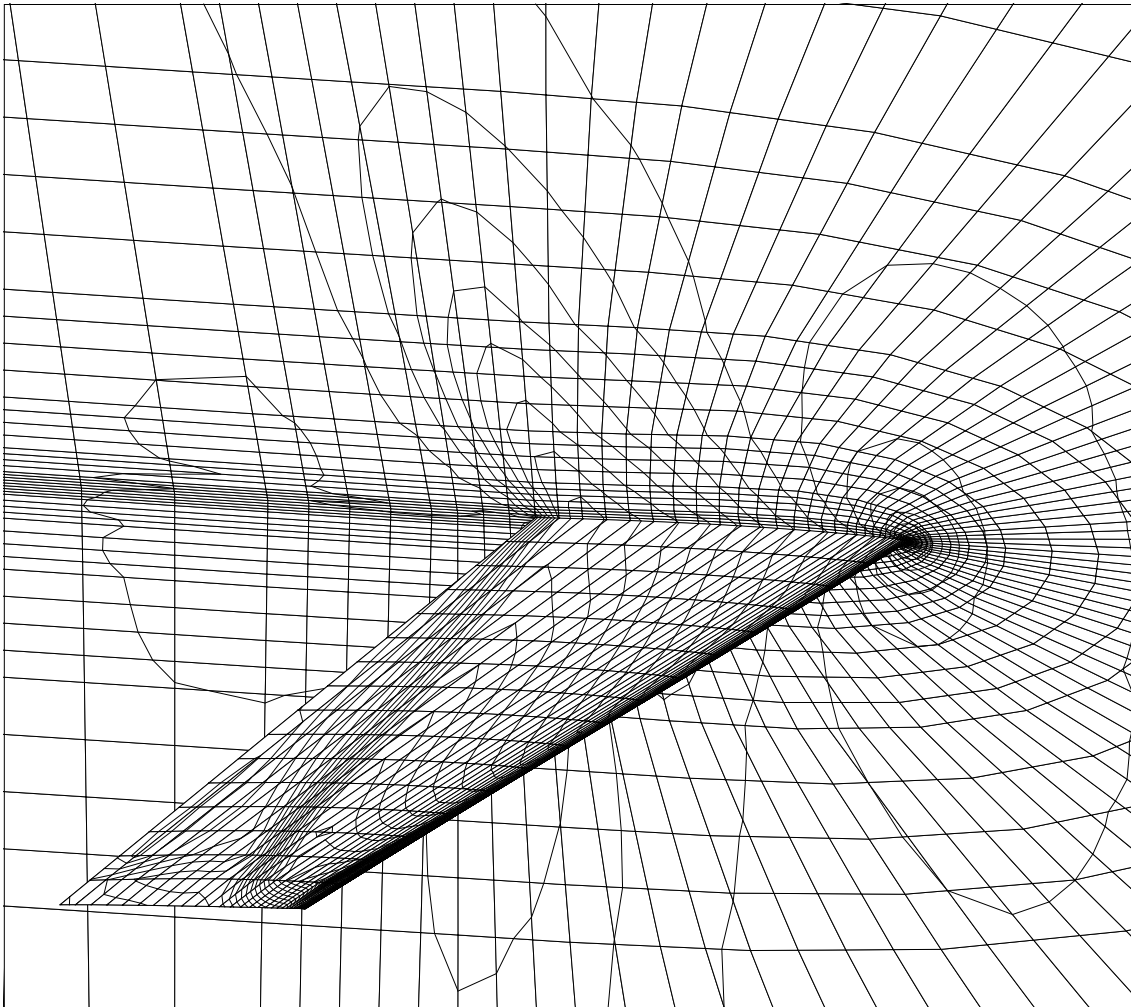


Fig. 25 Mach number contours on wing and symmetry plane at time $t = \frac{7}{20}T$, where T is the period of the torsion mode.

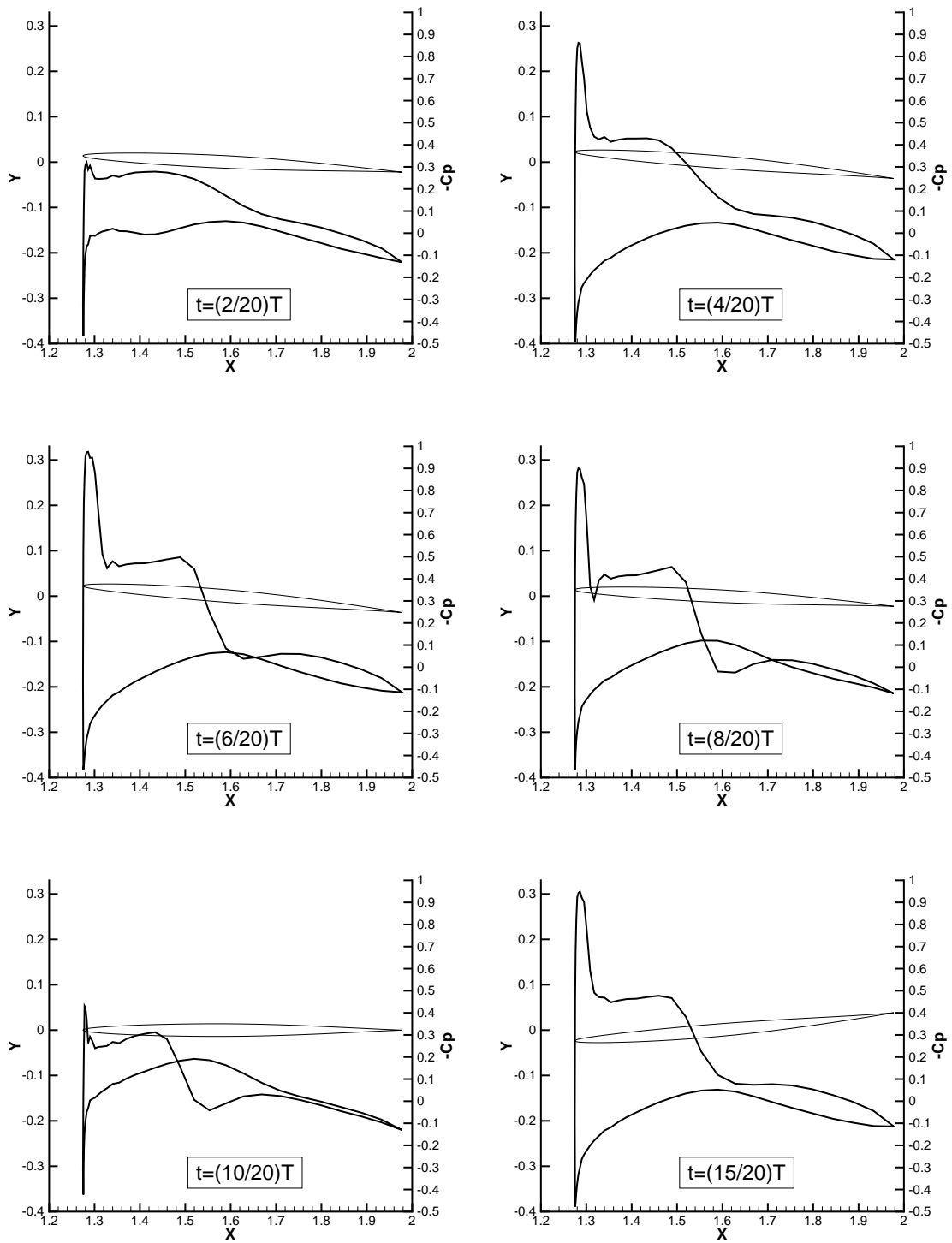


Fig. 26 C_p -distributions at a cross section at 88% span



5 Concluding Remarks

In these notes we have presented a new space-time discontinuous Galerkin finite element method for the time-accurate solution of inviscid compressible flows on dynamic, hexahedron type meshes. The accuracy is improved using local mesh refinement and we have presented an efficient pseudo-time integration technique with multigrid convergence acceleration to solve the non-linear equations for the expansion coefficients in the DG discretization.

In order to improve the computational efficiency of the space-time discontinuous Galerkin method a new quadrature rule for the face flux and volume integrals arising in the discontinuous Galerkin discretization of the Euler equations is presented and analyzed. The new quadrature rule expands the flux in a Taylor series and uses the gradient expansion coefficients, which are readily available in the DG method, to compute the flux integrals. This makes the Taylor quadrature rule very natural and highly efficient within the DG framework. A speedup of three has been obtained when comparing the computing times for the Taylor quadrature rule with the computing times for the standard Gauss quadrature rule. Moreover, this gain in efficiency comes without any loss in accuracy. Both numerical experiments and theoretical analysis showed that the new Taylor quadrature rule yields a second order accurate local truncation error for linear basis functions, just as the conventional Gauss quadrature rule does.

The space-time DG method has been demonstrated to combine well with local mesh refinement in various simulations and maintains accuracy on non-smooth meshes. This makes the space-time DG method an interesting technique for complex aerodynamic and aeroelastic problems. The space-time discontinuous Galerkin discretization of the Euler equations combined with the Taylor quadrature rule has successfully been applied to the simulation of unsteady transonic flow over a deforming wing and oscillating airfoils. Application of the method to helicopter rotor flows are presented elsewhere (Boelens et al. (Ref. 8) and Ven der Ven et al. (Ref. 50), the latter demonstrating four-dimensional grid adaptation in both space and time). These applications demonstrate the maturity of the discontinuous Galerkin method.

6 Acknowledgments

The first author is supported in part by a research grant from the Netherlands National Aerospace Laboratory.

The advice and continued support by Dr. B. Oskam (NLR) during the course of this project is greatly appreciated, especially his essential contributions to the development of the artificial dissipation operator. Sincere thanks are also due to O.J. Boelens (NLR) for conducting many simulations with the program HEXADAP which significantly contributed to the validation and improvements of the numerical scheme. We also thank Y. Stalder (UT) for the assistance with the stability analysis of the Runge-Kutta scheme and the testing of the HLLC scheme, and J.J. Sudirham (UT) for conducting the accuracy tests.

These notes are an adaptation of:

1. J.J.W. van der Vegt and H. van der Ven, Space-time discontinuous Galerkin finite element method with dynamic grid motion for inviscid compressible flows. I. General formulation, *Journal of Computational Physics*, 182, pp. 546-585 (2002).
2. H. van der Ven and J.J.W. van der Vegt, Space-time discontinuous Galerkin finite element method with dynamic grid motion for inviscid compressible flows. II. Efficient flux quadrature, *Computer Methods in Applied Mechanics and Engineering*, 191, pp. 4747-4780 (2002).



7 References

1. R.A. Adams, Sobolev spaces, Academic Press (1975).
2. H.L. Atkins and C.W. Shu, Quadrature-free implementation of discontinuous Galerkin method for hyperbolic equations, *AIAA J.* **36**(5), 775-782 (1997).
3. T.J. Barth, Numerical methods for gasdynamic systems on unstructured meshes. in Kröner, Ohlberger and Rohde (Eds.), *Lect. Notes in Comp. Sci. and Eng.* **5**, 195-285 (Springer-Verlag, 1998).
4. F. Bassi and S. Rebay, High-order accurate discontinuous finite element solution of the 2D Euler equations, *J. Comput. Phys.* **138**, 251-285 (1997)
5. P. Batten, N. Clarke, C. Lambert and D. Causon, On the choice of wave speeds for the HLLC Riemann solver, *SIAM J. Sci. and Stat. Comp.* **18**, 1553-1570 (1997).
6. P. Batten and M.A. Leschziner and U.C. Goldberg, Average-state Jacobians and implicit methods for compressible viscous and turbulent flows", *J. Comput. Phys.* **137**, 38-78 (1997)
7. C.E. Baumann, An hp-adaptive discontinuous finite element method for computational fluid dynamics, Ph.D. dissertation, The University of Texas at Austin, Aug. 1997.
8. O.J. Boelens, H. van der Ven, B. Oskam and A.A. Hassan, The boundary conforming discontinuous Galerkin finite element approach for rotorcraft simulations, *J. of Aircraft* **39**(5), 776-785 (2002)
9. C.L. Bottasso, On the computation of the boundary integral of space-time deforming finite elements, *Comm. in Numer. Meth. in Engrg.* **13**, 53-59 (1997).
10. J.H. Bramble and S.R. Hilbert, Bounds for a class of linear functionals with applications to Hermite interpolation, *Numer. Math* **16**, 362-369, (1971).
11. S.C. Brenner and L.R. Scott, The mathematical theory of finite element methods, Springer Verlag (1996).
12. A. Burbeau, P. Sagaut and Ch.-H. Bruneau, A problem-independent limiter for high-order Runge-Kutta discontinuous Galerkin methods, *J. Comput. Phys.* **169**, 111-150 (2001).
13. P.G. Ciarlet, The finite element method for elliptic problems, North-Holland (1978).
14. B. Cockburn and P.A. Gremaud, Error estimates for finite element methods for nonlinear conservation laws, *SIAM J. Numer. Anal.* **33**, 522-554 (1996).
15. B. Cockburn and C.-W. Shu, TVB Runge-Kutta local projection discontinuous Galerkin finite element method for conservation laws II: General framework, *Math. Comp.* **52**, 411-435 (1989).
16. B. Cockburn, S. Hou and C.-W. Shu, The Runge-Kutta local projection discontinuous Galerkin finite element method for conservation laws IV: The multidimensional case, *Math. Comp.* **54**, 545-581 (1990).

17. B. Cockburn and C.-W. Shu, The Runge-Kutta discontinuous Galerkin method for conservation laws V, *J. Comput. Phys.* **141**, 199-224 (1998).
18. B. Cockburn, Discontinuous Galerkin methods for convection-dominated problems, in T.J. Barth and H. Deconinck (Eds.), *Lect. Notes in Comp. Sci. and Eng.* **9** (Springer Verlag, 1999).
19. B. Cockburn, G.E. Karniadakis, C.-W. Shu, (Eds.), Discontinuous Galerkin methods. Theory, computation and applications, *Lect. Notes in Comp. Sci. and Eng.* **11** (Springer Verlag, 2000).
20. S.F. Davis, Simplified second-order Godunov-type methods, *SIAM J. Sci. Stat. Comput.* **9**, 445-473 (1988).
21. M. Giles and E. Süli, Adjoint methods for PDEs: a posteriori error analysis and postprocessing by duality. *Acta Numerica 2002*, 145-236 (Cambridge University Press, 2002).
22. J. Gopalakrishnan and G. Kanschat, A multilevel discontinuous Galerkin method. IMA Preprint Nr. 1735, 2000, <http://www.ima.umn.edu/preprints/dec2000/1735.pdf>. To appear in *Num. Math.*
23. P. Grisvard, Elliptic problems in nonsmooth domains, Pitman (1985).
24. H. Guillard and C. Farhat, On the significance of the GCL for flow computations on moving meshes, AIAA Paper 99-0793, 37th Aerospace Sciences Meeting and Exhibit, Reno, Nevada (1999).
25. P. Hansbo, Aspects of conservation in finite element flow computations, *Comput. Meth. Appl. Mech. Engrg.* **117**, 423-437 (1994).
26. J. Jaffre, C. Johnson and A. Szepessy, Convergence of the discontinuous Galerkin finite element method for hyperbolic conservation laws, *Math. Models and Meth. in Appl. Sci.* **5**, 367-386 (1995).
27. D.S. Kershaw, M.K. Prasad, M.J. Shaw and J.L. Milovich, 3D Unstructured mesh ALE hydrodynamics with the upwind discontinuous finite element method, *Comput. Meth. Appl. Mech. Engrg.* **158**, 81-116 (1998).
28. P.M. Knupp, On the invertibility of the isoparametric map, *Comput. Methods Appl. Mechanics and Engineering* **78** (1990), 313-329.
29. M. Lesoinne and C. Farhat, Geometric conservation laws for flow problems with moving boundaries and deformable meshes, and their impact on aeroelastic computations, *Comput. Meth. Appl. Mech. Engrg.* **134**, 71-90 (1996).
30. J.-L. Lions, Sur les espaces d'interpolation; Dualité, *Math. Scand.* **9**, 147-177, (1961).
31. D.P. Lockard and H.L. Atkins, Efficient implementations of the quadrature-free discontinuous Galerkin method, *AIAA J.* 99-3309, (1999).
32. R.B. Lowrie, P.L. Roe, B. van Leer, Space-time methods for hyperbolic conservation laws, in *Barriers and Challenges in Computational Field Dynamics*, V. Venkatakrishnan et al. (Eds.), 79 (1998).

33. A. Masud and T.J.R. Hughes, A space-time Galerkin/least squares finite element formulation of the Navier-Stokes equations for moving domain problems, *Comput. Meth. Appl. Mech. Engrg.* **146**, 91-126, (1997).
34. N.D. Melson, M.D. Sanetrik and H.L. Atkins, Time-accurate Navier-Stokes calculations with multigrid acceleration, in *Proc. 6th Copper Mountain Confer. on Multigrid Methods* (1993).
35. S.M. Nikol'skii, On imbedding, continuation and approximation theorems for differentiable functions of several variables, *Russian Mat. Surveys* **16**, 55-104 (1961).
36. Ch. Schwab, *hp*-FEM for fluid flow simulation, in T.J. Barth and H. Deconinck (Eds.), *Lect. Notes in Comp. Sci. and Eng.* **9** (Springer Verlag, 1999).
37. F. Shakib, T.J.R. Hughes and Z. Johan, A new finite element method for computational fluid dynamics: X. The compressible Euler and Navier-Stokes equations, *Comput. Meth. Appl. Mech. Engrg.* **89**, 141-219 (1991).
38. A.H. Stroud, *Approximate Calculation of Multiple Integrals* (Prentice-Hall, Englewood Cliffs, NJ, 1971).
39. P.D. Thomas and C.K. Lombard, Geometric conservation law and its application to flow computations on moving grids, *AIAA J.* **17**, 1030-1037 (1979).
40. E.F. Toro, M. Spruce and W. Speares, Restoration of the contact surface in the HLL-Riemann solver, *Shock Waves* **4**, 25-34 (1994).
41. E.F. Toro, *Riemann solvers and numerical methods for fluid dynamics. A practical introduction* 2nd edition (Springer Verlag, 1999).
42. H. Triebel, *Interpolation theory, function spaces, differential operators*, North-Holland, (1978).
43. J.J.W. van der Vegt and H. van der Ven, Discontinuous Galerkin finite element method with anisotropic local grid refinement for inviscid compressible flows, *J. Comput. Phys.* **141**, 46-77 (1998).
44. J.J.W. van der Vegt, H. van der Ven, and O.J. Boelens, Discontinuous Galerkin finite element methods for hyperbolic partial differential equations, in *Godunov Methods: Theory and Applications*, Edited by E.F. Toro, Kluwer Academic/Plenum Publishers, New York and London, pp. 985-1006, (2001),
45. J.J.W. van der Vegt and H. van der Ven, Space-time discontinuous Galerkin finite element method with dynamic grid motion for inviscid compressible flows. Part I. General formulation., *J. Comput. Phys.* **182**, 546-585 (2002).
46. J.J.W. van der Vegt and H. van der Ven, Slip boundary conditions in discontinuous Galerkin discretizations of the Euler equations of gas dynamics, in *Proceedings Fifth World Congress on Computational Mechanics*, July 7-12, Vienna, <http://wccm.tuwien.ac.at/>, eds. H.A. Mang, F.G. Rammerstorfer and J. Eberhardsteiner (2002).

47. J.J.W. van der Vegt, Geometric conditions on the invertibility and interpolation error of isoparametric hexahedral space-time elements”, in preparation.
48. H. van der Ven and J.J.W. van der Vegt, Accuracy, resolution, and computational complexity of a discontinuous Galerkin finite element method, *Lect. Notes in Comp. Sci. and Eng.* **11**, 439-444, Springer Verlag, Berlin (2000).
49. H. van der Ven and J.J.W. van der Vegt, Space-time discontinuous Galerkin finite element method with dynamic grid motion for inviscid compressible flows. II. Efficient flux quadrature, *Comput. Meth. Appl. Mech. Engrg.* **191**, pp. 4747-4780 (2002).
50. H. van der Ven and O.J. Boelens, Towards affordable CFD simulations of rotors in forward flight, A feasibility study with future application to vibrational analysis, in *Proceedings of the 59th American Helicopter Society Forum*, May 6-8, Phoenix, Arizona, NLR-TP-2003-100, (2003).



This page is intentionally left blank.

Appendices

A Sobolev spaces

- A domain Ω has the cone property if there exists a finite cone C such that each point $x \in \Omega$ is the vertex of a finite cone C_x contained in Ω , which is obtained by rigid motion from C and is congruent to C , Adams (Ref. 1).
- Define the standard Sobolev space $W^{m,p}(\Omega)$, with $m \in \mathbb{Z}$, $m \geq 0$, $1 \leq p \leq \infty$, and $\Omega \subseteq \mathbb{R}^n$, as:

$$W^{m,p}(\Omega) := \{v \in L^1_{loc}(\Omega) \mid \|v\|_{m,p,\Omega} < \infty\}.$$

Here $L^1_{loc}(\Omega)$ denotes the space of locally integrable functions:

$$L^1_{loc}(\Omega) := \{v \mid v \in L^1(K), \forall \text{ compact } K \subset \text{interior } \Omega\},$$

and $L^1(K)$ the space of Lebesgue integrable functions on K . The Sobolev norm $\|v\|_{m,p,\Omega}$ is defined as:

$$\|v\|_{m,p,\Omega} := \left(\sum_{|\alpha| \leq m} \int_{\Omega} |D^{\alpha}v|^p dx \right)^{1/p}, \quad \text{if } 1 \leq p < \infty,$$

$$\|v\|_{m,p,\Omega} := \max_{|\alpha| \leq m} \left(\text{ess sup}_{x \in \Omega} |D^{\alpha}v(x)| \right), \quad \text{if } p = \infty,$$

and the semi-norms $|v|_{m,p,\Omega}$ and $[v]_{m,p,\Omega}$ are for $1 \leq p < \infty$ defined as:

$$|v|_{m,p,\Omega} := \left(\sum_{|\alpha|=m} \int_{\Omega} |D^{\alpha}v|^p dx \right)^{1/p},$$

$$[v]_{m,p,\Omega} := \left(\sum_{k=0}^n \int_{\Omega} \left| \frac{\partial^m v}{\partial x_k^m} \right|^p dx \right)^{1/p},$$

with α the multi-index symbol, and the usual modification for $p = \infty$. The derivatives in the (semi)-norms have to be considered as weak derivatives.

- For a bounded or unbounded open domain $\Omega \subseteq \mathbb{R}^n$ with the cone property the Sobolev space $W^{s,p}(\Omega)$, with $s \in \mathbb{R}$, $s \geq 0$, $1 \leq p \leq \infty$, is defined as: $W^{s,p}(\Omega) = W^{m,p}(\Omega)$ when $s = m$ is a non-negative integer, and for noninteger s as the subspace of $W^{m,p}(\Omega)$ with a finite Sobolev-Slobodečkij norm:

$$\|v\|_{s,p,\Omega} := \left(\|v\|_{m,p,\Omega}^p + \sum_{|\alpha|=m} \int_{\Omega} \int_{\Omega} \frac{|D^{\alpha}v(x) - D^{\alpha}v(y)|^p}{|x-y|^{m+\sigma p}} dx dy \right)^{1/p}, \quad 1 \leq p < \infty$$

$$\|v\|_{s,p,\Omega} := \max \left(\|v\|_{m,\infty,\Omega}, \max_{|\alpha|=m} \text{ess sup}_{x,y \in \Omega, x \neq y} \frac{|D^{\alpha}v(x) - D^{\alpha}v(y)|}{|x-y|^{\sigma}} \right), \quad p = \infty,$$

with m the integer part of s , and $\sigma = s - m$, with $0 < \sigma < 1$. Note, with this definition fractional order Sobolev spaces coincide for s noninteger and $1 < p < \infty$ with the Besov spaces defined in Triebel (Ref. 42), pages 310 and 323 (see also (Ref. 35)), for which extensive imbedding theorems exist.

- Define the broken Sobolev space $W_B^{s,p}(\mathcal{T}_h^n)$, with $s \in \mathbb{R}$, $s \geq 0$ and $1 \leq p \leq \infty$, as:

$$W_B^{s,p}(\mathcal{T}_h^n) := \left\{ v \in L^p(\mathcal{T}_h^n) \mid v|_{\mathcal{K}} \in W^{s,p}(\mathcal{K}_j^n), \forall \mathcal{K}_j^n \in \mathcal{T}_h^n \right\}, \quad (88)$$

with the norm and semi-norms defined as:

$$\begin{aligned} \|v\|_{s,p,\mathcal{T}_h^n} &= \left(\sum_{\mathcal{K} \in \mathcal{T}_h^n} \|v\|_{s,p,\mathcal{K}}^p \right)^{1/p} \\ [v]_{s,p,\mathcal{T}_h^n} &= \left(\sum_{\mathcal{K} \in \mathcal{T}_h^n} |v|_{s,p,\mathcal{K}}^p \right)^{1/p} \\ |[v]|_{s,p,\mathcal{T}_h^n} &= \left(\sum_{\mathcal{K} \in \mathcal{T}_h^n} |v|_{s,p,\partial\mathcal{K}}^p \right)^{1/p}. \end{aligned}$$

- The norms and semi-norms on product spaces are extended naturally. For instance if $v \in \mathbb{R}^n$, $v = (v_1, \dots, v_n)$ then:

$$\|v\|_{m,p,\Omega} = \left(\sum_{i=1}^n \|v_i\|_{m,p,\Omega}^p \right)^{1/p}, \quad \text{if } 1 \leq p < \infty, \quad (89)$$

$$\|v\|_{m,\infty,\Omega} = \max_{1 \leq i \leq n} \|v_i\|_{m,\infty,\Omega}, \quad (90)$$

$$|[v]|_{m,\infty,\Omega} = \max_{1 \leq i \leq n} \sup_{x \in \Omega} \left\| \frac{\partial^m v(x)}{\partial x_i^m} \right\|, \quad (91)$$

with $\|\cdot\|$ the Euclidian norm.

- The product space L_N^p is defined for $1 \leq p < \infty$ as:

$$L_N^p(\Omega) = \prod_{j=1}^N L^p(\Omega),$$

with the associated norm given by (89).

B Some facts from differential geometry

Given a parameterization $F : (-1, 1)^{n-1} \rightarrow S$, where S is curved hypersurface in \mathbb{R}^n , integration over the surface S is defined as:

$$\int_S f(x) dx = \int_{(-1,1)^{n-1}} f(F(\xi)) \left| \frac{\partial F}{\partial \xi_1} \wedge \cdots \wedge \frac{\partial F}{\partial \xi_{n-1}} \right| d\xi,$$

where the outer product $v = w_1 \wedge \cdots \wedge w_{n-1}$, for $n-1$ vectors w_i in \mathbb{R}^n , is defined component-wise by the rule

$$v^j = \det(w_1, \dots, w_{n-1}, e_j),$$

with e_j the j -th basis vector in \mathbb{R}^n . From this formula it is clear that this concept is a generalization of the outer product in \mathbb{R}^3 .

Let \mathcal{S}_m ($1 \leq m \leq 6$) be one of the six space-time faces of the element \mathcal{K} which is parameterized by the map G_K . Let $F_{\mathcal{S}_m}$ be the parameterization of \mathcal{S}_m obtained from the restriction of G_K to the appropriate face of the boundary of $\hat{\mathcal{K}} = (-1, 1)^4$. As computed in Section 2.2.2.2 we have:

$$\frac{\partial F_{\mathcal{S}_m}}{\partial \xi_{m_2}} \wedge \frac{\partial F_{\mathcal{S}_m}}{\partial \xi_{m_3}} \wedge \frac{\partial F_{\mathcal{S}_m}}{\partial \xi_4} = \begin{pmatrix} \frac{1}{2} \Delta t \frac{\partial F_{\mathcal{S}_m(t)}}{\partial \xi_{m_2}} \wedge \frac{\partial F_{\mathcal{S}_m(t)}}{\partial \xi_{m_3}} \\ -\frac{1}{2} \Delta \bar{x} \cdot \left(\frac{\partial F_{\mathcal{S}_m(t)}}{\partial \xi_{m_2}} \wedge \frac{\partial F_{\mathcal{S}_m(t)}}{\partial \xi_{m_3}} \right) \end{pmatrix}, \quad (92)$$

where the outer product on the right hand side is the usual outer product in \mathbb{R}^3 and $\Delta \bar{x} = F_K^{n+1}(\bar{\xi}) - F_K^n(\bar{\xi})$. The parameterization $F_{\mathcal{S}_m(t)}$ of the space face $S_m(t)$ at time t is obtained by a further restriction of F_S to a constant computational time coordinate. Note that $\frac{\partial F_{\mathcal{S}_m(t)}}{\partial \xi_{m_2}} \wedge \frac{\partial F_{\mathcal{S}_m(t)}}{\partial \xi_{m_3}}$ is aligned with the space normal of $S_m(t) \subset \partial K(t) \subset \mathbb{R}^3$. By construction the outer product is aligned with the space-time normal n of \mathcal{S}_m :

$$n = s \frac{\frac{\partial F_S}{\partial \xi_{m_2}} \wedge \frac{\partial F_S}{\partial \xi_{m_3}} \wedge \frac{\partial F_S}{\partial \xi_4}}{\left| \frac{\partial F_S}{\partial \xi_{m_2}} \wedge \frac{\partial F_S}{\partial \xi_{m_3}} \wedge \frac{\partial F_S}{\partial \xi_4} \right|},$$

where $s = \pm 1$ is such that the normal is outward pointing. By definition,

$$\int_{\mathcal{S}_m} f n dx = s \int_{\hat{\mathcal{S}}} f \frac{\partial F_{\mathcal{S}_m}}{\partial \xi_{m_2}} \wedge \frac{\partial F_{\mathcal{S}_m}}{\partial \xi_{m_3}} \wedge \frac{\partial F_{\mathcal{S}_m}}{\partial \xi_4} d\xi_{m_2} d\xi_{m_3} d\xi_4, \quad (93)$$

hence the \mathbb{R}^4 -valued measure $d\hat{\mathcal{S}}^m$, $1 \leq m \leq 6$, is defined as:

$$d\hat{\mathcal{S}}^m = s \frac{\partial F_{\mathcal{S}_m}}{\partial \xi_{m_2}} \wedge \frac{\partial F_{\mathcal{S}_m}}{\partial \xi_{m_3}} \wedge \frac{\partial F_{\mathcal{S}_m}}{\partial \xi_4} d\xi_{m_2} d\xi_{m_3} d\xi_4.$$

Define the \mathbb{R}^3 -valued measure $d\bar{\mathcal{S}}^m$ on $\hat{\mathcal{S}}$ by:

$$d\bar{\mathcal{S}}^m = s \frac{\partial F_{\mathcal{S}_m(t)}}{\partial \xi_{m_2}} \wedge \frac{\partial F_{\mathcal{S}_m(t)}}{\partial \xi_{m_3}} d\xi_{m_2} d\xi_{m_3} d\xi_4.$$

Using the integral rule (93) for the space-time face \mathcal{S}^m and relation (92) we find for an integrable \mathbb{R}^4 -valued function f on \mathcal{S}_m :

$$\begin{aligned} \int_{\mathcal{S}_m} \sum_{k=1}^4 f_k n_k dx &= s \int_{\hat{\mathcal{S}}} \frac{1}{2} \Delta t \sum_{k=1}^3 f_k \left(\frac{\partial F_{\mathcal{S}_m(t)}}{\partial \xi_{m_2}} \wedge \frac{\partial F_{\mathcal{S}_m(t)}}{\partial \xi_{m_3}} \right)_k d\xi_{m_2} d\xi_{m_3} d\xi_4 \\ &\quad - s \int_{\hat{\mathcal{S}}} \frac{1}{2} f_4 \sum_{k=1}^3 \Delta x_k \left(\frac{\partial F_{\mathcal{S}_m(t)}}{\partial \xi_{m_2}} \wedge \frac{\partial F_{\mathcal{S}_m(t)}}{\partial \xi_{m_3}} \right)_k d\xi_{m_2} d\xi_{m_3} d\xi_4 \\ &= s \frac{1}{2} \Delta t \left(\int_{\hat{\mathcal{S}}} \bar{f} \cdot d\bar{\mathcal{S}}^m - \int_{\hat{\mathcal{S}}} f_4 v \cdot d\bar{\mathcal{S}}^m \right) \\ &= \left(\int_{\mathcal{S}_m} \bar{f} \cdot \bar{n} dx - \int_{\mathcal{S}_m} f_4 v \cdot \bar{n} dx \right). \end{aligned}$$

Hence the geometric face integrals containing the space normal and grid velocity are evaluated as follows:

$$\int_{\mathcal{S}_m} \phi_l \phi_k \bar{n} dx = s \frac{1}{2} \Delta t \int_{\hat{\mathcal{S}}} \xi_l \xi_k d\bar{\mathcal{S}}^m, \quad (94)$$

$$\int_{\mathcal{S}_m} \phi_l \phi_k v \cdot \bar{n} dx = s \frac{1}{2} \Delta t \int_{\hat{\mathcal{S}}} \xi_l \xi_k \frac{\Delta \bar{x}}{\Delta t} \cdot d\bar{\mathcal{S}}^m \quad (95)$$

For the face \mathcal{S}_7 the parameterization is given by $F(\xi) = (t_n, F_K(\bar{\xi}))$ for $K = K(t_n^+)$. A simple computation shows that for this face we have:

$$d\hat{\mathcal{S}}^7 = -|J_K| e_4 d\bar{\xi},$$

where $e_4 = (0, 0, 0, 1)^T$ is the last unit vector in \mathbb{R}^4 . Hence,

$$\int_{\hat{\mathcal{S}}} f \cdot d\hat{\mathcal{S}}^7 = - \int_{\hat{\mathcal{S}}} f_4 |J_K| d\bar{\xi} = - \int_{K(t_n^+)} f_4 dx.$$

Likewise we have:

$$\int_{\hat{\mathcal{S}}} f \cdot d\hat{\mathcal{S}}^8 = \int_{K(t_{n+1}^-)} f_4 dx.$$

C Geometric integrals

The parameterization of the space-time face \mathcal{S} is the linear interpolation in time of the isoparametric parameterization of the space faces $S^n = S(t_n)$ and $S^{n+1} = S(t_{n+1})$. Let x_1^n, \dots, x_4^n be the four vertices of the face S^n . Then the isoparametric mapping of S^n is given by:

$$\begin{aligned} F_{S^n} : (\xi_1, \xi_2) &\mapsto \hat{x}_1^n + \hat{x}_2^n \xi_1 + \hat{x}_3^n \xi_2 + \hat{x}_4^n \xi_1 \xi_2 \\ &:= \frac{1}{4}(x_1 + x_2 + x_3 + x_4) + \frac{1}{4}(-x_1 + x_2 - x_3 + x_4)\xi_1 + \\ &\quad \frac{1}{4}(-x_1 - x_2 + x_3 + x_4)\xi_2 + \frac{1}{4}(x_1 - x_2 - x_3 + x_4)\xi_1 \xi_2. \end{aligned} \quad (96)$$

Define the vectors (in \mathbb{R}^3):

$$\begin{aligned} a_{00}^n &= \hat{x}_2^n \wedge \hat{x}_3^n = \frac{1}{8}(x_1^n - x_4^n) \wedge (x_2^n - x_3^n), \\ a_{10}^n &= \hat{x}_2^n \wedge \hat{x}_4^n = \frac{1}{8}(x_3^n - x_4^n) \wedge (x_2^n - x_1^n), \\ a_{01}^n &= \hat{x}_4^n \wedge \hat{x}_3^n = \frac{1}{8}(x_1^n - x_3^n) \wedge (x_4^n - x_2^n), \\ c_{00} &= \hat{x}_2^{n+1} \wedge \hat{x}_3^n + \hat{x}_2^n \wedge \hat{x}_3^{n+1} \\ c_{10} &= \hat{x}_2^{n+1} \wedge \hat{x}_4^n + \hat{x}_2^n \wedge \hat{x}_4^{n+1} \\ c_{01} &= \hat{x}_4^{n+1} \wedge \hat{x}_3^n + \hat{x}_4^n \wedge \hat{x}_3^{n+1} \\ n_{00} &= a_{00}^{n+1} + a_{00}^n + \frac{1}{2}c_{00}, \\ n_{10} &= a_{10}^{n+1} + a_{10}^n + \frac{1}{2}c_{10}, \\ n_{01} &= a_{01}^{n+1} + a_{01}^n + \frac{1}{2}c_{01}, \\ d_{00} &= a_{00}^{n+1} - a_{00}^n, \\ d_{10} &= a_{10}^{n+1} - a_{10}^n, \\ d_{01} &= a_{01}^{n+1} - a_{01}^n. \end{aligned} \quad (97)$$

We find:

$$\begin{aligned} \frac{\partial F_{S(t)}}{\partial \xi_{m_2}} \wedge \frac{\partial F_{S(t)}}{\partial \xi_{m_3}} &= \frac{1}{4}(1 + \xi_4)^2 (a_{00}^{n+1} + \xi_{m_2} a_{10}^{n+1} + \xi_{m_3} a_{01}^{n+1}) \\ &\quad + \frac{1}{4}(1 - \xi_4)^2 (a_{00}^n + \xi_{m_2} a_{10}^n + \xi_{m_3} a_{01}^n) \\ &\quad + \frac{1}{4}(1 - \xi_4^2)(c_{00} + \xi_{m_2} c_{10} + \xi_{m_3} c_{01}), \end{aligned} \quad (98)$$

and the geometric integrals (94) obtained using this formula are tabulated in Table 4.



Table 4 The integrals $\frac{s}{\Delta t} \int_S \phi_l \phi_m \bar{n} dx$. The sign for $m = m_1$ is equal to $\phi_{m_1}|_S$.

	$m = 0$	$m = m_1$	$m = m_2$	$m = m_3$	$m = 4$
$l = 0$	$\frac{4}{3}n_{00}$	$\pm\frac{4}{3}n_{00}$	$\frac{4}{9}n_{10}$	$\frac{4}{9}n_{01}$	$\frac{2}{3}d_{00}$
$l = m_2$	$\frac{4}{9}n_{10}$	$\pm\frac{4}{9}n_{10}$	$\frac{4}{9}n_{00}$	0	$\frac{2}{9}d_{10}$
$l = m_3$	$\frac{4}{9}n_{01}$	$\pm\frac{4}{9}n_{01}$	0	$\frac{4}{9}n_{00}$	$\frac{2}{9}d_{01}$
$l = 4$	$\frac{2}{3}d_{00}$	$\pm\frac{2}{3}d_{00}$	$\frac{2}{9}d_{10}$	$\frac{2}{9}d_{01}$	$\frac{8}{15}n_{00} - \frac{2}{15}c_{00}$

Table 5 The integrals $\frac{s}{\Delta t} \int_S \phi_l \phi_m \bar{n} \cdot v dx$. The sign for $m = m_1$ is equal to $\phi_{m_1}|_S$.

	$m = 0$	$m = m_1$	$m = m_2$	$m = m_3$	$m = 4$
$l = 0$	v_{000}	$\pm v_{000}$	v_{100}	v_{010}	v_{001}
$l = m_2$	v_{100}	$\pm v_{100}$	v_{200}	v_{110}	v_{101}
$l = m_3$	v_{010}	$\pm v_{010}$	v_{110}	v_{020}	v_{011}
$l = 4$	v_{001}	$\pm v_{001}$	v_{101}	v_{011}	v_{002}

The grid velocity v is given by:

$$v = \frac{\Delta x}{\Delta t} = \hat{b}_1 + \hat{b}_2 \xi_{m_2} + \hat{b}_3 \xi_{m_3} + \hat{b}_4 \xi_{m_2} \xi_{m_3}, \quad (99)$$

with $\hat{b}_i = (\hat{x}_i^{n+1} - \hat{x}_i^n) / \Delta t$. Note that the grid velocity does not depend on the computational time coordinate.

Define the numbers:

$$\begin{aligned} v_{000} &= \frac{4}{3} \hat{b}_1 \cdot n_{00} + \frac{4}{9} \hat{b}_2 \cdot n_{10} + \frac{4}{9} \hat{b}_3 \cdot n_{01}, \\ v_{100} &= \frac{4}{9} \hat{b}_2 \cdot n_{00} + \frac{4}{9} \hat{b}_1 \cdot n_{10} + \frac{4}{27} \hat{b}_4 \cdot n_{01}, \\ v_{010} &= \frac{4}{9} \hat{b}_3 \cdot n_{00} + \frac{4}{27} \hat{b}_4 \cdot n_{10} + \frac{4}{9} \hat{b}_1 \cdot n_{01}, \\ v_{200} &= \frac{4}{9} \hat{b}_1 \cdot n_{00} + \frac{4}{15} \hat{b}_2 \cdot n_{10} + \frac{4}{27} \hat{b}_3 \cdot n_{01}, \\ v_{020} &= \frac{4}{9} \hat{b}_1 \cdot n_{00} + \frac{4}{27} \hat{b}_2 \cdot n_{10} + \frac{4}{15} \hat{b}_3 \cdot n_{01}, \\ v_{110} &= \frac{4}{27} \hat{b}_4 \cdot n_{00} + \frac{4}{27} \hat{b}_3 \cdot n_{10} + \frac{4}{27} \hat{b}_2 \cdot n_{01}, \\ v_{001} &= \frac{2}{3} \hat{b}_1 \cdot d_{00} + \frac{2}{9} \hat{b}_2 \cdot d_{10} + \frac{2}{9} \hat{b}_3 \cdot d_{01}, \\ v_{101} &= \frac{2}{9} \hat{b}_2 \cdot d_{00} + \frac{2}{9} \hat{b}_1 \cdot d_{10} + \frac{2}{27} \hat{b}_4 \cdot d_{01}, \\ v_{011} &= \frac{2}{9} \hat{b}_3 \cdot d_{00} + \frac{2}{27} \hat{b}_4 \cdot d_{10} + \frac{2}{9} \hat{b}_1 \cdot d_{01}, \\ v_{002} &= \frac{8}{15} \hat{b}_1 \cdot n_{00} + \frac{8}{45} \hat{b}_2 \cdot n_{10} + \frac{8}{45} \hat{b}_3 \cdot n_{01} \\ &\quad - \frac{2}{15} \hat{b}_1 \cdot c_{00} - \frac{2}{45} \hat{b}_2 \cdot c_{10} - \frac{2}{45} \hat{b}_3 \cdot c_{01}. \end{aligned}$$

Using these expressions the integrals (95) are computed and tabulated in Table 5.

D Discrete conservation

In order to stay conservative at the discrete level, the face fluxes are computed for one cell connecting to the face, and added to the other cell using only some permutation relations. These relations are the generalization of the principle that for general finite volume schemes the flux added to the one connecting cell is subtracted from the other.

Let \mathcal{S} connect the cells \mathcal{K} and \mathcal{K}' . The local face coordinate system $(\xi'_{m'_2}, \xi'_{m'_3}, \xi'_4)$ of the face derived from the topology of cell \mathcal{K}' is connected with the coordinate system $(\xi_{m_2}, \xi_{m_3}, \xi_4)$ through:

$$\begin{pmatrix} \xi'_{m'_2} \\ \xi'_{m'_3} \\ \xi'_4 \end{pmatrix} = \begin{pmatrix} A_i & 0 \\ 0 & 1 \end{pmatrix} \begin{pmatrix} \xi_{m_2} \\ \xi_{m_3} \\ \xi_4 \end{pmatrix}, \quad 1 \leq i \leq 8, \quad (100)$$

where A_i is one of the eight following rotation/mirror matrices:

$$\begin{aligned} A_1 &= \begin{pmatrix} 1 & 0 \\ 0 & 1 \end{pmatrix}, & A_2 &= \begin{pmatrix} 0 & 1 \\ -1 & 0 \end{pmatrix}, & A_3 &= \begin{pmatrix} -1 & 0 \\ 0 & -1 \end{pmatrix}, & A_4 &= \begin{pmatrix} 0 & -1 \\ 1 & 0 \end{pmatrix}, \\ A_5 &= \begin{pmatrix} -1 & 0 \\ 0 & 1 \end{pmatrix}, & A_6 &= \begin{pmatrix} 0 & 1 \\ 1 & 0 \end{pmatrix}, & A_7 &= \begin{pmatrix} 1 & 0 \\ 0 & -1 \end{pmatrix}, & A_8 &= \begin{pmatrix} 0 & -1 \\ -1 & 0 \end{pmatrix}. \end{aligned}$$

Let m_i , resp. m'_i , ($1 \leq i \leq 3$) be the ordering of the space gradients in cell \mathcal{K} , resp. \mathcal{K}' , such that (compare with (56)):

$$\begin{aligned} U_{|\mathcal{S}}^{\mathcal{K}}(\xi_{m_2}, \xi_{m_3}, \xi_4) &= U(\bar{\xi}_{m_1}; \mathcal{K}) + \xi_{m_2} \hat{U}_{m_2}(\mathcal{K}) + \xi_{m_3} \hat{U}_{m_3}(\mathcal{K}) + \xi_4 \hat{U}_4(\mathcal{K}) \\ U_{|\mathcal{S}}^{\mathcal{K}'}(\xi'_{m'_2}, \xi'_{m'_3}, \xi'_4) &= U(\bar{\xi}_{m'_1}; \mathcal{K}') + \xi'_{m'_2} \hat{U}_{m'_2}(\mathcal{K}') + \xi'_{m'_3} \hat{U}_{m'_3}(\mathcal{K}') + \xi'_4 \hat{U}_4(\mathcal{K}'). \end{aligned}$$

Using (100) we find that in the computational coordinates of face \mathcal{S} the latter equality is equivalent with:

$$U_{|\mathcal{S}}^{\mathcal{K}'}(\xi_{m_2}, \xi_{m_3}, \xi_4) = U(\bar{\xi}_{m'_1}; \mathcal{K}') + \xi_{m_2} \hat{U}'_{m'_2}(\mathcal{K}') + \xi_{m_3} \hat{U}'_{m'_3}(\mathcal{K}') + \xi_4 \hat{U}_4(\mathcal{K}').$$

where the transversal gradients are defined by:

$$\begin{pmatrix} \hat{U}'_{m'_2}(\mathcal{K}') \\ \hat{U}'_{m'_3}(\mathcal{K}') \end{pmatrix} = A_i^T \begin{pmatrix} \hat{U}_{m'_2}(\mathcal{K}') \\ \hat{U}_{m'_3}(\mathcal{K}') \end{pmatrix}.$$

By definition of the basis functions, (100) implies:

$$\begin{pmatrix} \phi_{m'_2|\mathcal{S}}^{\mathcal{K}'} \\ \phi_{m'_3|\mathcal{S}}^{\mathcal{K}'} \end{pmatrix} = A_i \begin{pmatrix} \phi_{m_2|\mathcal{S}}^{\mathcal{K}} \\ \phi_{m_3|\mathcal{S}}^{\mathcal{K}} \end{pmatrix}.$$

The remaining basis function is constant on the face: $\phi_{m_1}^{\mathcal{K}}|_S = s_S$ and $\phi_{m'_1}^{\mathcal{K}'}|_S = s'_S$.

The numerical flux is consistent, and hence:

$$F_{\text{HLLC}}(U_R, U_L, \bar{n}) = -F_{\text{HLLC}}(U_L, U_R, -\bar{n}).$$

Let U'_L and U'_R be the left and right states as seen from cell \mathcal{K}' and let \bar{n}' be the outward pointing normal of face S for cell \mathcal{K}' . Then,

$$\begin{aligned} \int_S F_{\text{HLLC}}(U'_L, U'_R, \bar{n}') dx &= \int_S F_{\text{HLLC}}(U_R, U_L, -\bar{n}) dx \\ &= - \int_S F_{\text{HLLC}}(U_L, U_R, \bar{n}) dx, \\ \int_S \phi_{m'_1}^{\mathcal{K}'} F_{\text{HLLC}}(U'_L, U'_R, \bar{n}') dx &= -s'_S \int_S F_{\text{HLLC}}(U_L, U_R, \bar{n}) dx, \\ \int_S \begin{pmatrix} \phi_{m'_2}^{\mathcal{K}'} \\ \phi_{m'_3}^{\mathcal{K}'} \end{pmatrix} F_{\text{HLLC}}(U'_L, U'_R, \bar{n}') dx &= -A_i \int_S \begin{pmatrix} \phi_{m_2}^{\mathcal{K}} \\ \phi_{m_3}^{\mathcal{K}} \end{pmatrix} F_{\text{HLLC}}(U_L, U_R, \bar{n}) dx, \\ \int_S \phi_4^{\mathcal{K}'} F_{\text{HLLC}}(U'_L, U'_R, \bar{n}') dx &= - \int_S \phi_4^{\mathcal{K}} F_{\text{HLLC}}(U_L, U_R, \bar{n}) dx. \end{aligned} \tag{101}$$

So, the face fluxes for cell \mathcal{K}' easily follow from the fluxes for cell \mathcal{K} .